Tailoring the angular and spectral reflectance characteristics of color-dynamic
films by modifying their photonic texture and topcoat roughness

by Andrew D. Blair

B.S.
University of Massachusetts - Amherst (2016)

Submitted to the Department of Mechanical Engineering
in partial fulfillment of the requirements for the degree of

MASTER OF SCIENCE IN MECHANICAL ENGINEERING

at the

MASSACHUSETTS INSTITUTE OF TECHNOLOGY

SEPTEMBER 2024

Authored by: Andrew D. Blair
                 Department of Mechanical Engineering
                 August 23, 2024

Certified by: Mathias Kolle
                 Associate Professor of Department of Mechanical Engineering
                 Thesis Supervisor

Accepted by: Nicolas Hadjiconstantinou
                 Chairman, Department Committee on Graduate Theses

This page was intentionally left blank.

Tailoring the angular and spectral reflectance characteristics of color-dynamic films by modifying their photonic texture and topcoat roughness

by

Andrew D. Blair

Submitted to the Department of Mechanical Engineering
on August 22, 2024
in partial fulfillment of the requirements for the degree of

Master of Science in Mechanical Engineering

Abstract:
Controlling nano- and microscale morphology is essential for tailoring the appearance of structurally colored stretchy films. An effective approach for controlling the optical properties of such color-dynamic photonic films, which are manufactured holographically, is demonstrated using two simple control handles: the *texture* of the photonic structure and the *surface roughness* of a transmissive topcoat. Texture of the photonic structure affects the spectral signature and angular distribution of reflected light. Surface roughness of the topcoat affects the angular distribution of incident and reflected light. Fourier optics concepts are harnessed for modeling and predicting the optical characteristics of the materials as a function of their photonic texture and topcoat roughness. The model is verified with data obtained by imaging the angular scattering distribution and spectroscopic analysis of four representative combinations of photonic texture and surface coat roughness. The findings presented in this thesis validate the hypothesis that controlling texture of the photonic film and roughness of its topcoat allows for tailoring the visual appearance of structurally colored materials. This approach provides access to a rich design space of different appearances, including strong iridescence, color constancy with collimated light sources at small angles of incidence, pure and muted colors, and specular and highly diffuse reflections.

Thesis Supervisor: Mathias Kolle
Title: Associate Professor, Mechanical Engineering

This page was intentionally left blank.

Acknowledgements

The studying, research, and collaboration process I experienced during the preparation of this thesis was truly transformative. At times grueling, at times exhilarating – I learned so much while doing this work, about the material and about myself. Thank you for reading. I had an immense amount of help, guidance, input, and support from many people along the way. I'd like to extend my gratitude to some particular folks whose contributions were significant over the last two years.

To Ben Miller: thank you for trusting me with your half-a-decade long research project. Thank you for showing me the ropes in the lab and taking so much time to explain concepts/instruments/the endless red tape of MIT. Credit to Ben for lending me his Matlab Ewald's sphere model as reference.

To Hannah Feldstein: thank you for endless laughter and camaraderie, for helping with everything all the time, especially Fall 2023 - Spring 2024. Thank you for enduring capsizing and lab fluctuations. Thank you for bringing your full self to the group, particularly the Hamster C-series. And thank you for so many horror movies.

To Max Thomsen: thank you for inspiration in the Master's thesis process (I read yours a ton). Thank you for your early tips when I first started at MIT, and thank you for your guidance on navigating the Master's program overall.

To Mohamed Yassen: thank you for challenging me to be a mentor, for pushing me to explain myself clearly, and to teach this thesis as I was learning to do it. Good luck in your studies, friend.

To Mathias Kolle: thank you for teaching me optics, materials, and how to be a student again. Thank you for teaching me how to build things in the lab, how to do a thesis, and how to do research at a graduate level. Thank you for endlessly challenging me to have an exacting eye for detail, which I will always remember. Credit to Mathias for writing the core Matlab scripts used in this thesis.

To Anthony McDougal: thank you for your friendship. Thank you for showing me how one can be a researcher and a partner and a father at the same time. Thank you for demonstrating examples of clear, funny, direct, thoughtful, and beautiful scientific presentation.

To Susan Spilecki: thank you for many writing sessions, for emotional support, for grammar editing, and for thesis mapping. I don't know how I would have finished this project without your input.

To Philippe, Al, Peter, Connor: thank you for your friendship and all the emotional support you provided behind the scenes. Heavy lifts are much easier with lots of people supporting.

To my wife and daughter, Steph and Cass: thank you for loving me in the many ways that you do. Thank you for reminding me to slow down, zoom out, and consider the big picture when needed. Thank you for jumping on this wild ride with me.

This page was intentionally left blank.

Contents

List of Figures

List of Tables

Chapter 1: Introduction

Tailoring the appearance of structurally colored films necessitates morphology control on the nano- and microscales. Presented within this thesis is a practical method for controlling the optical properties of holographically manufactured color-dynamic photonic films. The *texture* of the photonic structure and the *surface roughness* of a transmissive topcoat are the control factors of our simple technique.

The surface roughness of the topcoat modifies the incoming and outgoing light fields, affecting the angular distribution of incident and reflected light. The photonic material filters the field depending on the spectral composition and direction of the incoming light field. Thus, the texture of the photonic structure affects the spectral signature and angular distribution of reflected light (visualized in Figure 1-1).

Fourier optics principles are utilized to model the optical properties of the materials based on the texture of the photonic structure and surface roughness of the topcoat. The optical properties and appearance are characterized using three metrics:
- **Angular dependency of hue**, defined by the variation of color when changing observation angle and/or light incidence angle
- **Spectral width**, or the spectral composition of reflected light at a given angle of observation
- **Diffuseness**, defined by the angular range into which the sample scatters light

These metrics are used to define the accessible extent of an optical appearance design space. Predictions of material appearance based on optical modeling are verified with data obtained by imaging the angular scattering distribution and spectroscopic analysis of four representative combinations of photonic texture and surface coat roughness, which are demonstrated in Figure 1-2.

The findings presented in this thesis validate the hypothesis that controlling texture of the photonic film and roughness of its topcoat allows for tailoring the visual appearance of structurally colored materials. This approach provides access to a rich space of different appearances, including strong iridescence or color constancy (with collimated light sources at small angles of incidence)*,* pure and muted colors, and specular and highly diffuse reflections.
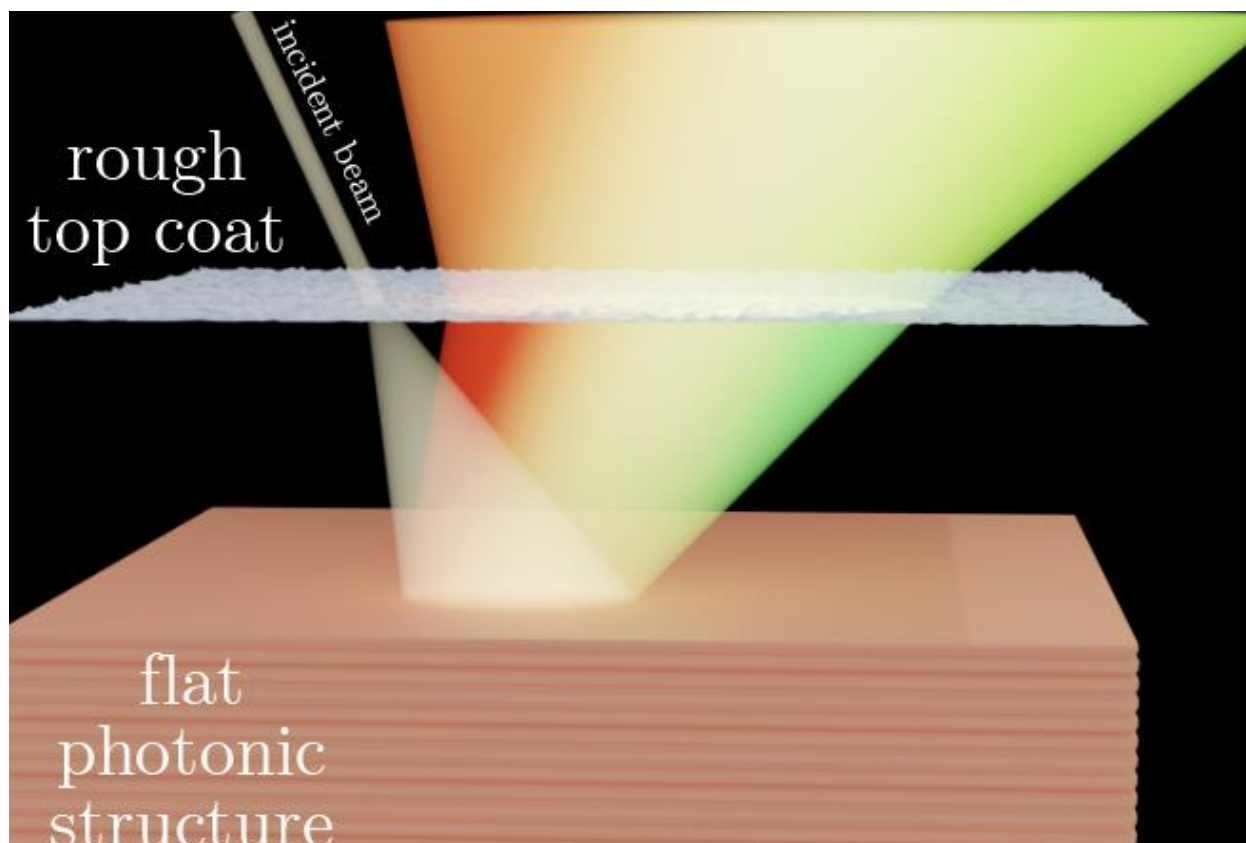
Figure 1-1 – Schematic of light interacting with a mirror-like photonic film with a rough topcoat: A flat photonic film with a rough topcoat scatters incident light at the topcoat surface based on its surface roughness. Many light waves at varying directions then encounter the flat photonic film surface and are filtered according to their angle of incidence, leading to a broadened spectral distribution. Light is scattered at the topcoat surface on its exit path out of the material. The result is a broad spectral distribution and broad angular distribution of light, visible as a distribution of colors at varying angles of observation. The schematic was drawn by Mathias Kolle and is reproduced in this thesis with permission.
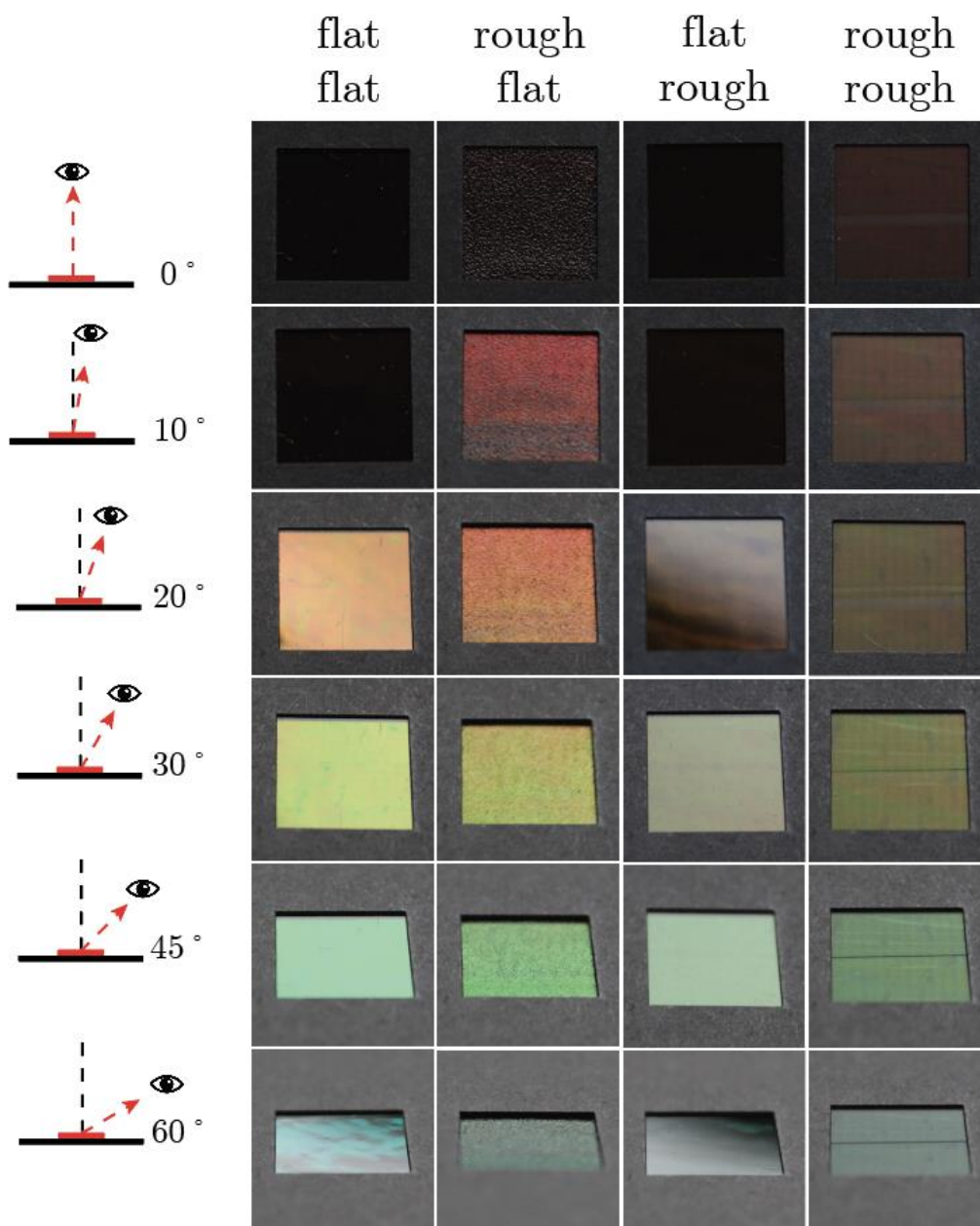
Figure 1-2 – Scattering topcoats applied to structurally colored films; visual comparison of four samples: Camera images of four different samples with different combinations of photonic film texture and topcoat roughness. Different samples are arranged in columns: flat topcoat - mirror-like photonic structure ("*flat flat*"); rough topcoat - mirror-like photonic structure ("*rough flat*"); flat topcoat - diffuse photonic structure ("*flat rough*"); rough topcoat - diffuse photonic structure ("*rough rough*"), in order from left to right. Moving down a column displays variation in optical appearance as the angle of observation θ_{obs} increases from 0° to 60°. All images were taken with a diffuse light source positioned at center angle of incidence $\theta_{inc} = 30°$ with a ± 27° angular range.

Chapter 2: Background

2.1 Structural color

The visible swirl of rainbow colors in a soap bubble or an oil slick on a puddle of water are naturally occurring structural color phenomena that manifest themselves due to light interference, which can be observed in thin films formed by soap bubbles or oil spills, as in Figure 2-1 A,B. In both depicted scenarios, a thin film of material (soapy water or oil) forms in another material environment (air or water, respectively). These different materials have different refractive indices, which causes light to propagate through each material differently. For example, the refractive index of air is close to 1 (n_1 = 1.003) and the refractive index of water is greater than 1 (n_2 = 1.33) [1]. Light hitting the interface at an angle θ_1 will either reflect equal to the angle of incidence (specularly $\theta_1 = \theta_2$) or refract through the interface at a new angle, determined by Snell's Law *(2.1)* and limited by the critical angle of the interface.

$$n_1 \, sin(\theta_1) = n_2 \, sin(\theta_2)$$

(2.1)
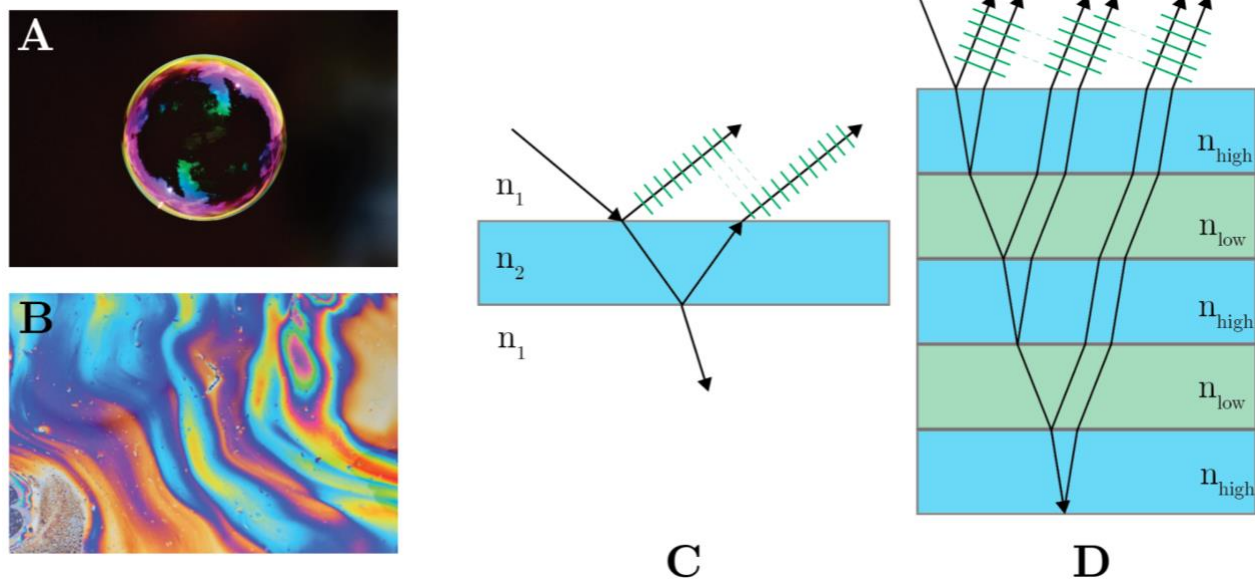
Figure 2-1 – Thin film interference: A soap bubble **(A)** and an oil slick **(B)** are common examples of thin film interference. **(C)** Diagram of simple thin film interference with a single incident ray, where $n_2 > n_1$, resulting in reflected waves which constructively interfere and thus visible color. **(D)** A stack of thin films – also known as a Bragg stack – produces similar constructive interference, with greater reflected intensity

based on the number of thin film layers. Soap and oil images reproduced from [2] and [3]. Bragg stack diagram adapted from [4].

Treating the soap bubble as a model system, as in Figure 2-1C, the bubble film of water with refractive index n_2 has air with refractive index n_1 inside and outside. The conditions when light waves constructively interfere in the thin film system are determined by the refractive indices n_1 and n_2 of the layered materials, the thickness of the thin film, and the wave vector **k** of incoming light, including its wavelength λ and angle of incidence $\theta_{incidence}$. The film will (1) reflect some light at the top surface of water, (2) refract some light at the top surface of water, (3) reflect some light at the bottom surface of the water, and (4) transmit some light through the bottom surface. Waves that reflect off and exit from the top surface of the film while in phase will constructively interfere. The path length difference and wavelength of the incident light are contributing factors to phases matching under these conditions.

When the constructive interference of waves is strong enough for our human eye (or other detector), color becomes observable and is referred to as *structural color*, which is color as the result of micro- or nano-structure, rather than dye or pigmentation. Structural color has been harnessed synthetically in a number of materials and form factors [5] for pigment replacement [6], colorimetric sensing [7], and anticounterfeiting [8].

2.2 Holographic manufacturing of structural color in elastomeric films

In 2022, Miller et al. demonstrated a method for scalable and tunable manufacturing of structural color in stretchy films, enabling color-dynamic materials [9]. The present thesis utilizes the same manufacturing technique for producing structurally colored elastomeric films. Additional applications of color-dynamic films are demonstrated in Appendix A-1.
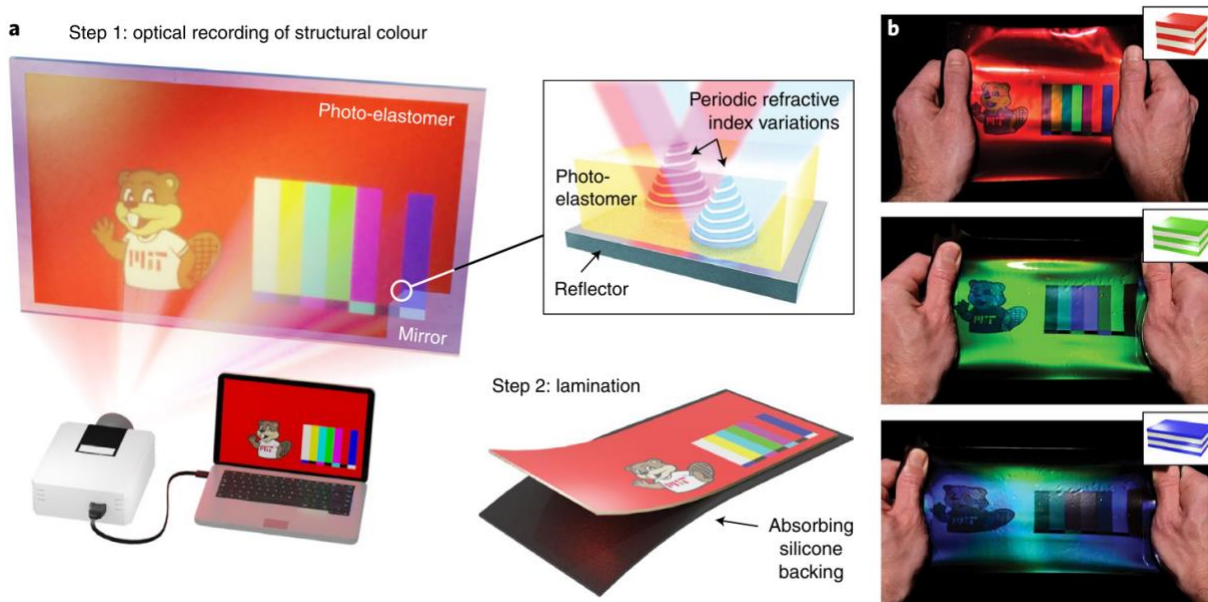
Figure 2-2 – Structural color in elastomeric photopolymer films: (A) Diagram detailing the manufacture of structural color within elastomeric photopolymer films. Step 1 shows the optical recording using a projector and mirror substrate. Step 2 shows the lamination of structurally colored photopolymer film onto a black silicone backing. **(B)** Photographs of a sample being stretched. The image on the sample has been optically manufactured and changes color when stretched based on the change in thickness of the periodic refractive index variations, as shown in the inset diagrams. Figure reproduced without modifications from Miller et al. (2022) [9].

These materials are produced using a modified desktop projector and a commercially available holographic polyurethane film. This film, when exposed to light, crosslinks internally. When laminated to a mirror and exposed to light, the holographic film will be subject to an optical standing wave, akin to Gabriel Lippmann's interference photography technique that won the Nobel Prize in 1908 [10]. The optical standing wave selectively crosslinks the photosensitive species most strongly at its *antinodes*, where the intensity of the standing wave is the highest. The photosensitive monomer in the standing wave *node* regions continues to diffuse and may eventually crosslink in the antinode regions. The exposure event thus generates regions of more- and less-crosslinked monomer, which results in a sinusoidal refractive index gradient throughout the bulk of the film.

A sinusoidal refractive index gradient causes light to reflect and refract similarly to the single thin-film interference case as detailed in section 2.1, with the resulting intensity of reflected light increasing proportional to thickness of the photopolymer film, i.e. optical path length. The intensity and wavevector of a reflected wave are a function of the difference in refractive indices Δn of the more- and less-crosslinked regions, the period of the sinusoidal refractive index variation, and the wave vector **k** of incoming light,

including its wavelength λ and angle of incidence θ_{inc}. This is discussed in greater mathematical detail in section 2.4.1. The angular and spectral reflectance characteristics of the photonic structure can be modified by altering the physical characteristics of the structure itself, including generating more complex patterns of refractive index variation.

2.3 Strategies for modifying a photonic film's optical properties

2.3.1 Texture of photonic structure

The holographic manufacturing of photonic structure in elastomeric films can be modified using diffuse reflective surfaces, e.g. brushed aluminum, rather than a flat mirror surface as introduced in section 2.2. The light exposure process can be approximated as forming standing waves coincident with the surface normals of the microscopic variations along the surface of the reflector [11]. The period of the resulting standing wave increases at elements tilted further away from the average/planar surface normal, as in Figure 2-3B. The cross-linked photonic structure in that region will then reflect a higher wavelength of light for a ray incident to that element's normal.

For example, a mirror substrate, i.e. low roughness, generates a clean standing wave and thus produces a sinusoidal variation in refractive index within the holographic film. However, a rough reflective surface such as a brushed sheet of aluminum generates a wave with a more complex wavefront, as seen in Figure 2-3A. This wavefront is the combination of many secondary wavelets that are reflected at each element of the rough reflective surface based on the direction of that elements' surface normal [12]. For example, in Figure 2-3A, an element at angle θ will reflect waves at angle 2θ.
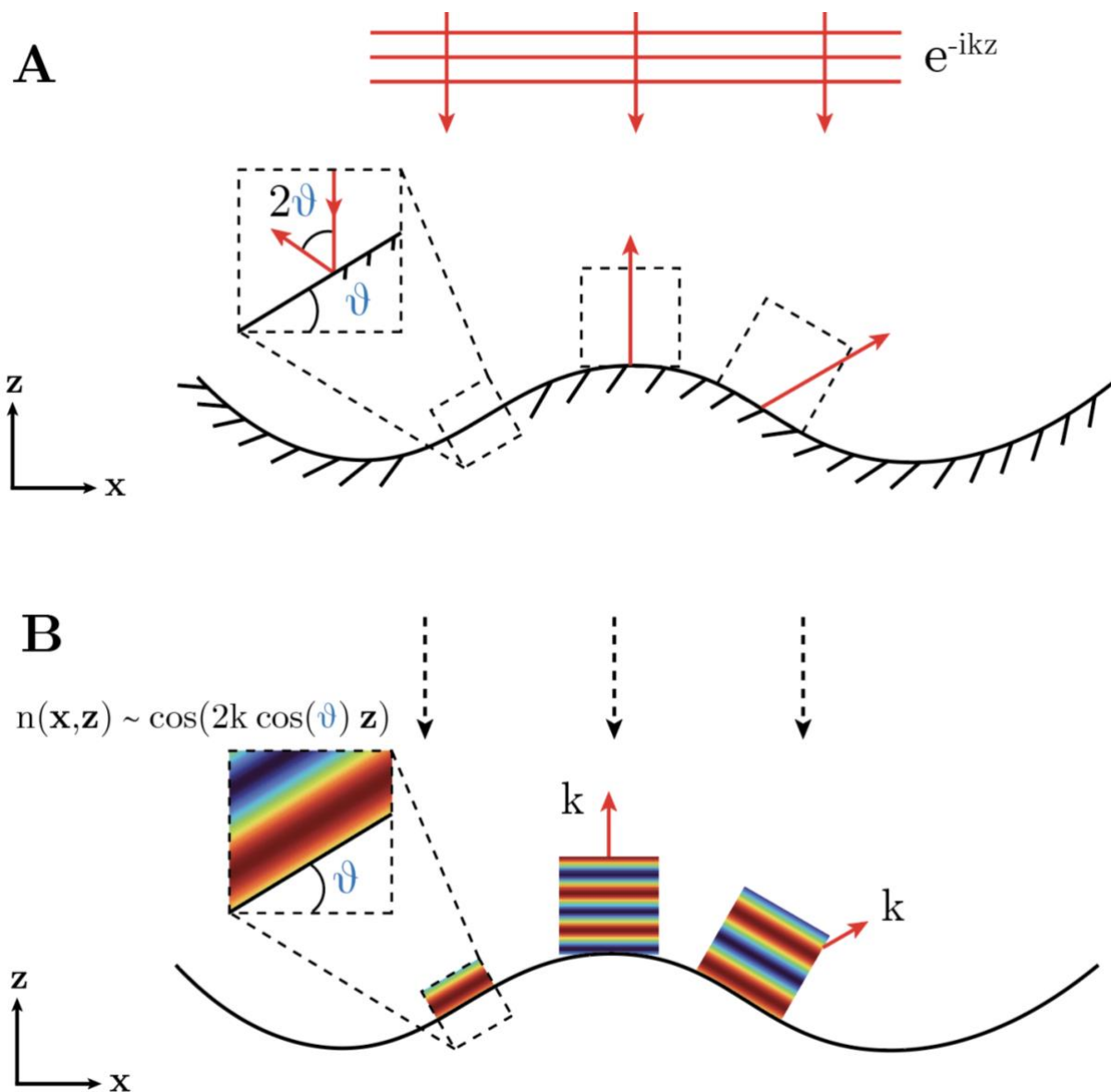
Figure 2-3 – Diffuse reflective photonic structure: (A) An incident plane wave with wavevector *k* is reflected to a variety of angles from a diffuse reflector surface, based on the surface normals at each element along the surface. Tilted elements (like those on the left and right) at angle *θ* reflect waves to angle *2θ*. The wavevector of the reflected waves will vary according to this angle *2θ*. **(B)** Period of the resulting standing wave at each element - and thus photonic structure at each element - increases as *θ* increases. This photonic structure will reflect waves with wavevectors *k* to a variety of angles, based on the structure normals at each element. Adapted from Dr. Benjamin Miller's PhD thesis [11].

Color-dynamic films holographically manufactured with a flat mirror can only be viewed under specular lighting conditions when $\theta_{inc} = \theta_{obs}$, whereas the film manufactured with a brushed reflector reflects light to a broad range of observation angles, as seen in Figure 2-4 [9, 11]. The photonic structure is modified by the texture of the reflector

substrate used during manufacturing: a more diffusely (rougher) reflective substrate produces a more diffusely reflective (rougher) photonic structure.
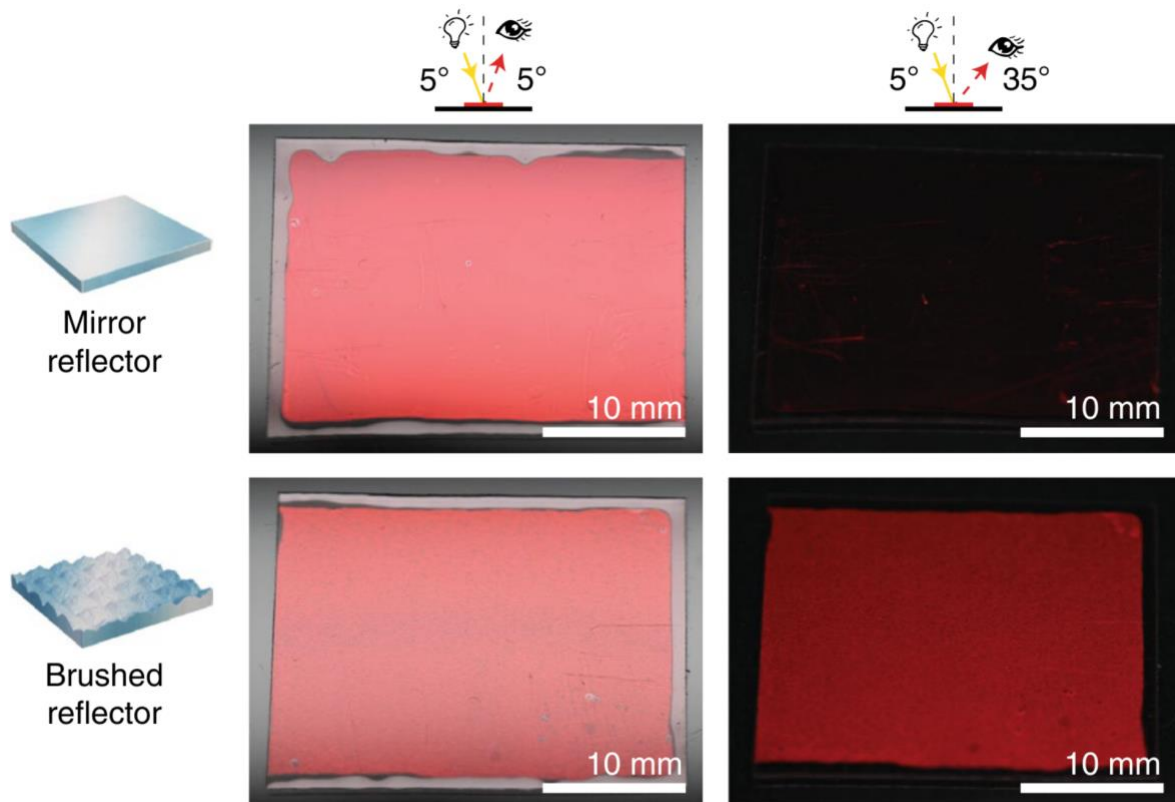
Figure 2-4 – Visual comparison of mirror and brushed reflector photonic films: Photonic structure within photopolymer films can be optically manufactured using a mirror reflector, i.e. standard silver mirror, or a brushed reflector, i.e. aluminum shim stock. The mirror reflector produces a photonic structure that strongly reflects when the angle of incidence and angle of observation are equal, but it appears dark at other angles of observation. The brushed reflector produces a photonic structure that displays color at a greater range of observation angles. Figure reproduced without modification from Miller et al. (2022) [9].

While previous work found the use of brushed reflector in optical manufacturing could tailor the visual appearance of structurally colored films [9], additional control of appearance can be achieved by tailoring the characteristics of light incident on the photonic film, which can be achieved through the addition of rough, light-transmitting topcoats.

2.3.2 Light scattering due to topcoat surface roughness

A transparent material, i.e. "topcoat," applied on top of another material can be engineered to have a desired surface roughness that scatters light [13]. A rough surface of a transparent material will allow light to radiate through the bulk after refracting the incident light to many outgoing angles, indicated in Figure 2-5.
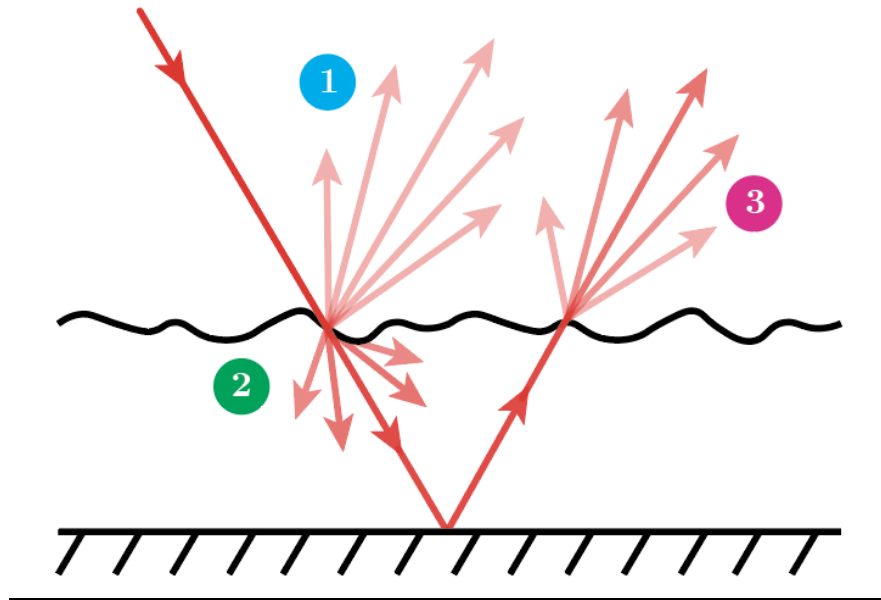
Figure 2-5 – Transparent material with rough surface scatters light: A transparent material with a rough surface profile sits above a reflective surface. In this system, scattering occurs at three stations.
(1) Scattering occurs at the surface which gives rise to surface appearances like "matte" or "glossy", based on the roughness of the surface.
(2) Scattering occurs when light transmits through the surface, where it becomes diffuse. The diffused light will eventually reflect in many directions off the reflective surface below.
(3) Scattering occurs when light transmits out of the material and through the surface again where it is diffused.

The surface roughness of the transparent topcoat modifies the angular distribution of incident light which transmits through the topcoat. This thesis demonstrates topcoats applied to photonic films, so the scattered distribution of transmitted incident light will eventually be filtered by an underlying photonic material. The topcoat also modifies the angular distribution of outgoing light by scattering the light that is reflected by the photonic film.

2.4 Fourier optics modeling framework

To accurately predict the scattering behavior of photonic films with topcoat modifications, a computationally inexpensive technique is applied that allows the mapping of the full design space of visual appearance and optical properties. Fourier optics concepts are harnessed for modeling and predicting the optical characteristics of the material system. Because the photonic structures in question are highly periodic and weakly-scattering due to low refractive index contrast ($\Delta n = 0.03$), the far-field and first-order Born approximations of the scattered light field and Ewald's sphere of reflection [11, 14] can be utilized.

2.4.1 Frequency space representation of photonic structure

The scattering potential F($\mathbf{r}$) of a photonic material is a measure of how much the material will scatter incident light in $\mathbf{r}$. The Fourier transform of the scattering potential, as in *(2.1)*, gives the far-field scattering behavior of the photonic material, predicting the angular distribution of light scattered by the material (represented in $\mathbf{K}$-space) based on its microscopic spatial optical characteristics [14].

$$\tilde{F}(\mathbf{K}) = \int F(\mathbf{r})\, e^{-i\,\mathbf{K}\cdot\mathbf{r}}\, d^3 r$$

(2.1)

For example, the holographically manufactured photonic film described in Section 2.2 can be represented as a sinusoidal variation in refractive index in $\mathbf{z}$ [11]:

$$n(\mathbf{z}) \;=\; n_0 + \frac{\Delta n}{2}\, cos(2\,k_m\,\mathbf{z})$$

(2.2)

where k_m is the wavenumber of the light used in the optical manufacturing process, n_0 is the refractive index of the matrix material ($n_0 = 1.47$) and Δn is the variation in refractive index ($\Delta n = 0.03$) [11].

Assuming the refractive index of the photonic film is constant as a function of frequency and it only varies in the $\mathbf{z}$-direction, the material's scattering potential can be defined as [14]:

$$F(\mathbf{z}) = \frac{1}{4\pi} k_0^2 \left[n^2(\mathbf{z}) - 1 \right]$$

where k_0 is the wavenumber of the incident light and will be referred to later in section 2.4.3. Squaring the sinusoidal refractive index variation n($\mathbf{z}$) from (2.2) to find n^2($\mathbf{z}$):

$$n^2(\mathbf{z}) = n_0{}^2 + \frac{\Delta n^2}{8} + n_0 \Delta n \, cos(2 k_m \, \mathbf{z}) + \frac{\Delta n^2}{8} cos(4 k_m \, \mathbf{z})$$

(2.4)

As $\Delta n \ll n_0$, a reasonable approximation can be made where the terms with Δn^2 are discarded, leaving a simplified n^2($\mathbf{z}$) expression:

$$n^2(\mathbf{z}) = n_0{}^2 + n_0 \Delta n \, cos(2 \, k_m \, \mathbf{z})$$

(2.5)

which can be substituted into (2.3):

$$F(\mathbf{z}) = \frac{1}{4\pi} k_0^2 \left[n_0{}^2 + n_0 \Delta n \, cos(2 \, k_m \, \mathbf{z}) - 1 \right]$$

(2.6)

and rearranged for clarity:

$$F(\mathbf{z}) = \frac{1}{4\pi} k_0^2 \left[(n_0{}^2 - 1) + n_0 \Delta n \, cos(2 \, k_m \, \mathbf{z}) \right]$$

(2.7)

F($\mathbf{z}$) is substituted into (2.1), where the one-dimensional Fourier transform is taken of the scattering potential in $\mathbf{z}$ to find the frequency-domain representation of the sinusoidal refractive index variation, as in (2.8) and (2.9).

$$\tilde{F}(\mathbf{K}) = \int \frac{1}{4\pi} k_0^2 \left[(n_0{}^2 - 1) + n_0 \Delta n \, cos(2 \, k_m \, \mathbf{z}) \right] e^{-i \, \mathbf{K} \cdot \mathbf{z}} \, d\mathbf{z}$$

(2.8)

$$\tilde{F}(k_z) = \frac{1}{4\pi} k_0^2 \left[(n_0{}^2 - 1)\,\delta(k_z) + n_0\,\Delta n \left(\delta(k_z - 2\,k_m) + \delta(k_z + 2\,k_m) \right) \right]$$

(2.9)

The Fourier transform of an offset cosine is a Dirac delta [14, pg. 892] at the origin – corresponding to the offset term ($n_0{}^2$ - 1) – and a pair of deltas above and below the origin at $2k_m$ along the z axis, which is defined by the wavevector k_m of the light used to optically generate the structure. The refractive index profile mathematically expressed in equation *(2.2)* is visualized in Figure 2-6A and the material's scattering potential in **K**-space expression in equation *(2.9)* is visualized in Figure 2.6B below. k_m (the wavevector of the light used in the optical manufacturing process), n_0 (the refractive index of the matrix material) and Δn (variation in refractive index) are tunable parameters in the model section 3.1.
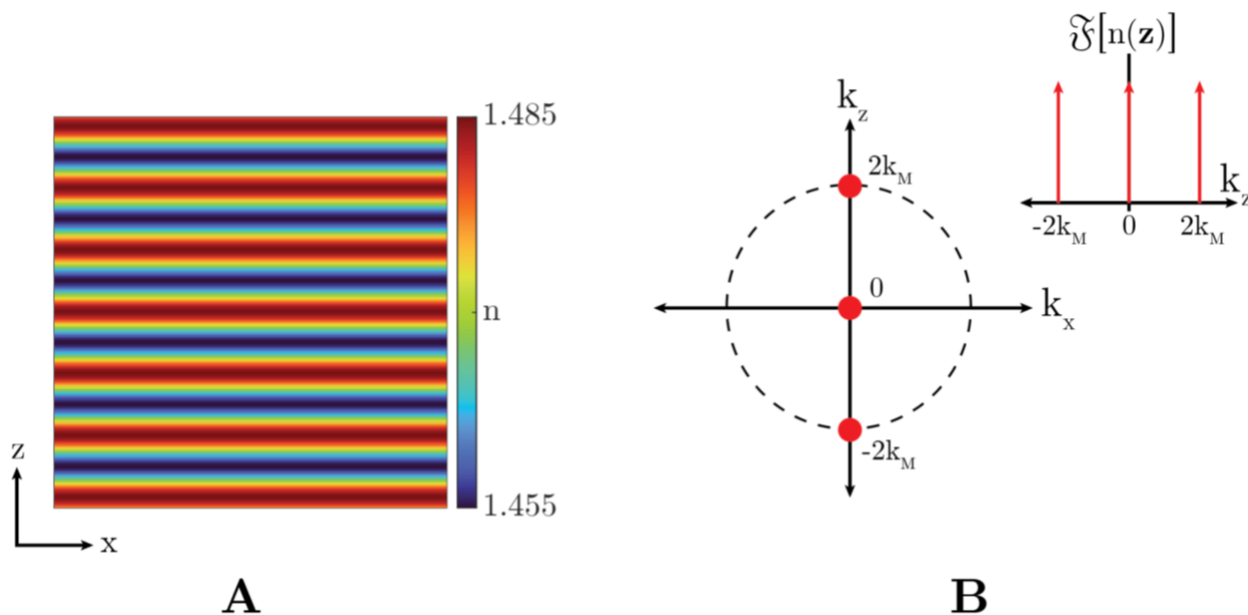
Figure 2-6 – Representation of a sinusoidal refractive index variation in space and K-space: (A) Diagram of the variation of refractive index *n(z)*, as per equation *(2.2)*. **(B)** The photonic structure can be represented in the reciprocal **K**-space by applying the Fourier transform of the scattering potential. The Fourier transform of a cosine function with amplitude offset consists of three delta functions (represented by the red dots): a pair of deltas along the k_z axis located at $2k_m$, and a delta term at the origin corresponding with the ($n_0{}^2$ - 1) amplitude offset term.

This technique allows for simple representation of any highly periodic and weakly-scattering photonic structure, implying that arbitrary photonic structures can be

imagined for inverse design. A function in **K**-space can be proposed as having desirable scattering behavior, and the spatial characteristics can be derived from such a function, which is discussed in section 4.3 and implemented for expanding the design space of tailored visual appearances using textured photonic structures and engineered rough topcoats.

2.4.2 Frequency space representation of rough topcoats

Transmissive rough topcoats with features greater than or on the order of the wavelength of incident light will scatter light in many directions [15]. The scattering potential of the rough topcoat is related to its surface roughness [16]. The degree of scattering and diffuseness in surface appearance increases as surface roughness increases [17].

Figure 2-7 A & B illustrates the real space and **K**-space representations of a rough topcoat scattering a wave from above at direction $\vec{s_{inc}}$, which is decomposed or scattered into waves with new directions $\vec{s_{in,i}}$ through $\vec{s_{in,f}}$. The distribution of the scattered waves is determined by the scattering potential of the rough topcoat. Under a weak elastic scattering approximation, the wavenumber k_0 is preserved; incident light with wavevector $k_0\vec{s_{inc}}$ scatters to wavevectors $k_0\vec{s_{in,i}}$ through $k_0\vec{s_{in,f}}$. Figure 2-7 C & D illustrates the real space and **K**-space representations of a rough topcoat scattering a wave from below at direction $\vec{s_{out}}$, which is scattered into waves with new directions $\vec{s_{obs,i}}$ through $\vec{s_{obs,f}}$.

Section 4.1 demonstrates empirical measurements of the scattering angle $\alpha_{scatter}$, which approximates the scattering behavior as a normal distribution of scattered waves, where the direction of the wave with peak amplitude is coincident with the original direction of incidence $\vec{s_{inc}}$. The scattering characteristics of a rough surface are then implemented in Ewald's sphere calculation (see Sections 2.4.3 and 3.1), where the spectral composition and angular distribution of reflected light can be modeled.
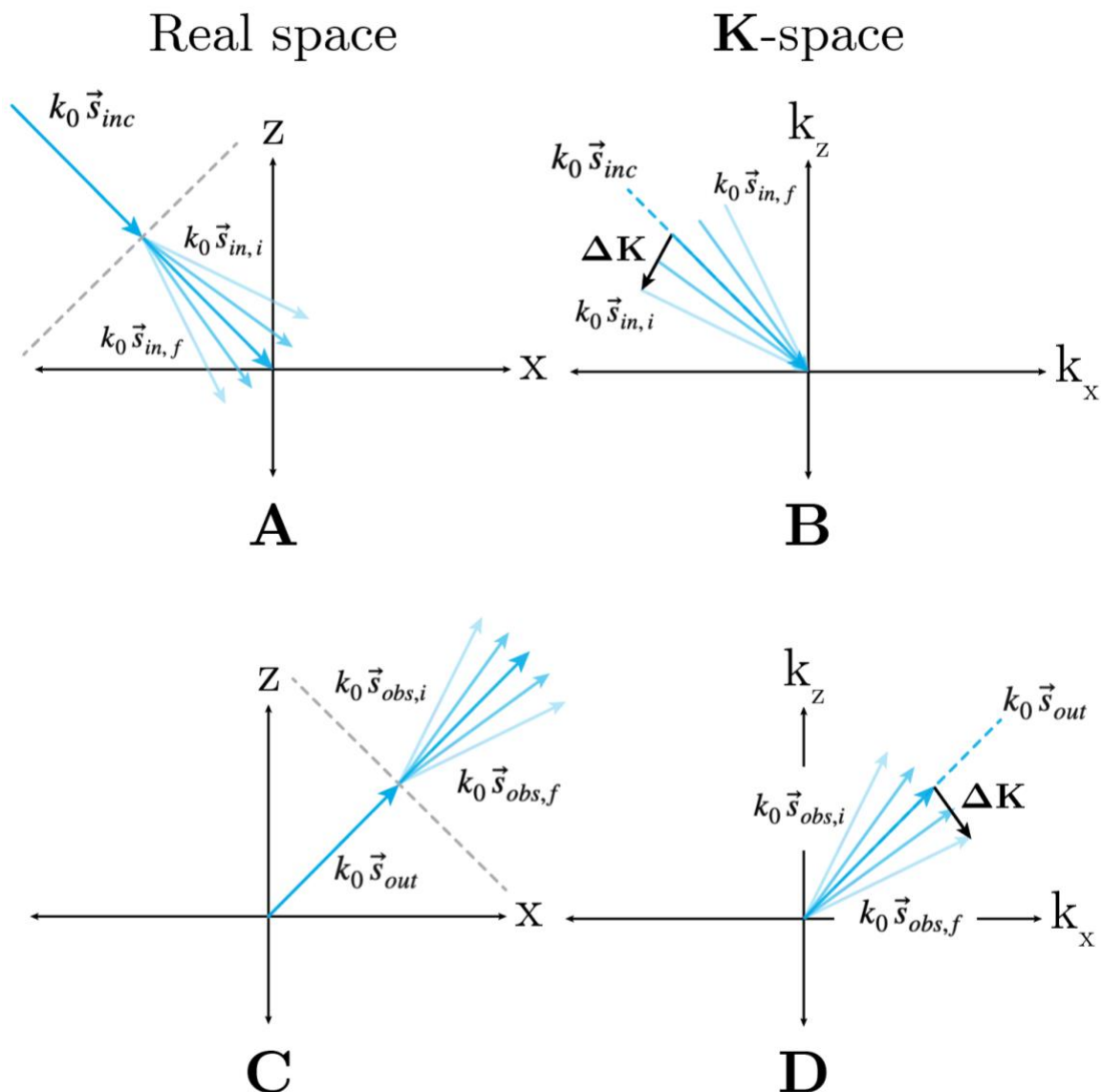
Figure 2-7 – Representation of a rough topcoat scattering in K-space: Diagrams of scattering in real space and **K**-space. **(A)** An incident wave with direction $\overrightarrow{s_{inc}}$ is scattered into many directions $\overrightarrow{s_{in,i}}$ through $\overrightarrow{s_{in,f}}$. The gray dashed line represents the surface of a transmissive scattering topcoat. **(B)** In **K**-space, an incident wave with direction $\overrightarrow{s_{inc}}$ is scattered into many directions $\overrightarrow{s_{in,i}}$ through $\overrightarrow{s_{in,f}}$ with a distribution of magnitudes. The angular extent of scattering ΔK-vectors from $k_0\overrightarrow{s_{in,i}}$ to $k_0\overrightarrow{s_{in,f}}$ is a function of the scattering cone angle of the rough topcoat. **(C)** An outgoing wave with direction $\overrightarrow{s_{out}}$ is scattered into many observation directions $\overrightarrow{s_{obs,i}}$ through $\overrightarrow{s_{obs,f}}$. **(D)** In **K**-space, scattered waves $\overrightarrow{s_{obs,i}}$ through $\overrightarrow{s_{obs,f}}$ centered on outgoing wave with direction $\overrightarrow{s_{out}}$.

2.4.3 Ewald's sphere construction

Representing a photonic structure in **K**-space via the Fourier transform of its scattering potential allows for applying the concept of Ewald's sphere of reflection to determine the scattering behavior of the photonic structure for a given direction of light incidence [11, 14]. Following the first order Born approximation – for far-field scattering behavior of a highly periodic and weakly-scattering photonic structure – the amplitude of the scattered/reflected wave for a given direction of incident light depends only on one term of the **K**-space representation of the scattering potential:

$$\Delta \mathbf{K} = k_0(\vec{s}_{out} - \vec{s}_{in})$$

(2.10)

where k_0 is the wavenumber $k_0 = 2\pi/\lambda$, $\overrightarrow{s_{in}}$ is the direction of the wavevector of the incoming light wave and $\overrightarrow{s_{out}}$ is the direction of the wavevector of the scattered/reflected wave. Then, for any incoming wave at direction $\overrightarrow{s_{in}}$ and wavenumber k_0, one can determine the magnitude of $\Delta \mathbf{K}$-vectors of the scattered wave at direction $\overrightarrow{s_{out}}$ and wavenumber k_0.

In essence, this construction allows us to draw many spheres (or circles in 2D, as shown in Figure 2-8B) of radii k_0, centered at any incidence direction $\overrightarrow{s_{in}}$ and identify the amplitude of any corresponding observation direction $\overrightarrow{s_{out}}$. At any incidence direction $\overrightarrow{s_{in}}$ from the source to the photonic structure—and for each wavenumber k_0—we can calculate the amplitude of $\Delta \mathbf{K}$-vectors for any direction $\overrightarrow{s_{out}}$ of the reflected field. The amplitude of $\Delta \mathbf{K}$-vectors can then be squared to find the far-field intensity I [14]:

$$I = |\Delta \mathbf{K}|^2$$

(2.11)

Intensities I can be calculated for any wavenumber k_0 and consolidated as a full reflectance spectrum for a photonic structure. As implemented in the model – sections 3.1.3 and 3.1.4 – these spectra for any directions $\overrightarrow{s_{in}}$ and/or $\overrightarrow{s_{out}}$ can be converted to RGB colors, allowing for visualization of the scattering behavior of any photonic structure or photonic material system.
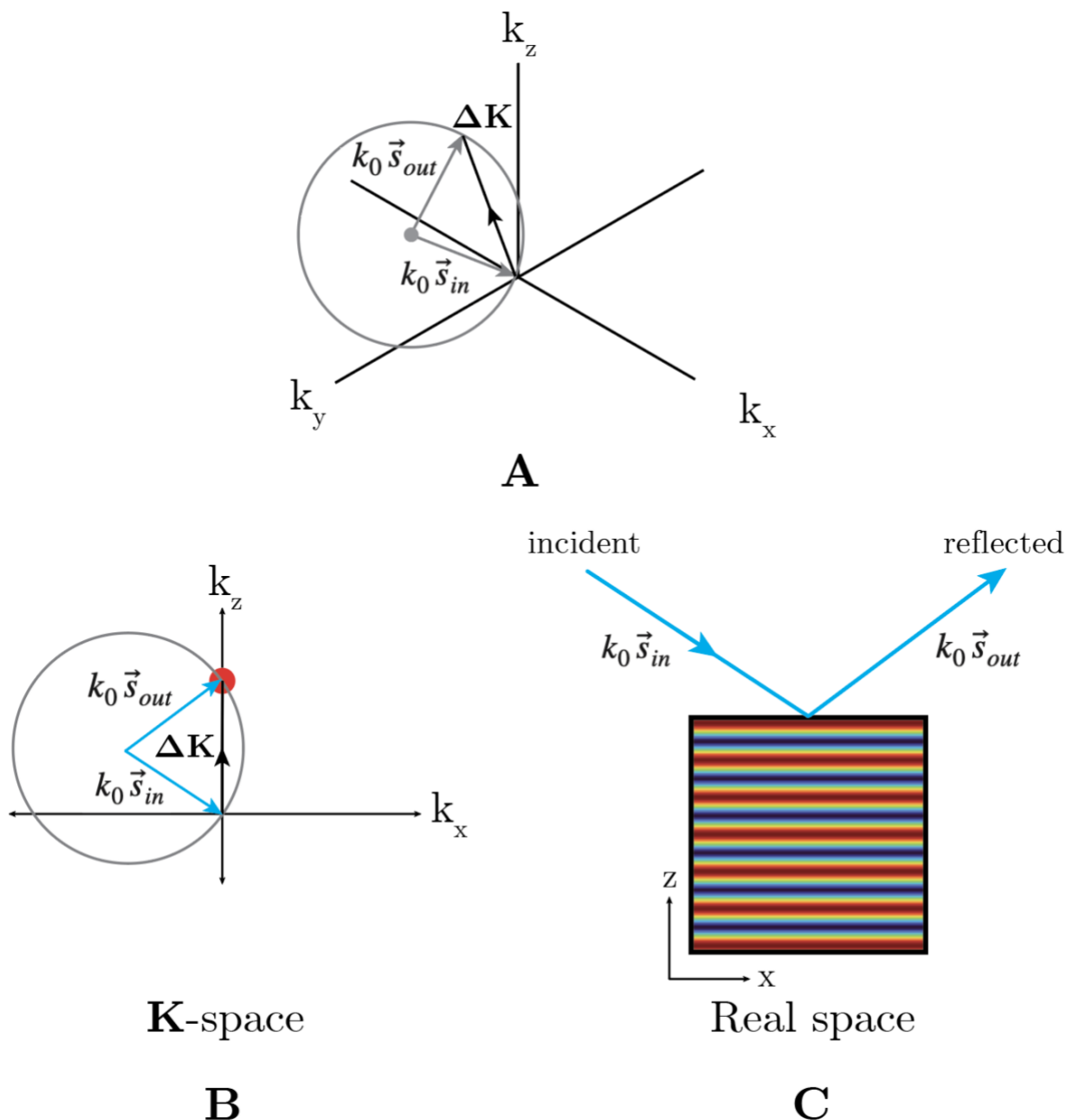
Figure 2-8 - Ewald's sphere construction: (A) Diagram of Ewald's sphere of reflection, a visual representation of the light scattering behavior of a photonic structure. The points on the surface of a sphere in **K**-space, with radius k_0 and centered at $-k_0\overrightarrow{s_{in}}$, represent the conditions for light scattering by the photonic structure from incident light with wavevector $k_0\overrightarrow{s_{in}}$ and scattered/reflected light with wavevector $k_0\overrightarrow{s_{out}}$. Adapted from [11]. **(B)** Diagram of photonic structure in reciprocal space scattering incident light with wavevector $k_0\overrightarrow{s_{in}}$ (blue wavelength) to reflected light with wavevector $k_0\overrightarrow{s_{out}}$. The amplitude of the scattered wave can be determined by the **K**-space value of the photonic function, i.e. magnitude of the Fourier transform of the scattering potential that vector ΔK points to *(2.10)*. Here the photonic function has been simplified from Figure 2-6 as a single delta node, represented by a red dot. **(C)** Diagram of photonic structure in

real space scattering incident light with wavevector $k_0\overrightarrow{s_{in}}$ (blue wavelength) to reflected light with wavevector $k_0\overrightarrow{s_{out}}$. Adapted from [18].

2.4.4 Bidirectional reflectance distribution function (BRDF)

The reflective behavior of a surface is characterized by the bidirectional reflectance distribution function (BRDF) [19]. For a uniformly illuminated surface with large area (relative to illuminant size) that is uniform and isotropic, the reflecting properties are characterized by:

$$BRDF = I(\theta_{in}, \varphi_{in}) = \int_{\theta_1}^{\theta_2} \int_{\varphi_1}^{\varphi_2} S(\theta_{in}, \varphi_{in}, \theta_{out}, \varphi_{out})\, sin\theta_{out}\, d\theta_{out}\, d\varphi_{out}$$

(*2.12*)

where *S* is the general scattering function of the surface. BRDF is calculated using an area differential solid angle, or a patch $sin(\theta)\, d\theta\, d\phi$ on a spherical surface around the illuminated surface. *I* is the intensity at all angles of observation ($\theta_{out} = \theta_{obs}$, $\varphi_{out} = \varphi_{obs}$). The BRDF of a surface or material describes the angular and spectral reflectance distribution and can be calculated to model the optical properties and/or visual appearance of that surface, especially in computer vision applications [20].

Chapter 3: Modeling Optical Characteristics of Photonic Films with Fourier Optics

A model was developed in Matlab by Mathias Kolle to predict the optical characteristics and visual appearance of photonic films with rough topcoats. Utilizing Fourier optics concepts simplifies the computation of wave propagation and scattering by operating in the frequency domain, or **K**-space; it also enables significant variability in defining the scattering behavior of the photonic material and rough topcoat. First, the specific topcoat and photonic structure functions are defined. The model then discretely solves the bidirectional reflectance distribution function (BRDF) of the scattering topcoat and photonic structure material system. The model outputs reflectance spectra for many angles of observation. The model's key input parameters are (1) the scattering angle of the rough topcoat, (2) photonic structure texture and periodicity, and (3) illumination conditions. The flexibility and speed of the model allows for simulation of visual appearances that define the corners of a representative design space.

3.1 Simulating appearance and optical properties

To simulate the visual appearance and optical properties of a photonic material system, a spherical coordinate system is employed to describe light propagation in space relative to a material positioned at the origin. Angles of incidence (θ_{inc}, φ_{inc}) and observation (θ_{obs}, φ_{obs}) can be defined, where θ is the polar angle, φ is the azimuthal angle, and r is the radial distance from the origin. Spherical coordinates simplify the process of integrating over spherical surfaces [21].

Figure 3-1 shows a two-dimensional schematic of the coordinate systems employed in the model. The model simulates the incoherent superposition of the intensities of waves at a given observation angle (θ_{obs}, φ_{obs}). These waves originate from a source positioned at (θ_{inc}, φ_{inc}) which scatter into angles (θ_1, φ_1) after transmitting through the topcoat S_{in}. The photonic film R filters and reflects these waves to directions (θ_2, φ_2), based on each wave's direction (θ_1, φ_1) and wavenumber k_0. The topcoat S_{out} scatters the waves at directions (θ_2, φ_2) into angles (θ_{obs}, φ_{obs}) on their way out of the material.
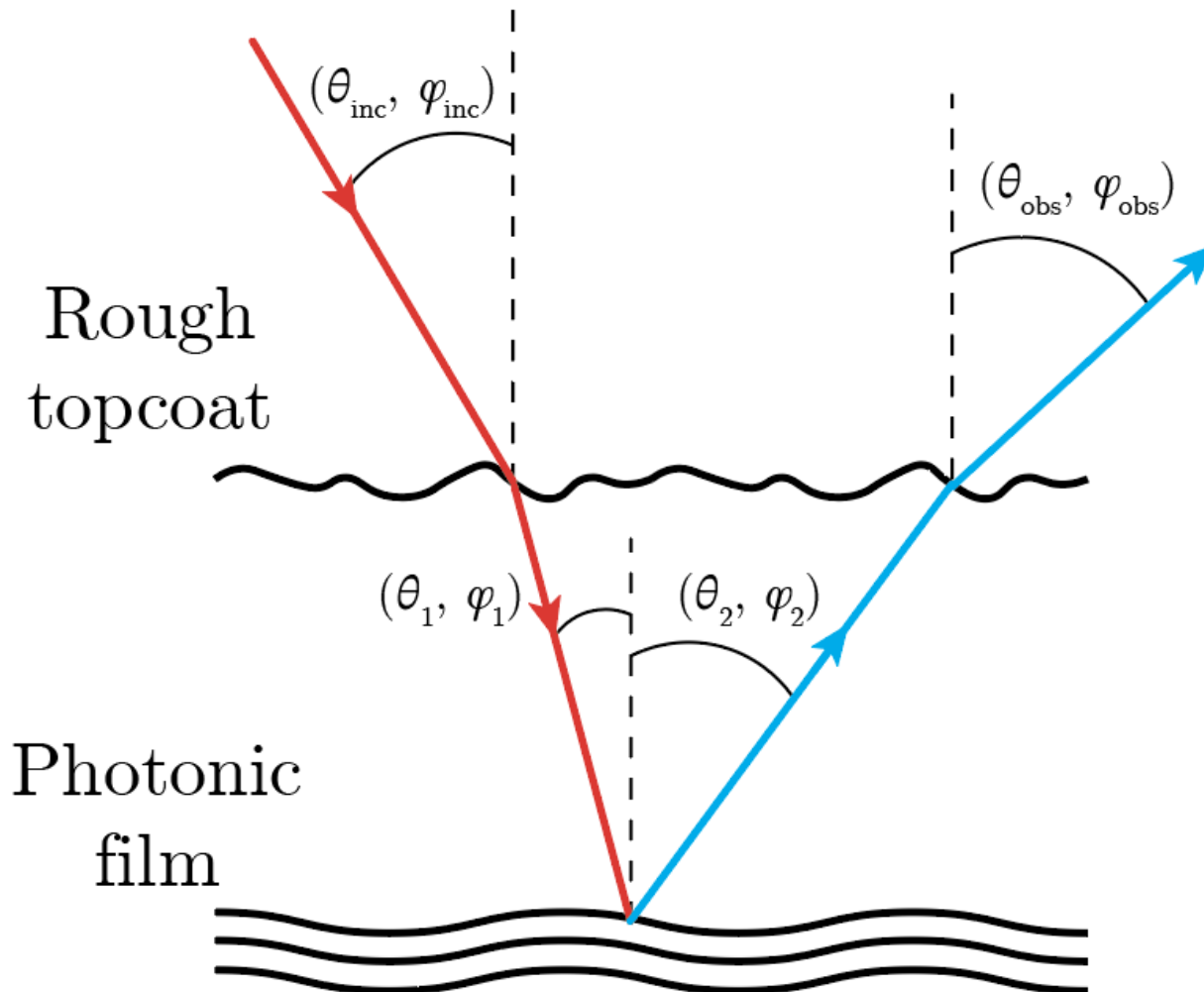
Figure 3-1 - Coordinate system schematic: The rough topcoat scatters incident light at (θ_{inc}, φ_{inc}) into angles (θ_1, φ_1). Waves at directions (θ_1, φ_1) are reflected and filtered by the photonic film to directions (θ_2, φ_2). Waves at directions (θ_2, φ_2) are scattered by the rough topcoat as they exit the material. Figure adapted from illustrations by Mathias Kolle.

As introduced in section 2.4.4, the bidirectional reflectance distribution function (BRDF) is a function that defines how light is scattered and reflected by this material system, using the spherical coordinate systems outlined above. The BRDF is demonstrated in equation (*3.1*):

$$BRDF = I\left(\theta_{inc}, \varphi_{inc}, \theta_{obs}, \varphi_{obs}, \lambda\right) =$$

$$\int_0^{2\pi} \int_0^{\frac{\pi}{2}} \int_0^{2\pi} \int_0^{\frac{\pi}{2}} S_{in}(\theta_{inc}, \varphi_{inc}, \theta_1, \varphi_1)\, R(\theta_1, \varphi_1, \theta_2, \varphi_2, \lambda)\, S_{out}(\theta_2, \varphi_2, \theta_{obs}, \varphi_{obs})\, d\theta_1\, d\varphi_1\, d\theta_2\, d\varphi_2$$

(3.1)

The quadruple integral is calculated discretely in the model, for the entire hemispherical range above the photonic film for ranges $0 \leq \theta_1 \leq \frac{\pi}{2}$, $0 \leq \varphi_1 \leq 2\pi$, $0 \leq \theta_2 \leq \frac{\pi}{2}$, and $0 \leq \varphi_2 \leq 2\pi$.

Figure 3-2 shows a schematic of the model pipeline. First, the illumination conditions and material properties are input, i.e. angle of incidence (θ_{inc}, φ_{inc}), refractive index of the photonic material n_0, and wavenumber k_m of the light used in the optical manufacturing process. Then, the photonic material (Section 3.1.1) and the scattering topcoat (Section 3.1.2) are represented as functions in **K**-space. Next, the BRDF is discretely solved using Ewald's sphere (Section 3.1.3) for all wavelengths and all observation angles, returning reflectivity spectra of intensity I versus wavelength λ. These spectra are converted to XYZ values in the CIE 1931 color space, and the XYZ values are converted to RGB values (Section 3.1.4). RGB values are converted to colors and mapped as points on a polar diagram. Individual points of interest can be sampled to relate visible color to a corresponding reflectivity spectrum.
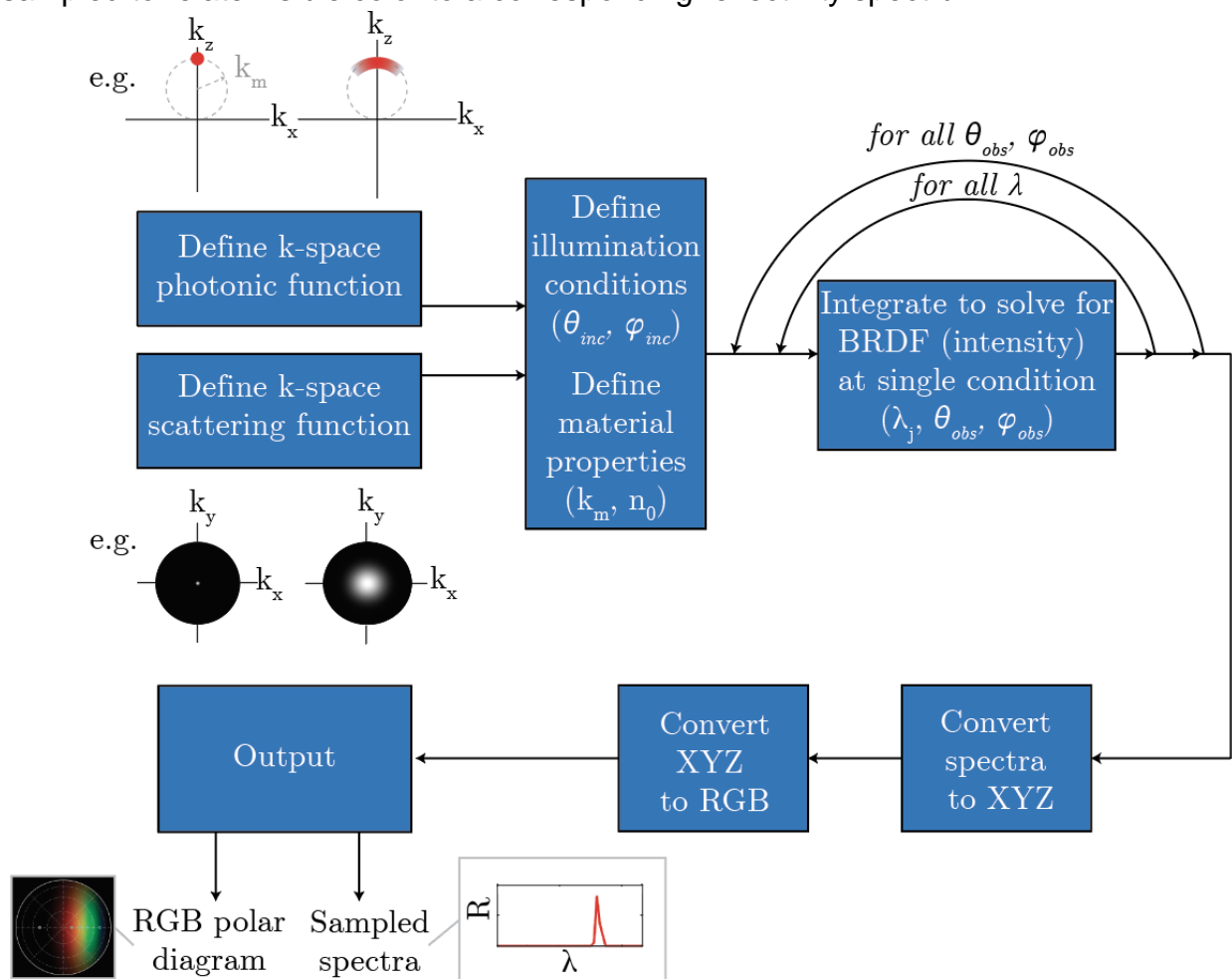
Figure 3-2 - Model schematic: Diagram showing the model pipeline. The photonic film and topcoat functions are defined in **K**-space. Illumination conditions and material properties are defined. These parameters are used to discretely solve the bidirectional reflectance distribution function (BRDF) for all observation angles and wavelengths. The solutions of the BRDF – many reflectance spectra – are finally converted to and output as RGB colors. This process can be iterated by changing the angular and specular distribution parameters of the photonic material function and topcoat function.

3.1.1 Modeling photonic structure in frequency space

To model specific photonic film textures, photonic material function R is defined in **K**-space as:

$$R\left(k_x, k_y, k_z\right) = e^{-\left|\frac{\left((k_z - k_M)^2 + k_x{}^2 + k_y{}^2 - k_M{}^2\right)^2}{\left(k_M\,\sigma_0\right)^2}\right|}\; e^{\frac{-1}{2}\left(\frac{k_x}{\sigma_x}\right)^2}\; e^{\frac{-1}{2}\left(\frac{k_y}{\sigma_y}\right)^2}$$

(3.2)

where k_x, k_y, and k_z are coordinates in reciprocal space with units of inverse distance (typically 1/µm or 1/nm for visible wavelengths). k_M is the wavenumber of light used in optical manufacture, defined as:

$$k_M = \frac{2\pi\, n_0}{\lambda_m}$$

(3.3)

where n_0 is the refractive index of the photopolymer film ($n_0 \sim$ 1.5 for polyurethane [22]) and λ_M is the wavelength of the exposure light field.

The first exponential term of the function *(3.2)* can be conceptualized as a normal distribution along a spherical path with radius k_M in **K**-space. σ_0 corresponds to the width of the normal distribution, which is determined by the *spectral distribution* of the light exposure field used to manufacture the photonic material. σ_x and σ_y in the second and third exponential terms correspond to the *angular distribution of scattering* of the reflective surface used during manufacture, denoted as the standard deviation of a Gaussian distribution function [23]. σ_x and σ_y are derived from the x- and y-direction scatter angles β_x and β_y, as empirically measured in Section 4.1 and illustrated in Figure 3-3 below.
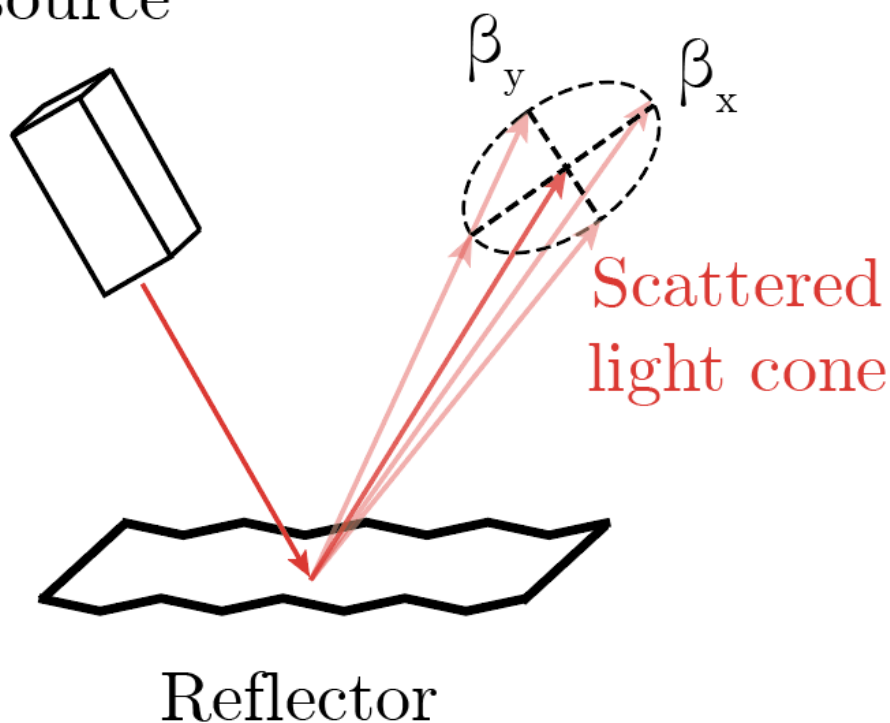
Figure 3-3 - Reflective surface scatter angles β_x and β_y: A collimated source illuminates a rough reflective surface and scatters into a cone at angles β_x and β_y. β_x is the horizontal scattering angle, or major axis cone angle of an ellipsoidal scattering cone; β_y is the vertical scattering angle, or minor axis cone angle of an ellipsoidal scattering cone. For an anisotropically scattering surface (e.g. anisotropic brushed reflector), the horizontal and vertical scattering angles are not equal $\beta_x \neq \beta_y$.

For example, to find σ_x from the x-direction scatter angle β_x, first the k_x-direction full-width half maximum FWHM$_{kx}$ is calculated (*3.4*). Assuming the scatter angles β in real space are equivalent to the scatter angles in **K**-space, FWHM$_{kx}$ is the full width half maximum of the normal distribution of scattered light in the k_x-direction.

$$FWHM_{kx} = 2k_M \, tan(\beta_x)$$

(3.4)

FWHM$_{kx}$ can then be converted into the Gaussian distribution standard deviation σ_x value (*3.5*) [24].

$$\sigma_x = \frac{FWHM_{kx}}{2\sqrt{2 \ln 2}} = \frac{FWHM_{kx}}{2.35}$$

The frequency space photonic function for different scatter angles ($\beta_x = \beta_y = 0.1°$ and 12°) is visualized in Figure 3-4A & B, plotted in k_z and k_x. Figure 3-4C shows a three-dimensional plot of the photonic material function for $\beta_x = \beta_y = 12°$.
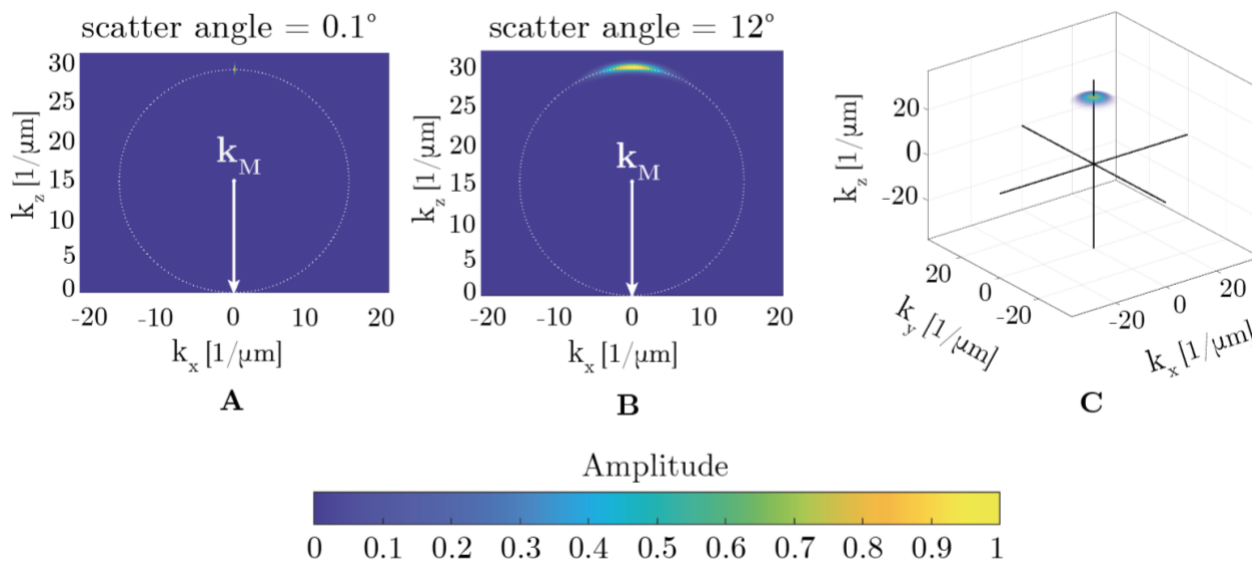

Figure 3-4 – **Photonic material in K-space, Matlab outputs:** (**A**) Two-dimensional slice of the frequency space representation of a photonic structure made using a mirror ($\beta_x = \beta_y = 0.1°$), plotted in k_z and k_x. The peak value is located at $2k_M$. The center point (and optical manufacturing wavevector k_M) is marked in white as k_M. (**B**) Two-dimensional slice of the frequency space representation of a photonic structure made using a diffuse reflector ($\beta_x = \beta_y = 12°$). (**C**) Three-dimensional plot of photonic structure featured in **B**. The amplitude legend refers to all three figures.

3.1.2 Modeling scattering topcoat in frequency space

The **K**-space photonic material function R is modified by the **K**-space scattering functions S_{in} and S_{out}. S_{in} is the scatter function as light enters the material through the topcoat, as in Figure 2-6, (**2**). S_{out} is the scatter function as light exits the material through the topcoat as in Figure 2-6, (**3**).

To define specific topcoat configurations, the scattering functions are defined in the model as:

$$S(\Delta\mathbf{K}) = \frac{\sqrt{2\pi}}{\sigma_s} \, e^{\frac{-1}{2}\frac{\Delta\mathbf{K}^2}{\sigma_s{}^2}}$$

(3.6)

where $S(\Delta\mathbf{K})$ is the intensity of scattered light. The derivation of the argument $\Delta\mathbf{K}$ is illustrated in Figure 3-5, using $S_{out}(\Delta\mathbf{K}_{out})$ as an example.
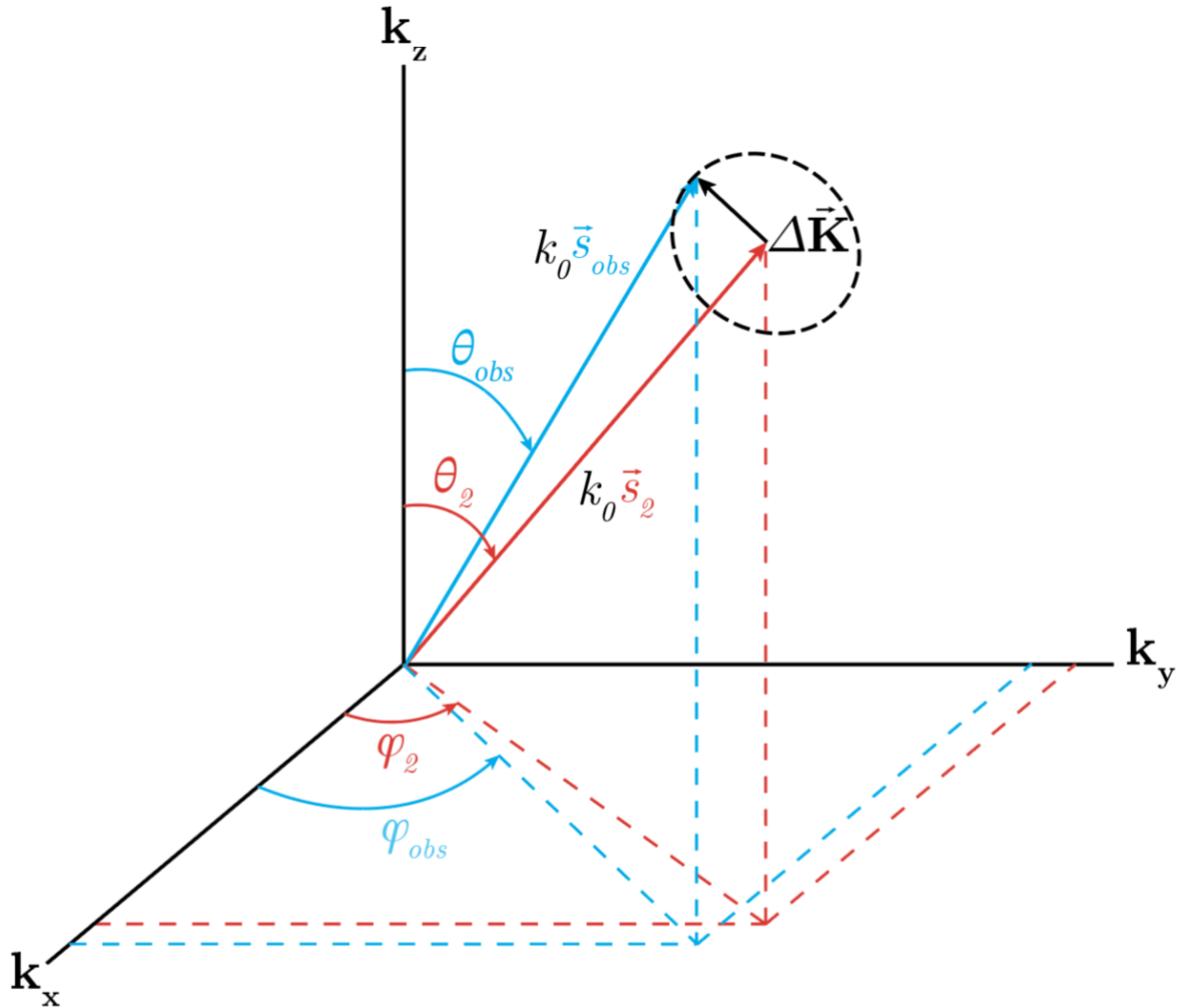
$$|\Delta\vec{\mathbf{K}}| = |\vec{s}_{obs} - \vec{s}_2|$$

$$= k_0 \begin{vmatrix} \sin\vartheta_{obs}\cos\varphi_{obs} - \sin\vartheta_2\cos\varphi_2 \\ \sin\vartheta_{obs}\sin\varphi_{obs} - \sin\vartheta_2\sin\varphi_2 \\ \cos\vartheta_{obs} - \cos\varphi_2 \end{vmatrix}$$

Figure 3-5 - Derivation of ΔK for scattering topcoats in K-space: Illustration of ΔK for $S_{out}(\Delta \mathbf{K_{out}})$, which is the deviation of the scattered light $k_0\overrightarrow{s_{obs}}$ at direction (θ_{obs}, φ_{obs}) from the incident light $k_0\overrightarrow{s_2}$ at direction (θ_2, φ_2). The extent of the scattering cone is denoted by the dashed black circle. Both scattered and incident waves have wavenumber k_0. The mathematical derivation of ΔK**out** (equation *(3.8)*) is shown. Figure adapted from illustrations by Mathias Kolle.

For $S_{in}(\Delta \mathbf{K_{in}})$, the argument ΔK**in** of the scattering function *(3.6)* is defined as:

$$\Delta \mathbf{K_{in}} = k_0\sqrt{2\left(1 - sin\theta_1\,sin\theta_{inc}\,cos(\varphi_1 - \varphi_{inc}) - cos\theta_1\,cos\theta_{inc}\right)}$$

(3.7)

for the deviation of the scattered light $k_0\overrightarrow{s_1}$ at direction (θ_1, φ_1) from the incident light $k_0\overrightarrow{s_{inc}}$ direction at (θ_{inc}, φ_{inc}) in **K**-space.

For $S_{out}(\Delta \mathbf{K_{out}})$, the argument ΔK**out** is defined as:

$$\Delta \mathbf{K_{out}} = k_0\sqrt{2\left(1 - sin\theta_{obs}\,sin\theta_2\,cos(\varphi_{obs} - \varphi_2) - cos\theta_{obs}\,cos\theta_2\right)}$$

(3.8)

for the deviation of the scattered light $k_0\overrightarrow{s_{obs}}$ at direction (θ_{obs}, φ_{obs}) from the incident light $k_0\overrightarrow{s_2}$ direction at (θ_2, φ_2) in **K**-space.

k_0 is the wavenumber of the waves of interest. If the surface features of the rough topcoat are comparable to the order of the wavelengths of incident light, scattering is less dependent on wavelength and all wavelengths will scatter similarly [11]. It should be noted that the scattering functions *(3.6)* and/or *(3.7)* and *(3.8)* could be developed further for greater accuracy in scattering behavior in relation to the surface roughness of the topcoat, especially incorporating the generalized Harvey-Shack surface scatter theory which characterizes the scattering behavior of a surface by its surface transfer function [15, 25, 26, 27].

σ_s in equation (*3.6*) represents the degree of scattering of the rough topcoat. σ_s is derived from the scattering angle of the topcoat $\alpha_{scatter}$, which is measured empirically in Section 4.1 and illustrated in Figure 3-6.
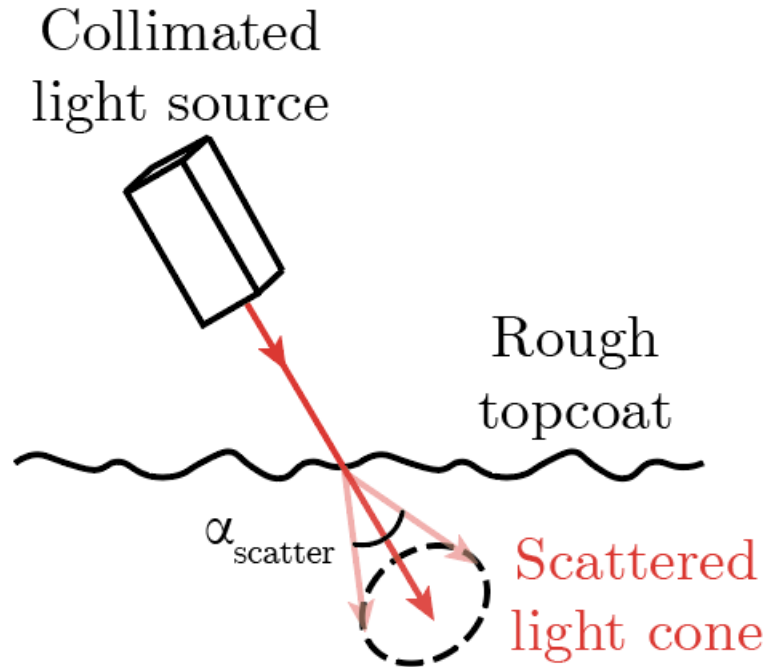
Figure 3-6 - Rough transmissive topcoat scatter angle $\alpha_{scatter}$: A collimated source illuminates a rough transmissive topcoat and scatters light into a cone at angle $\alpha_{scatter}$.

To find σ_s from scatter angle $\alpha_{scatter}$, first the $FWHM_{scatter}$ is calculated using equation (*3.9*):

$$FWHM_{scatter} = 2\,k_M\,tan(\alpha_{scatter})$$

(*3.9*)

$FWHM_{scatter}$ can then be converted into the Gaussian distribution standard deviation σ_s value using equation (*3.10*) [24].

$$\sigma_s = \frac{FWHM_{scatter}}{2\sqrt{2\,ln2}} = \frac{FWHM_{scatter}}{2.35}$$

(*3.10*)

Figure 3-7A & B show diagrams of the scattering function in real space and **K**-space, respectively. Figure 3-7C shows plots of the scattering function for differing scatter angles ($\alpha_{scatter}$ = 1° and 6°), plotted in k_y and k_x.
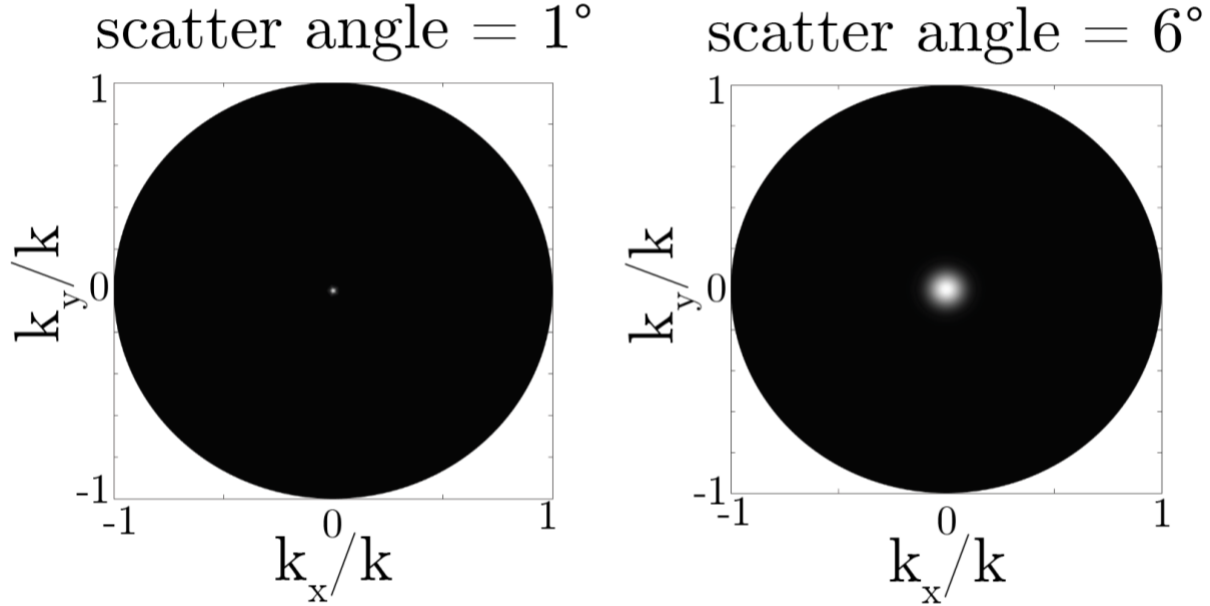
Figure 3-7 – Scattering topcoat in K-space, Matlab outputs: (Two-dimensional plots of the scattering function viewed from above, with $\alpha_{scatter} = 1°$ and $6°$ for (θ_{inc}, φ_{inc}) **=** (0,0). These functions apply for both scattering incident waves (S_{in}) and scattering reflected/outgoing waves (S_{out}). These plots are flattened images of functions which exist on the surface of a hemisphere with radius $k_x/k = k_y/k = k_z/k$.

3.1.3 Spectral calculation from Ewald's sphere

Once the **K**-space representations of the photonic film R and topcoat S_{in} and S_{out} are defined, they are implemented in the calculation of BRDF (*3.11*).

$$I\,(\theta_{inc}, \varphi_{inc}, \theta_{obs}, \varphi_{obs}, \lambda) =$$

$$\int_0^{2\pi} \int_0^{\frac{\pi}{2}} \int_0^{2\pi} \int_0^{\frac{\pi}{2}} S_{in}(\theta_{inc}, \varphi_{inc}, \theta_1, \varphi_1)\, R(\theta_1, \varphi_1, \theta_2, \varphi_2, \lambda)\, S_{out}(\theta_2, \varphi_2, \theta_{obs}, \varphi_{obs})\, d\theta_1\, d\varphi_1\, d\theta_2\, d\varphi_2$$

(3.11)

The scattering behavior of the photonic film is calculated via function $R(k_x, k_y, k_z)$ using Ewald's sphere *(3.12)* as introduced in section 2.4.3.

$$\Delta\mathbf{K} = k_0(\vec{s}_{out} - \vec{s}_{in})$$

(3.12)

Incident waves on the photonic film of direction $\vec{s_{in}}$ and wavenumber k_0 are the result of scattered waves from $S_{in}(\theta_{inc}, \varphi_{inc}, \theta_1, \varphi_1)$ at fixed (θ_{inc}, φ_{inc}). The scattered light waves at direction $\vec{s_{out}}$ have wavenumber k_0. $\Delta\mathbf{K}$ is the vector difference between an incident

light wave vector and a scattered light wave vector, and it can be defined in **K**-space as a vector (k_x, k_y, k_z). Many vectors (k_x, k_y, k_z) are input into $R(k_x, k_y, k_z)$ equation *(3.2)* to find the scattering behavior of the photonic material for all (θ_1, φ_1) and (θ_2, φ_2).

The product $R(k_x, k_y, k_z)$ $S_{in}(\theta_{inc}, \varphi_{inc}, \theta_1, \varphi_1)$ is calculated for each (θ_1, φ_1) and summed across (θ_1, φ_1), for discrete integration over (θ_1, φ_1). This product is then multiplied by $S_{out}(\theta_2, \varphi_2, \theta_{obs}, \varphi_{obs})$ for each (θ_2, φ_2) and summed across (θ_2, φ_2), for discrete integration over (θ_2, φ_2).

The area differential solid angles $d\theta_1$, $d\varphi_1$, $d\theta_2$, $d\varphi_2$ are given by the resolution of an icosphere mesh, derived from Wil O.C. Ward's icosphere technique, where the density of points on a half-sphere is defined by the mesh grid resolution [28]. The mesh grid is illustrated in Figure 3-8.
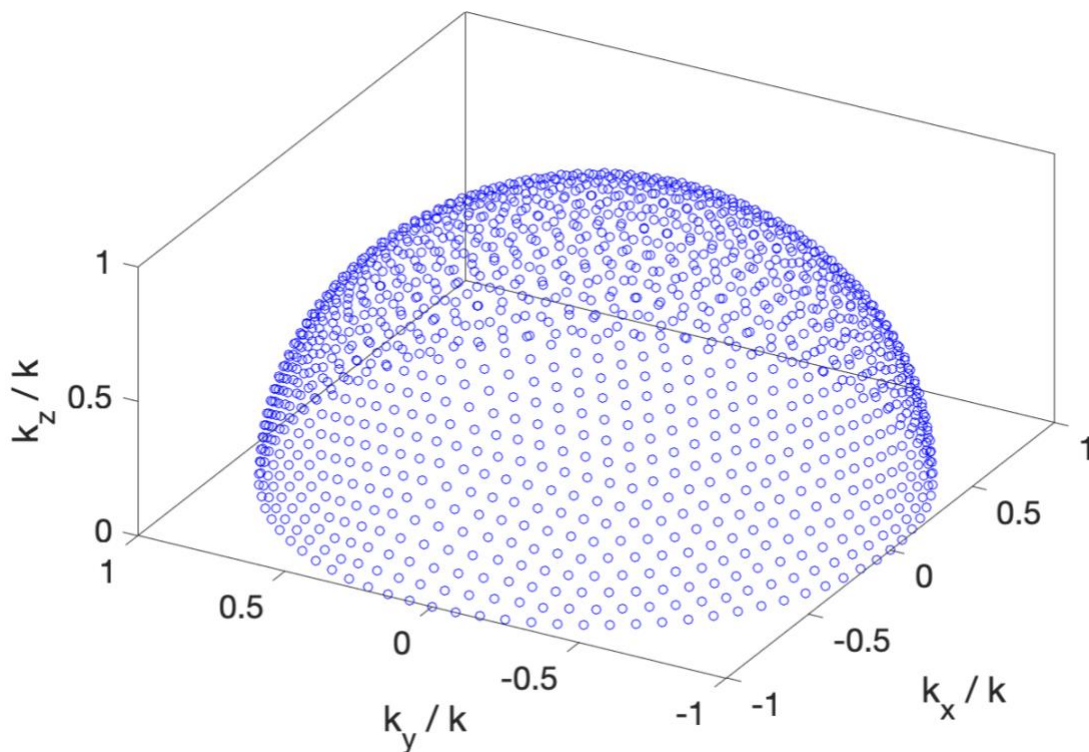

Figure 3-8 – Icosphere integration mesh: For "mesh grid resolution = 4."

The BRDF integration is conducted using for loops in Matlab, which outputs reflectance spectra (intensity I % vs. wavelength λ typically between 400 and 700 nm) for one specified angle of incidence (θ_{in}, φ_{in}) at a hemispherical range of angles of observation (θ_{obs}, φ_{obs}) between $0 \leq \theta_{obs} \leq \frac{\pi}{2}$, $0 \leq \varphi_{obs} \leq 2\pi$. The resolution of the angles of observation $d\theta_{obs}$ and $d\varphi_{obs}$ can be specified in the model. Reflectance spectra can be easily visualized as visible colors and plotted as points on the surface of a hemisphere, where the sample sits at the center point.

3.1.4 Visualization of optical properties and appearance

The BRDF integration discussed above outputs reflectance spectra at each angle of observation (θ_{obs}, φ_{obs}). For simulation of optical properties and appearance, spectra are first converted to XYZ values using the CIE tristimulus curves, which relate to the spectral response of human color vision [29, 30]. This conversion is well documented [31, 32]. XYZ values are then converted to RGB values using Matlab's xyz2rgb function with a standard D65 illuminant [32, 33].

Finally, RGB values are plotted as colors in a top-down polar diagram, or a hemisphere viewed from above. Additionally, spectra at angles of observation of interest can be plotted as reflectivity (%) vs. wavelength λ. The model appearance predictions are displayed in Section 3.3 using scattering parameters presented in Section 3.2.

3.2 Scattering parameters from empirical measurements

Empirical measurements of scattering angles – described in section 4.1 – were used to define a representative design space of four samples based on their scattering angles. The scattering angle of the rough topcoat is defined as α. The scattering angles of the reflector surface used in holographic manufacture of the photonic film are defined as βx and βy, scattering angles in the x-direction and y-direction respectively. A matrix of four samples with scattering angles is listed in Table 3-1.

Table 3-1 – Scattering angle parameters from empirical measurements

Flat topcoat - Flat photonic structure	Rough topcoat - Flat photonic structure
α = 1.0° βx = 0.01° βy = 0.01°	α = 3.8° βx = 0.01° βy = 0.01°
Flat topcoat - DIffuse photonic structure	**Rough topcoat - Diffuse photonic structure**
α = 1.0° βx = 2.6° βy = 12°	α = 4.3° βx = 12° βy = 26°

3.3 Model results

Four samples were for modeled using the scattering angle parameters defined in Section 3.2. The model was run for three angles of illumination θ_{inc} = 10°, 20°, and 30°. Figure 3-9 presents polar diagrams where reflectance spectra are represented as RGB colors on a hemisphere viewed from above. The model predicts the visual appearance of samples based on topcoat roughness and photonic film texture. Different appearances are visualized depending on these factors. A vocabulary is provided for systematically describing and categorizing these different appearances. This vocabulary links sample properties to the control factors of the material system (topcoat roughness and photonic film texture), helping to establish a design space for optical appearances.
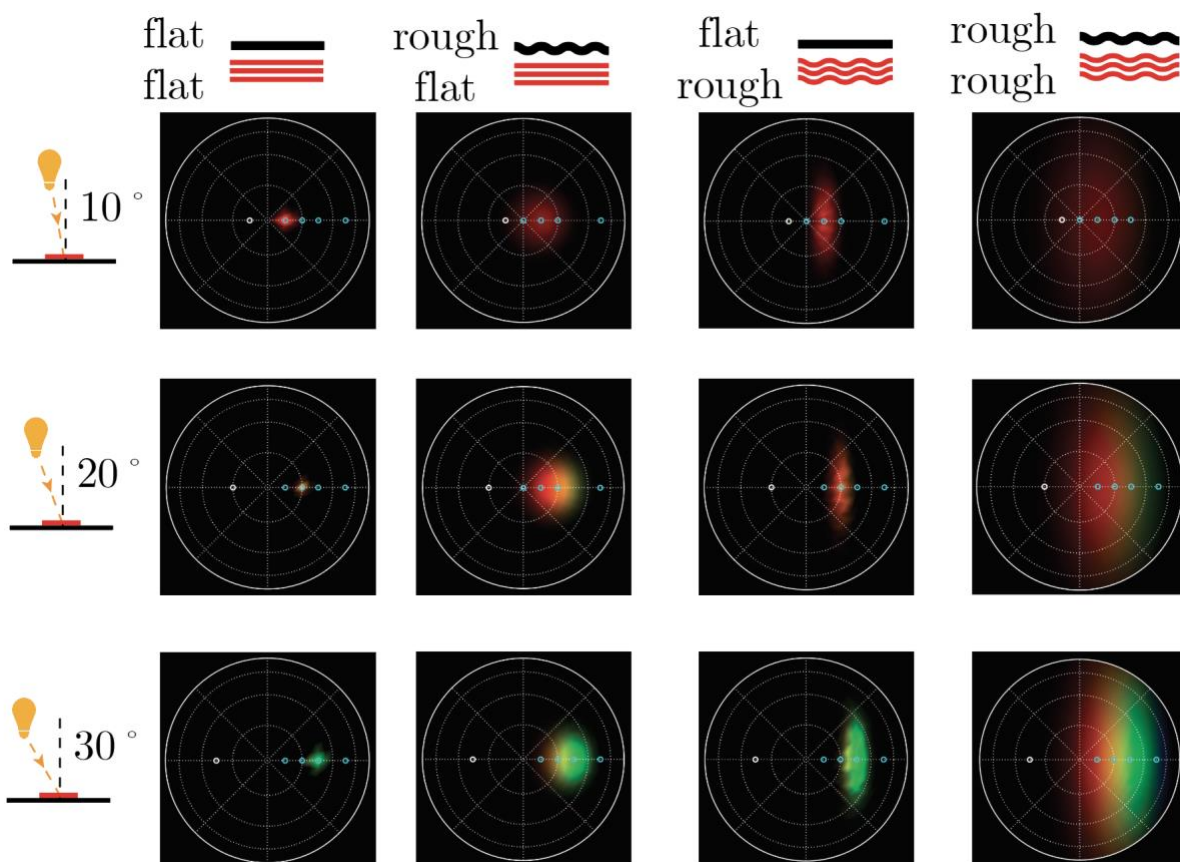
Figure 3-9 – Polar diagrams of intensity and color of reflected light for four sample configurations: Polar diagram outputs from model. Simulations were performed at three illumination conditions (θ_{inc} = 10°, 20°, and 30°). The incident light direction/position is marked by a small white circle on the left half of each image. The blue dots mark the locations of sampled spectra, which are the data sources of the measurements presented in Table 3-2. The images were uniformly scaled by a "brightness factor" in MatLab for greater visibility. α is the scattering angle of the rough topcoat. βx and βy are the scattering angles of the reflector surface used in optical manufacture in the x-direction and y-direction respectively. Sample parameters are as

follows: *Flat-flat* α = 1°, βx = βy = 0.01°. *Rough-flat* α = 3.8°, βx = βy = 0.01°. *Flat-rough* α = 1.0°, βx = 2.6°, βy = 12°. *Rough-rough* α = 4.3°, βx = 12°, βy = 26°.

3.4 Descriptors of optical appearance

To design optical appearances based on photonic film texture and topcoat roughness, a clear vocabulary is needed for two purposes: (1) describing objective reflectance spectrum characteristics independent of vision system, and (2) detailing appearance as visually perceived by humans. This vocabulary will allow any designer to efficiently select parameters for a desired optical appearance.

Objective, vision-agnostic descriptors include reflectance, spectral width, and spectral position. Figure 3-10 illustrates reflectance, spectral position, and spectral width for a sample spectral peak. Human-vision-specific descriptors include brightness, hue, saturation, diffuseness, and iridescence. Definitions for these descriptors are provided below:

Vision-agnostic descriptors:
- Reflectance is the ratio of the intensity of light reflected by a surface to the intensity of light incident on the surface. It is manifested in the height of the peak reflection strength in the surface's spectral signature. Reflectance is often given in percentages (0 – 100%) or absolute fractions (0 – 1). Measurements often use a reflective reference surface with near-100% reflectivity, such as a silver mirror.
- Spectral position and spectral width describe a material's ability to reflect light within a specific spectral band. Spectral position indicates the center of a reflectance peak, and spectral width measures the peak's the full-width half maximum (FWHM). A small spectral width corresponds with perceived pure colors [34].
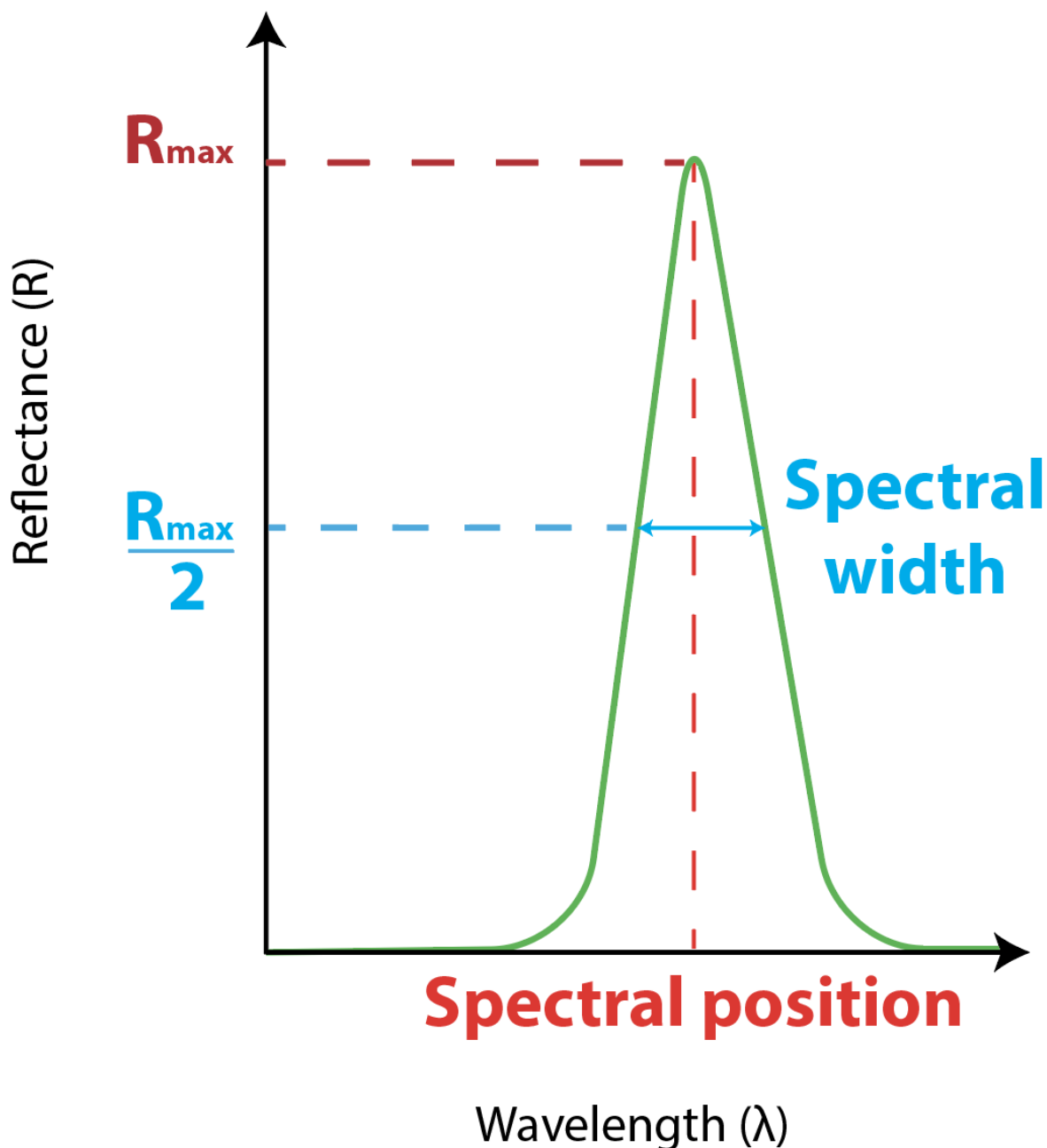
Figure 3-10 – Reflectance, spectral position, and spectral width: Reflectance (R_{max}) is the maximum intensity of a spectral peak. Spectral position is the wavelength position at R_{max}. Spectral width is the FWHM. Adapted from [34].

Vision-specific descriptors:
- Brightness is an attribute that describes the perceived reflectance of a material, in the case of the photonic materials in this thesis [20].
- Hue is an attribute that describes the color of an object in reference to its reflection spectrum.

- Saturation is an attribute that describes the spectral purity (bandwidth) of an object's color. More saturated colors have narrower spectral widths [34].
- Diffuseness is a perceived metric for the angular spread of observable light. Diffuseness [35] is defined as the percentage of a 2π hemisphere that is covered by observable light. The "observable light" threshold for a human or non-human detector is defined as the boundaries when observed light is indistinguishable from background noise or darkness.
- Iridescence is a perceived optical characteristic of the change in hue when varying observation and/or illumination angles. Angular dependency of hue is a quantifiable attribute of an object's iridescence. Three different scenarios are distinguished when describing angular dependency of hue:
  - Change in hue as a function of observation direction, for a fixed illumination direction
  - Change in hue as a function of illumination direction, for a fixed observation direction
  - Change in hue as a function of illumination and observation directions while satisfying the angular constraint of specular reflection ($\theta_{inc} = \theta_{obs}$)

These descriptors were used to compare the modeled material configurations and are expected to help material designers quantitatively stake out the corners of a representative design space of textured photonic films with rough topcoats.

3.5 Four archetypal samples

Our material system has two simple control handles for tuning optical appearance: the roughness of a transparent topcoat and the roughness of the reflector surface used for the holographic manufacture of the structurally colored elastomer, which determines its photonic texture. A matrix of four archetypal sample morphologies is presented in Figure 3-11. These samples represent the primary differences in the two parameters (photonic texture and topcoat roughness).

A sample made with a flat topcoat profile and a mirror-like photonic structure is referred to as "*flat-flat.*" A sample made with a rough topcoat profile and a mirror-like photonic structure is referred to as "*rough-flat.*" A sample made with a flat topcoat profile and a diffuse photonic structure is referred to as "*flat-rough.*" A sample made with a rough topcoat profile and a diffuse photonic structure is referred to as "*rough-rough.*"

flat ▬▬ **flat** ▬▬ • small diffuseness • high reflectance • narrow spectral width • bright and saturated color • high angular dependence of hue at $\theta_{inc} = \theta_{obs}$	**rough**〰〰 **flat** ▬▬ • higher diffuseness • smaller reflectance • broader spectral width • less bright, less saturated color
flat ▬▬ **rough** 〰〰 • higher diffuseness • smaller reflectance • narrow spectral width • less bright, saturated color	**rough** 〰〰 **rough** 〰〰 • highest diffuseness • smallest reflectance • broadest spectral width • least bright, least saturated color

Figure 3-11 – Archetypal sample matrix: Each sample archetype is represented by a symbol, with black lines for the topcoat profile and red lines for the photonic film. *Flat flat* corresponds with the sample made using a flat casting surface for the topcoat profile and a flat mirror for the photopolymer photonic structure. *Rough rough* corresponds with the sample made using a rough casting surface for the topcoat profile and a diffuse mirror for the photonic structure.

The *flat-flat* sample transmits most incident light at the flat topcoat surface. Incident light at a single direction then encounters the flat photonic surface and is filtered according to its angle of incidence. Waves of a single wavevector are transmitted through the topcoat surface. The result is bright and pure color visible at a single angle of observation.

The *rough-flat* sample scatters incident light at the topcoat surface, as shown in Figure 1-1. Many incident light waves at varying directions then encounter the flat photonic surface and are filtered according to their angle of incidence, leading to a broadened spectral distribution. The spectral and angular distribution of light is scattered at the

topcoat surface on its exit path out of the material. The result is a broad spectral distribution and broad angular distribution of light.

The *flat-rough* sample transmits most incident light at the topcoat. Incident light of a single direction then encounters the rough photonic surface and is filtered according to its angle of incidence and the relative distribution of angled photonic elements, leading to a broadened angular distribution. The angular distribution of light of a fairly uniform spectral width transmits out of the topcoat surface. The result is an angular distribution of light with slightly broadened spectral width.

The *rough-rough* sample scatters incident light at the topcoat surface based on its roughness/surface profile. Many incident light waves at varying directions then encounter the rough photonic surface and are filtered according to their angle of incidence and the relative distribution of angled photonic elements, leading to a broadened angular distribution and broadened spectral distribution. Light is further broadened in angular direction by scattering at the topcoat surface on its exit path out of the material. The result is a broad spectral distribution and broad angular distribution of light, which can be color constant and observable from many angles.

Metrics were measured for all four samples' model results and the tabulated values are presented below in Table 3-2. These metric values are later compared with experimental values and additional modeling results in Chapter 4 Figure 4-17.

Angular dependency of hue as a function of observation direction was measured at fixed angle of incidence $\theta_{inc} = 20°$ as the average of the change in spectral position λ_p while changing θ_{obs} between 10° and 30°. Angular dependency of hue as a function of illumination direction was measured at fixed angle of observation $\theta_{obs} = 20°$ as the average of the change in λ_p while changing θ_{inc} between 10° and 30°. Angular dependency of hue as a function of observation and illumination directions (at specular constraint $\theta_{inc} = \theta_{obs}$) was measured as the average of the change in λ_p while changing θ_{inc} and θ_{obs} between 10° and 30°. Spectral width was measured in Matlab as the average of all spectra at $\theta_{inc} = 10°$, 20°, and 30°, and $\theta_{obs} = 10°$, 20°, 30°, and 50°. Diffuseness was measured using Adobe Illustrator, where the threshold of observable light was determined by eye as the boundary when colored pixels were indistinguishable from black pixels. Reflectance was measured as the maximum reflectivity % of all collected spectra, normalized by the unit solid angle (Ω) of the model, determined by the integration resolution $d\theta_{obs} = 5°$ and $d\varphi_{obs} = 10°$ ($\Omega \approx 50$ sq. degrees).

Table 3-2 – Measured optical properties for archetypal samples: The optical property metrics are tabulated for (left to right) *flat-flat*, *rough-flat*, *flat-rough*, and *rough-rough* samples. Sample parameters are as follows: *Flat-flat* α = 1°, βx = βy = 0.01°. *Rough-flat* α = 3.8°, βx = βy = 0.01°. *Flat-rough* α = 1.0°, βx = 2.6°, βy = 12°. *Rough-rough* α = 4.3°, βx = 12°, βy = 26°. Optical properties are angular dependency of hue for changing observation direction ("Obs. Hue"), angular dependency of hue for changing illumination direction ("Ill. Hue"), angular dependency of hue for changing observation and illumination direction ("Spec. Hue"), spectral width, diffuseness, and reflectance.

	flat-flat	rough-flat	flat-rough	rough-rough
Obs. Hue (Δnm/Δ°)	–	1.50	0.00	1.78
Ill. Hue (Δnm/Δ°)	–	3.25	–	2.00
Spec. Hue (Δnm/Δ°)	3.50	3.00	3.50	3.75
Spectral width (nm)	10.0	22.1	14.0	33.0
Diffuseness (% of 2π)	1.12%	8.34%	6.85%	42.7%
Reflectance (max %/sq. deg.)	1.0	0.2	0.4	0.04

Flat-flat and *flat-rough* have such narrow viewing angles that angular dependency of hue for changing illumination direction is not applicable. Notably, *flat-rough* has zero angular dependency of hue for changing observation direction because λ_p remained constant for θ_{obs} = 20°; λ_p also remained constant for θ_{obs} = 10° and θ_{obs} = 30°.

These results are most consistent with our hypotheses for the *flat-flat* and *rough-rough* samples. The *flat-flat* sample has high angular dependency of hue for specular constraints, pure color, and small diffuseness. The *rough-rough* sample has a significantly broadened spectral width, the lowest reflectance, and high diffuseness. *Rough-flat* and *flat-rough* do have broadened spectral width and diffuseness as well as lower reflectance, but the quality of such optical properties was difficult to hypothesize beyond that, especially for the angular dependency of hue. Preliminarily, the model allows for visualization and prediction of the optical characteristics of materials as a function of their photonic texture and topcoat roughness, and these results must be confirmed experimentally.

Chapter 4: Experimental Validation of the Model's Appearance Predictions

The model's appearance predictions were validated experimentally by fabricating and characterizing four representative samples of textured photonic structures with topcoats, using materials with empirically measured scattering angles. Characterization data was obtained by spectroscopic analysis and imaging of the angular scattering distribution. The model was further used to define the outer extents of the design space. Discussion is presented on the agreement of the model's predictions with the experimentally achieved visual appearance and optical properties, as well as limitations of this material system.

4.1 Empirical measurements of scattering angles and materials selection

Several materials were tested and characterized to better understand the scattering behavior of rough topcoats and rough mirrors. Measurements were taken of the scattering cone angle of light transmitting through translucent rough surfaces and of light reflecting off rough reflective surfaces.

4.1.1 Characterization of scattering behavior in reflection

To determine the ideal photonic structure for the desired optical properties, multiple reflective surfaces were characterized. The scattering behavior in reflection was measured by illuminating a reflective material sample using an Ocean Optics halogen HL2000 lamp with an optical fiber and collimating lens at a fixed position and angle, as in Figure 4-1. The scattered light was collected on a uniform white sheet of paper (100# cover white matte cardstock), which was imaged at multiple distances along a sliding 80-20 track using a Canon EOS Rebel T3i DSLR camera with an EFS 18-55mm lens. Images were taken in a dark room, with constant exposure and numerical aperture.

The resulting images, seen in Figure 4-2 A-C, were processed in ImageJ to measure the cross-sectional profile of scattered light. Light profiles were processed in Matlab and FWHM was measured, seen in Figure 4-2 D-F. The scattering angle of a given sample surface profile was determined by calculating the change in FWHM at multiple distances as a trigonometric angle.

Three materials of interest were selected for their different surface roughness: Stainless steel 304 with a no. 4 brush finish, or "brushed stainless"; 18-8 stainless steel shim stock, or "18-8 stainless"; multipurpose 304 stainless steel, or "304 stainless." Results for these three materials are reported in Table 4-1.
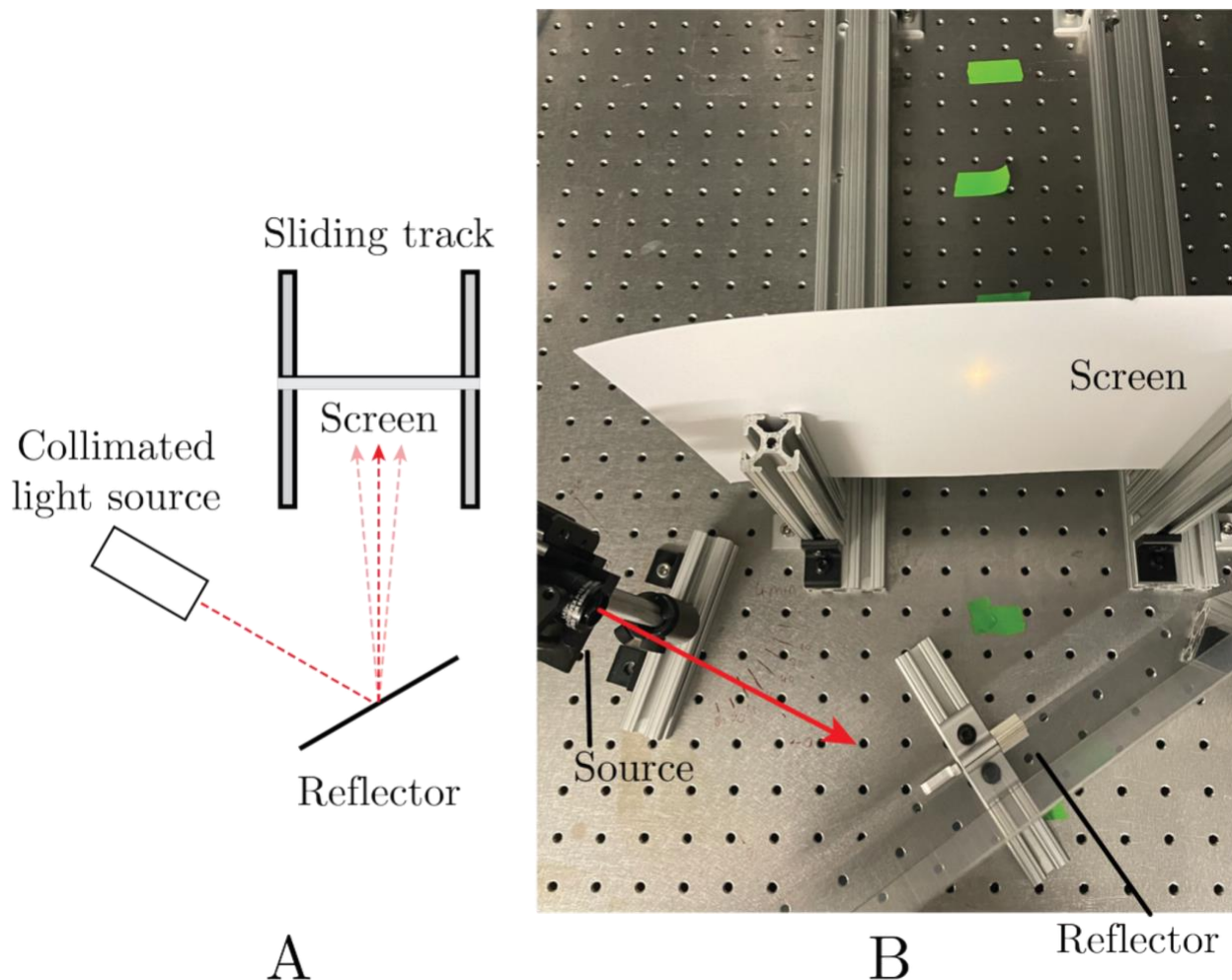

Figure 4-1 - Setup for scattering measurements in reflection: (A) Diagram of setup for collecting scattering behavior of reflective materials. A collimated light source illuminates the reflective surface, and the scattered beam is captured on a paper screen. The scattered beam can then be imaged with a camera from multiple positions by adjusting the screen distance along the sliding track. **(B)** The constructed setup, with green tape marking particular distances. In this case, the reflective material is angled at roughly +30° relative to the screen (counterclockwise rotation) and the light source is -30° relative to the screen (clockwise rotation).
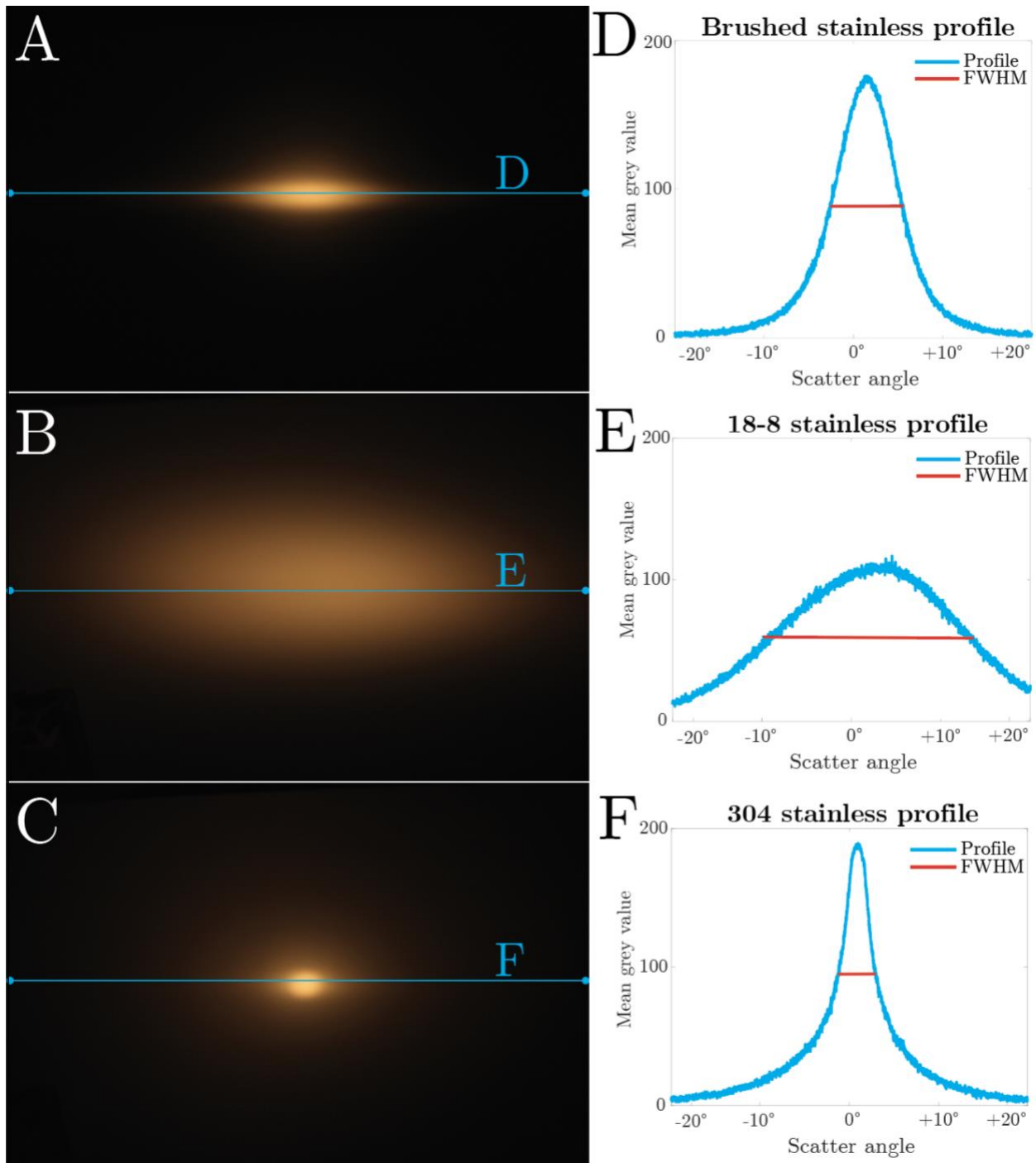
Figure 4-2 - Results of scattering in reflection: (A - C) Images of scattering behavior of **A** brushed 304 stainless steel, **B** 18-8 stainless steel, and **C** multipurpose 304 stainless steel, in reflection. Images taken at 14 cm distance. (**D - F**) Corresponding profile plots of scatter angle, measured horizontally across the center of each image.

Table 4-1 – Empirical reflection scattering angle measurements

Material	Reflection		
	Brushed stainless	18-8 stainless	304 stainless
β_x (Horizontal scattering angle)	2.61°	12.13°	1.24°
β_y (Vertical scattering angle)	11.97°	26.11°	2.37°

Two different reflective surfaces were selected for *flat-rough* and *rough-rough,* to effectively differentiate the optical properties and appearances of the samples with rough photonic texture. 18-8 stainless steel was selected for the *rough-rough* sample due to its large scattering cone angle, which maximizes diffuse scattering and thus highlights the texture of the photonic structure. This choice ensures that the *rough-rough* sample exhibits the most pronounced diffuse texture. On the other hand, brushed stainless steel, with a smaller but still diffuse scattering cone, was chosen for the *flat-rough* sample to provide a less intense but still significantly diffuse reflective surface. This allows for a clearer comparison of how a less pronounced diffuse texture affects the optical appearance relative to the *rough-rough* sample.

While both brushed stainless steel and 18-8 stainless steel have larger scattering angles in one direction (based on their grain direction), this anisotropy can be accounted for in the model.

4.1.2 Fabrication of rough topcoats and characterization of scattering behavior in transmission

Castings of multiple surface profiles were made and characterized. Surface profiles were cast using a two-part silicone polymer (SmoothOn Solaris), which was mixed 1:1 by weight and degassed for 10 minutes in a vacuum chamber. Casting surfaces, e.g. frosted P95 acrylic, were covered in silicone polymer in roughly 1" x 1" area and left to cure for 24 hours at room temperature. The casting cured into a thin transparent piece which scatters light based on the surface profile characteristics when illuminated in transmission.

The scattering behavior in transmission was measured by illuminating a sample using an Ocean Optics halogen HL2000 lamp with an optical fiber and collimating lens at a fixed position, as in Figure 4-3. The scattered light was collected on a uniform white

sheet of paper (100# cover white matte cardstock, selected for its uniformity compared to other lightweight paper screens), which was imaged at multiple distances along a sliding 80-20 track using a Canon EOS Rebel T3i DSLR camera with an EFS 18-55mm lens. Images were taken in a dark room, with constant exposure and numerical aperture.
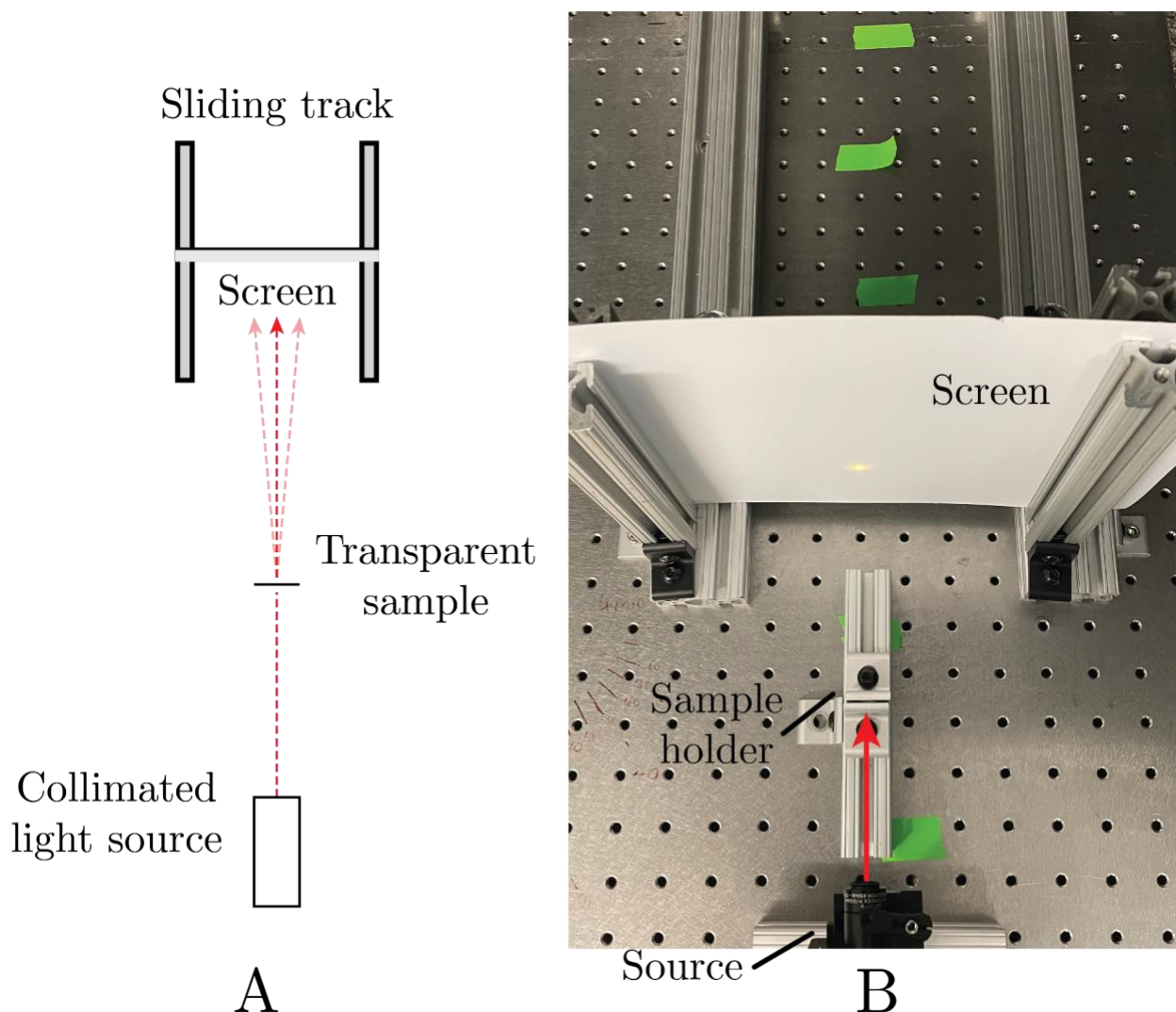

Figure 4-3 - Setup for scattering measurements in transmission: (A) Diagram of setup for collecting scattering behavior of transparent castings of rough surfaces. A collimated light source illuminates the transparent sample, whose rough surface scatters the beam which is then captured on a paper screen. The scattered beam can then be imaged with a camera from multiple positions by adjusting the screen distance along the sliding track. **(B)** The constructed setup. A transparent sample is laminated onto a glass slide which is held in the sample holder.

The resulting images, seen in Figure 4-4 A-C, were processed in ImageJ to measure the cross-sectional profile of scattered light. Light profiles were processed in Matlab and

the full-width half maximum (FWHM) was measured, seen in Figure 4-4 D-F**.** The scattering angle of a given sample surface profile was determined by calculating the change in FWHM at multiple distances as a trigonometric angle.

Three materials of interest were selected for their different surface roughness: blue vinyl plastic, frosted P95 acrylic sheet and 3M Magic™ Tape. Results for these three materials are reported in Table 4-2.
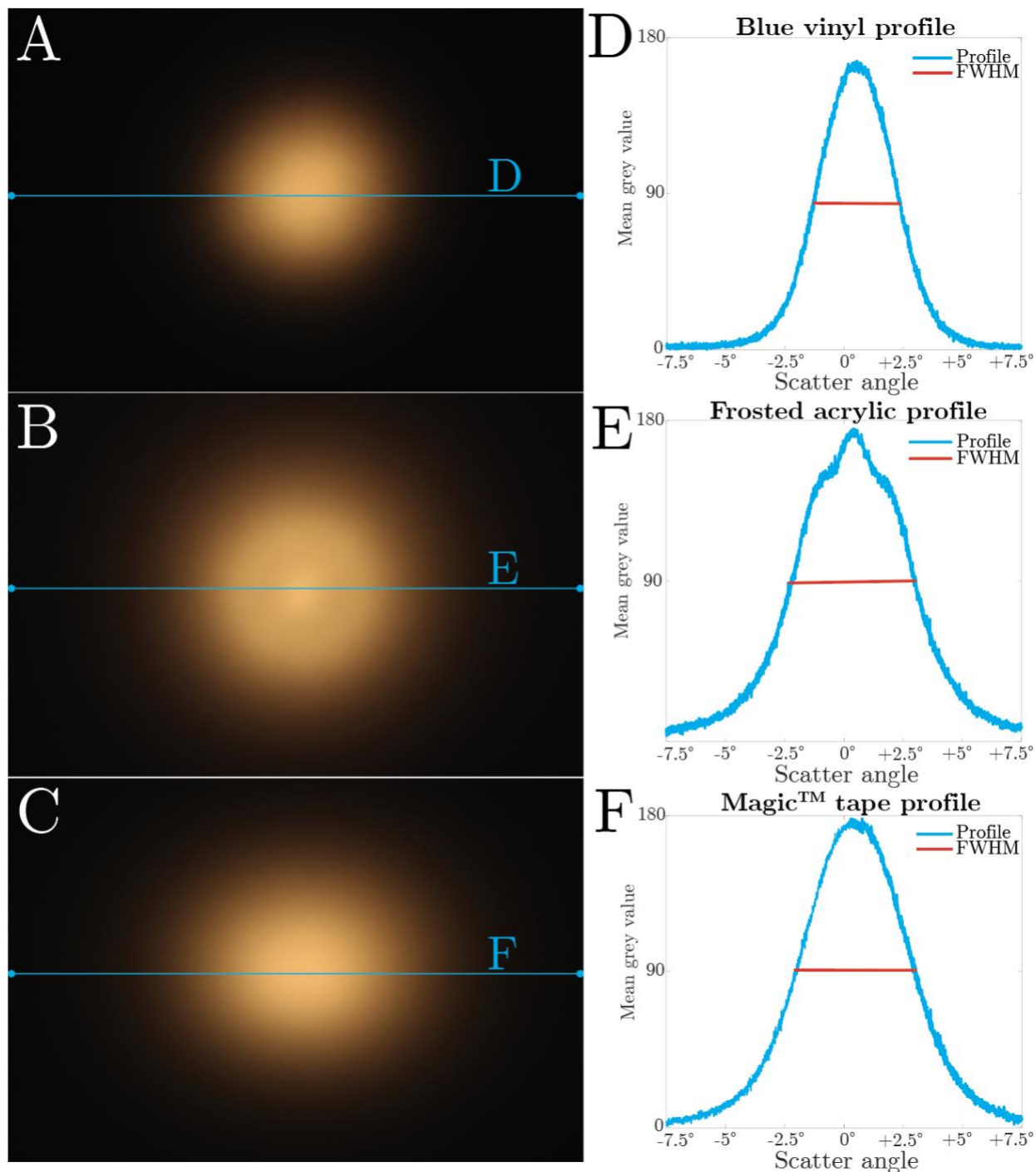
Figure 4-4 - Results of scattering in transmission: (A - C) Images of scattering behavior of transparent castings of **A** blue vinyl, **B** frosted acrylic, and **C** Magic™ Tape in transmission. Images taken at 14 cm distance. (**D - F**) Corresponding profile plots of scatter angle, measured horizontally across the center of each image.

Table 4-2 – Empirical transmission scattering angle measurements

Material	Transmission		
	Blue vinyl	Frosted acrylic	Magic™ tape
α_x (Horizontal scattering angle)	3.73°	6.67°	3.97°
α_y (Vertical scattering angle)	3.92°	6.16°	4.52°
$\alpha_{scatter}$ (Average scattering angle)	3.83°	6.42°	4.25°

Two different casting surfaces were selected to effectively contrast the optical properties and appearances of the rough topcoat samples. Blue vinyl was chosen for the *rough-flat* sample because it has the lowest scattering cone angle. This choice allows for a clear assessment of how a less rough, less diffusely scattering surface influences the appearance of the rough topcoat samples. Conversely, the surface with the highest scattering cone angle was selected for the *rough-rough* sample to maximize diffuse scattering. This choice highlights the effect of the rough topcoat by ensuring that light is scattered more widely.

Frosted acrylic was measured to have a larger scattering cone angle than 3M Magic™ Tape (6.42° vs. 4.25° respectively). While frosted acrylic may be theoretically better suited for demonstrating a larger design space due its larger scattering cone angle, the physical samples created using frosted plastic as a casting surface tended to cure poorly in comparison with the Magic™ Tape samples. Additionally, frosted acrylic was measured to have an irregular scattering profile (see protrusion shape in Figure 4-4E).

While the irregular scattering profile has the potential to be ultimately selected as a material advantage, simplicity in modeling suggests assuming uniformly Gaussian shaped scattering profiles. Thus, Magic™ Tape was selected as the casting surface for the *rough-rough* sample.

4.2 Fabrication of photonic structures with topcoats

Physical samples were created to experimentally validate the model and demonstrate physical products of controlled optical appearances, using the casting surfaces and reflective surfaces described in Section 4.1. The fabrication techniques employed for both photonic films and their topcoats are described. Specifics of the materials and tools used are detailed further in Appendix A.6.

4.2.1 Holographic manufacturing of photonic film

Photonic films were produced using Covestro Bayfol HX holographic photopolymer films, which were supplied in rolls sandwiched between a polyethylene (PE) protective layer and a cellulose triacetate (TAC) protective layer [36]. After removal of the PE, the film was placed photopolymer side down on a reflective surface and laminated using a flat rubber blade to remove any air bubbles and create a uniform surface. Preparation was conducted in the dark to prevent preemptive exposure of the photosensitive films.

Flat-flat and *Rough-flat* samples were made using an aluminum mirror (ThorLabs) as the reflective surface. *Flat-rough* samples were made using brushed 304 stainless steel as the reflective surface. *Rough-rough* samples were made using 18-8 stainless steel as the reflective surface. The specifics of the materials are detailed in Appendix A.6.

Holographic films were then exposed to light from an Epson VS250 projector with bandpass filters in the R, G, and B channels to increase temporal coherence. Films were 15 μm thick and the coherence length of the projector light was increased to produce a standing wave at least 15 μm long. Films were exposed to red light via a 255-0-0 image projected from a laptop computer for four minutes, as specified by procedure in Miller et al. [10] and seen in Figure 4-5. After exposure, the holographic films were laminated face-down on a clean TAC surface and flood-cured under ambient white light for a minimum of five minutes.
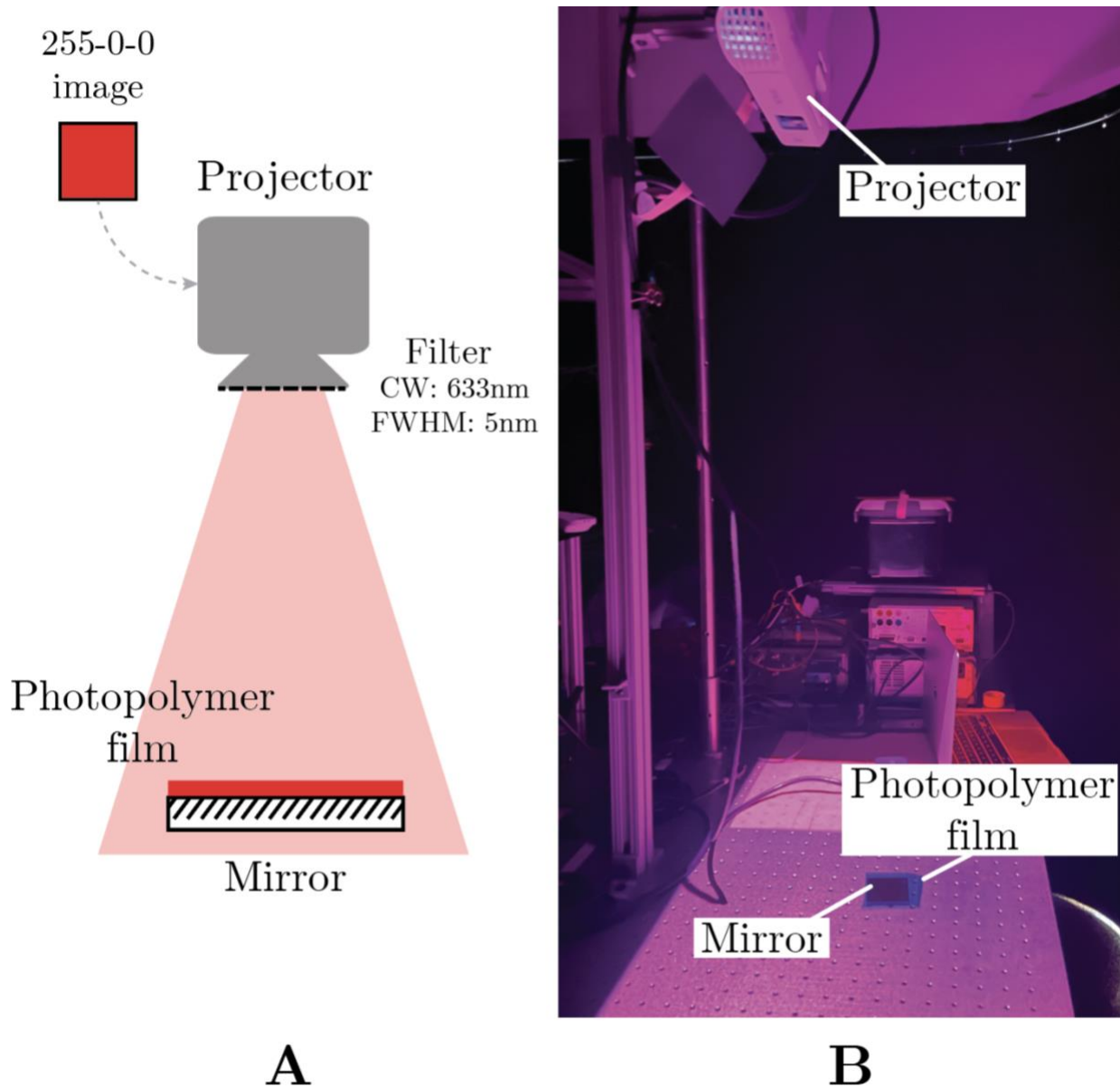
Figure 4-5 – Manufacturing setup for structurally colored film: (A) Diagram of setup for manufacturing structurally colored film. Photopolymer film is laminated to a reflective surface (mirror or other). A red image is sent to a modified desktop projector, which uniformly illuminates the film. **(B)** The constructed setup with a projector mounted overhead, illuminating the photopolymer film from above. Featured here is a 1"x1" aluminum mirror with a small sample of photopolymer film.

The holographic films were then plasma etched (10 cc/min O_2 flow rate at 200 mT for 1 min) to prepare bonding with a black backing silicone layer. After plasma etching, the films were laminated TAC side down on a glass template where Dow 700 black silicone adhesive was blade-cast at controlled thickness using shim stock spacers (total thickness of 500µm). Samples were left for 24 hours at room temperature to fully cure. After curing, the TAC protective coating was carefully peeled from the photopolymer

film. Samples of 1" x 1" photopolymer film were then prepared for top-coat casting by laminating onto a glass slide substrate, black backing side down.

4.2.2 Casting of scattering topcoats

1" x 1" photopolymer film samples were again plasma etched (photopolymer film face up) with conditions described in 4.2.1, to ensure proper adhesion of the photopolymer surface and the topcoat polymer. The topcoats were produced using a two-part transparent silicone polymer (SmoothOn Solaris), which was mixed 1:1 by weight and degassed for 10 minutes in a vacuum chamber. After degassing, silicone polymer was poured onto the photopolymer film just enough to cover the surface. Then, the casting surface was sandwiched on top, using binder clips with spacers of defined thickness on either side of the photopolymer to control the topcoat layer thickness (stacks of spacers each 250 µm thick). The setup can be seen in Figure 4-6. Samples were cured for 24 hours at room temperature.

Flat-flat and *Flat-rough* samples were made using a smooth acrylic sheet as the casting surface. *Rough-flat* samples were made using blue vinyl as the casting surface. *Rough-rough* samples were made using 3M Magic™ tape as the casting surface.
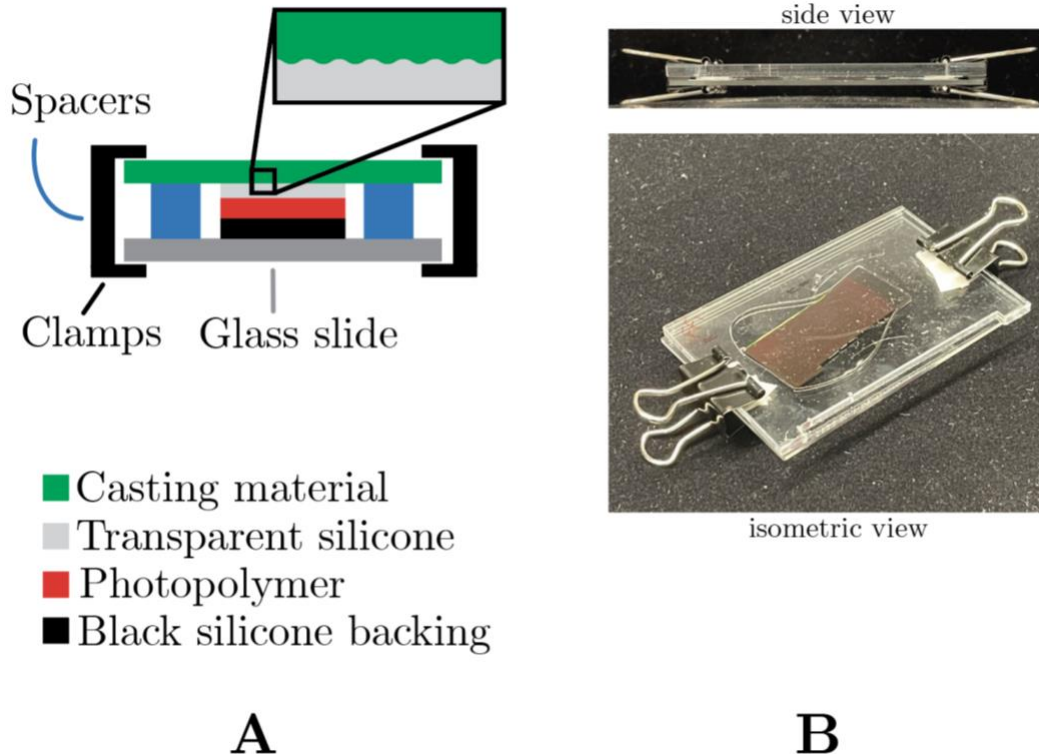
Figure 4-6 – Topcoat casting setup: (A) Diagram of setup for manufacturing samples with transparent topcoat. Transparent silicone polymer is poured onto photopolymer

film, with the black silicone backing underneath. The casting surface is sandwiched on top, using binder clips with spacers of defined thickness on either side of the photopolymer. Inset diagram demonstrates the profile of the original surface being cast by the transparent silicon polymer. **(B)** The constructed setup with four polystyrene spacers of thickness 250 µm each, viewed from the side and viewed isometrically.

4.3 Metrology of photonic structures with topcoats

Physical samples were characterized quantitatively to test the research hypothesis, validate the model results, and demonstrate control of visual appearance and optical properties. Visual appearances were imaged using a DSLR camera at fixed distance from the sample with varied angle of incidence (θ_{inc}, φ_{inc}). The angular distribution of reflected colors were imaged at many observation angles (θ_{obs}, φ_{obs}) using a DSLR camera at fixed distance with varied (θ_{inc}, φ_{inc}) of collimated light, where the reflected angular light distribution is imaged on the outside of a semi-translucent hemispherical screen. The spectral reflectance signature of samples was measured from several observation angles along one plane ($\varphi_{obs} = 0$) via reflectance spectra using a custom goniometric spectrometer.

4.3.1 DSLR imaging

Samples were imaged on a black felt background covered by a black cardboard mask, using a Godox SL60W lamp and diffuser with a Canon EOS Rebel T3i DSLR camera and EFS 18-55mm lens, as seen in Figure 4-7. A diffuser was used to reduce harsh specular reflections (glare) and better simulate natural lighting conditions while still capturing hue travel behavior. The angular range of the diffuser was roughly 90° (± 45° from the center incidence angle $\theta_{inc, center}$) [37]. At a fixed distance of roughly 2 feet above the sample, the samples were imaged under a ± 27° angular range of incident light.
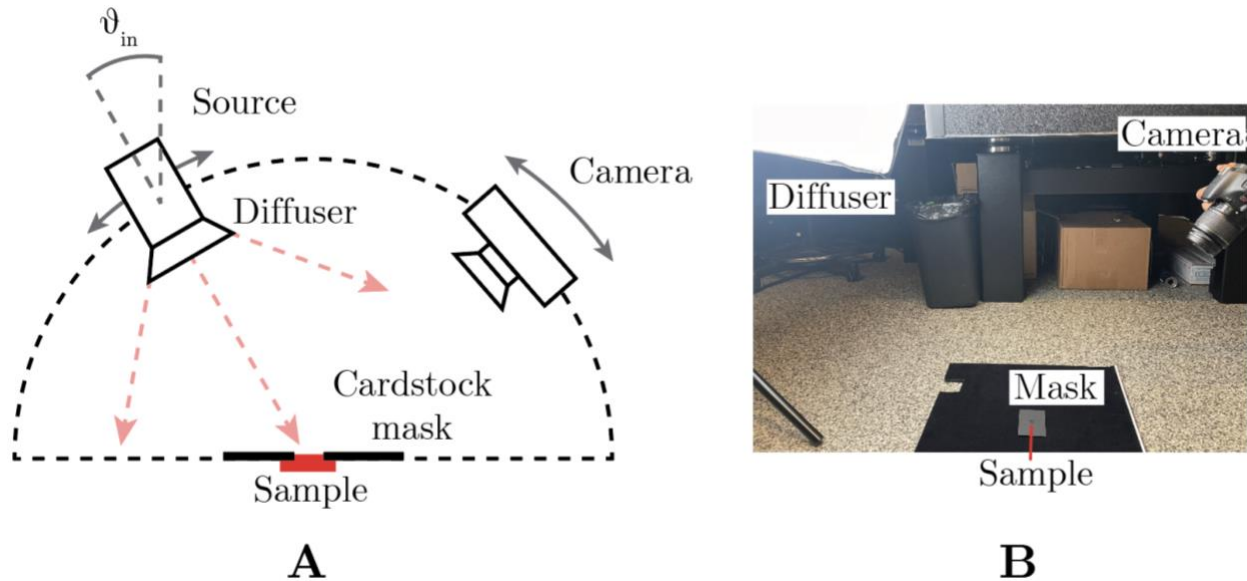
Figure 4-7 – Setup for imaging visual appearance: (A) Diagram of setup for imaging samples with DSLR camera. Samples are covered in a black cardstock mask with a square cut in the center. A lamp source with a diffuser illuminates the sample at center angle $\theta_{inc,\ center}$ fixed in the $\varphi_{obs} = 0$ plane, with diffuse light in an angular range of $\pm 27°$ from $\theta_{inc,\ center}$. Images were collected with the camera at various angles of observation θ_{obs}. **(B)** The constructed setup with a lamp positioned at roughly $\theta_{inc,\ center} = 10°$.

4.3.2 Angular scattering distribution

For the characterization of the angular scattering distribution, a standard ping pong ball was cut in half and "drilled" with a hot nail at the desired angle of incidence. The modified ping pong ball was then placed as a semi-translucent hemispherical screen over a sample, with the sample positioned at the spherical center. The sample was illuminated through the hole using an Ocean Optics halogen HL2000 lamp with optical fiber and a collimating lens positioned at the desired angle of incidence. The scattered light was collected on the internal surface of the ping pong ball, whose translucence allowed imaging of the light on the exterior surface using the Canon DSLR camera described in 4.3.1, positioned roughly 6" above the ping-pong ball, as seen in Figure 4-8. Images were taken in a dark room, with fixed numerical aperture & ISO and variable exposure/shutter speed based on the diffuseness of the sample.
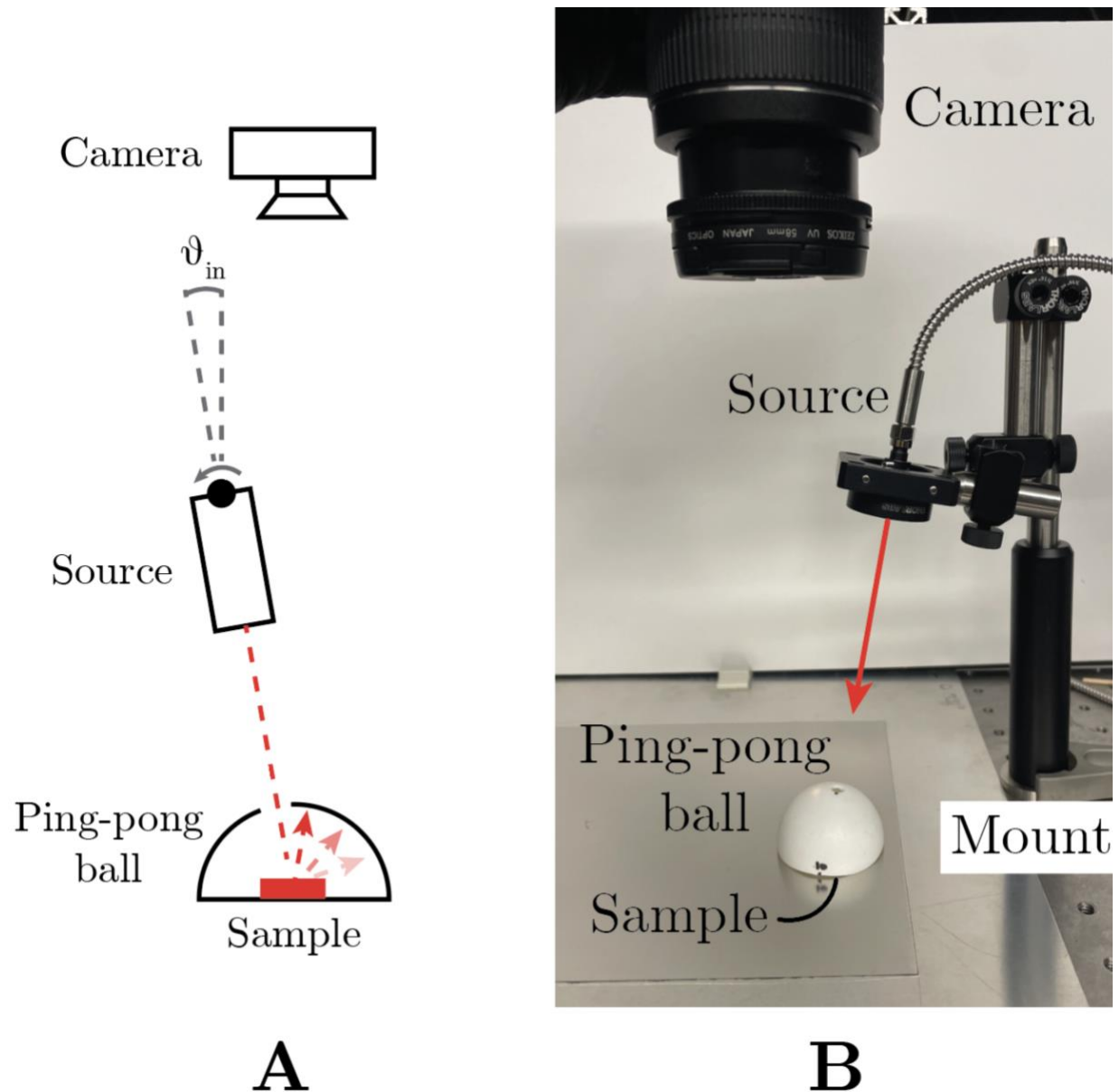
Figure 4-8 – Setup for imaging angular distribution: (A) Diagram of setup for imaging scattering behavior of samples. Sample is placed into the center point of a hemispherical ping-pong ball. The sample is illuminated by an angled source through a hole in the hemisphere's surface. Light reflects from the sample onto the interior surface of the hemisphere, whose translucence allows for imaging with a DSLR camera from above. **(B)** The constructed setup with the source angled at roughly 10°.

4.3.3 Custom goniometric spectrometer

For the collection of reflectance spectra, a custom variable angle spectrometer was assembled using multiple rotation stages, an XY stage, a dual-angle tilt stage, and

standard ThorLabs cage mounts, rods & posts. Spectra were collected using ThorLabs SLS201L source and a Maya 2000 Pro spectrometer at θ_{inc} and θ_{obs}, with $\varphi_{obs} = 0$.
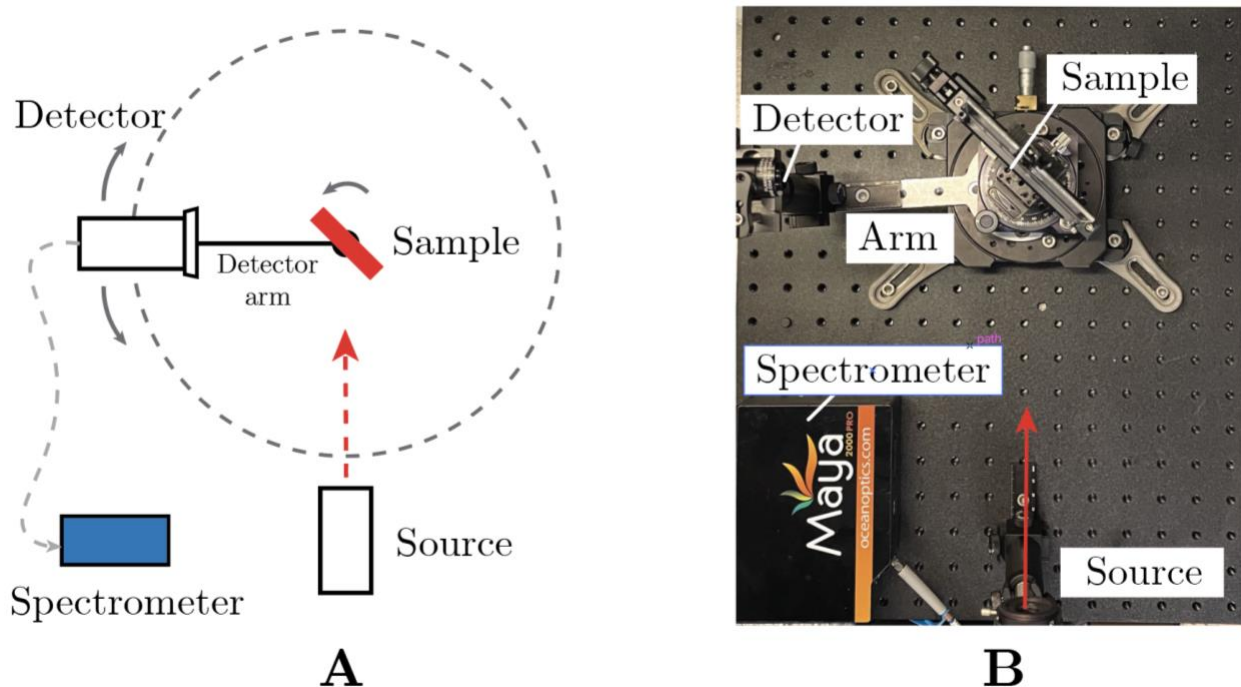
Figure 4-9 – Setup for goniometric spectroscopy: (A) Diagram of gonio-spectrometry setup for characterizing scattering behavior of samples. Sample is placed into a custom 3D printed sample holder at the device's center of rotation. The sample is illuminated by a fixed source. The reflected light is collected by a detector which sits on a rotating arm. Reflectance spectra were collected from many positions by rotating the sample holder and/or the detector. **(B)** The constructed setup with the sample angled at roughly 45°.

The data resulting from visual appearance assessment and spectroscopic analysis of the samples were used to validate the model's predictions of appearance and optical properties, with the results being discussed below.

4.3.4 Comparison of experimental data and model predictions

Figure 4-10 shows camera images of four different samples of photopolymer with transparent topcoats, as described in section 4.3.1. For all angles of incidence, each sample blue-shifts as the angle of observation increases. As the angle of incidence increases, the color at the specular condition also blue shifts. Considering the diffuseness of the source used in imaging, the discrepancy between the appearances presented in Figure 4-10 and Figure 4-11 suggests that collimated light sources at small $\theta_{inc} \leq 20°$ lead to stronger color constancy in the rough photonic texture samples.
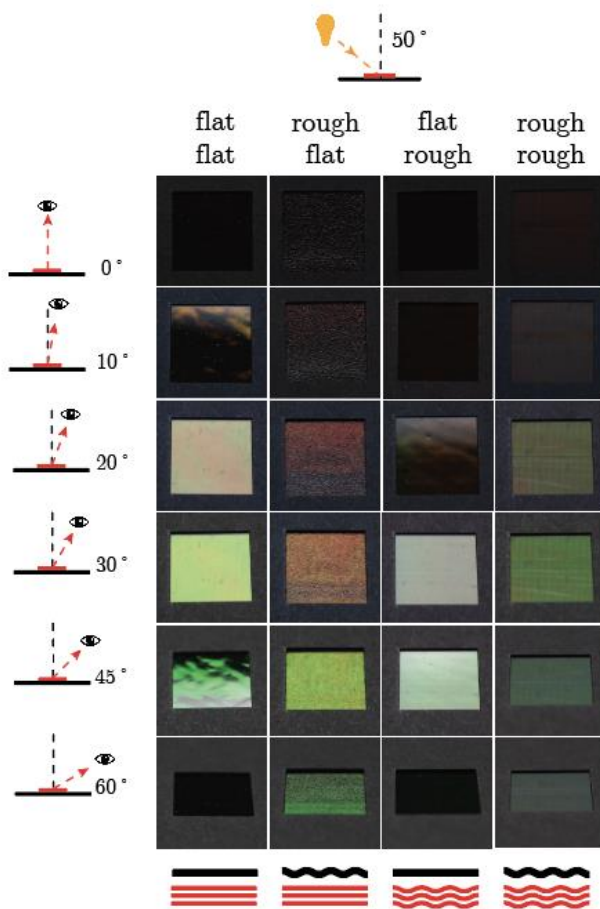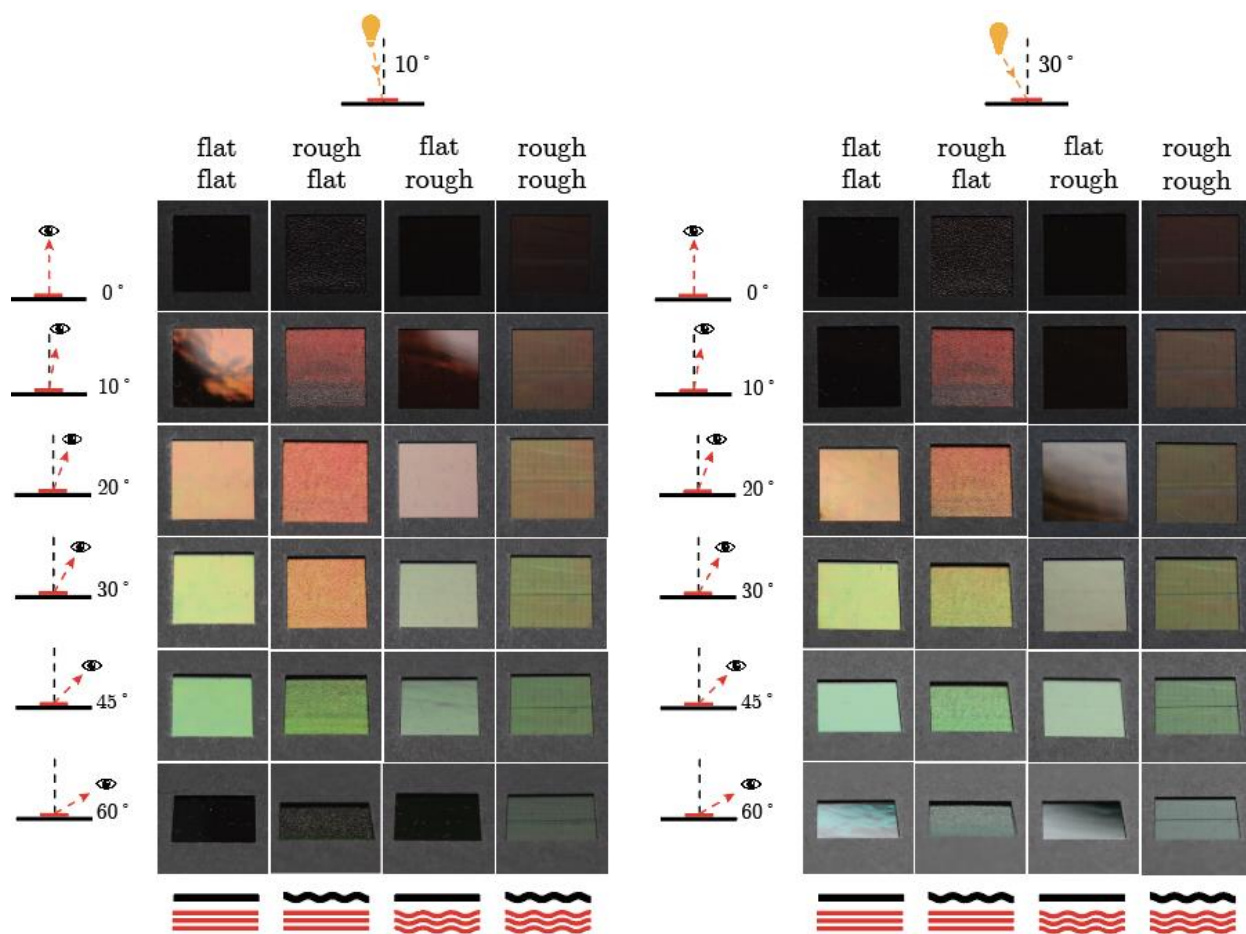
Figure 4-10 – Visual Comparison of Four Samples: Different samples are arranged in columns as *flat-flat, rough-flat, flat-rough, rough-rough*, in order from left to right. Moving down a column displays variation in visual appearance as the angle of observation θ_{obs} increases from 0° to 60°. Images in the top left block were taken with a diffuse illumination source at roughly θ_{inc} = 10°; the top right block at roughly θ_{inc} = 30°; and the bottom center block at roughly θ_{inc} = 50°. The samples were imaged under a ± 27° angular range of incident light, measured from θ_{inc}.

Figure 4-11 shows camera images of the reflected angular distribution from the ping pong ball setup from Section 4.3.2. As θ_{inc} increases, color tends to blue-shift. The viewing angles for *rough-flat* and *rough-rough* samples are broad. The *flat-rough* sample shows a bright white specular highlight. The rough photonic texture samples show angular color constancy at $\theta_{inc} \leq 20°$.
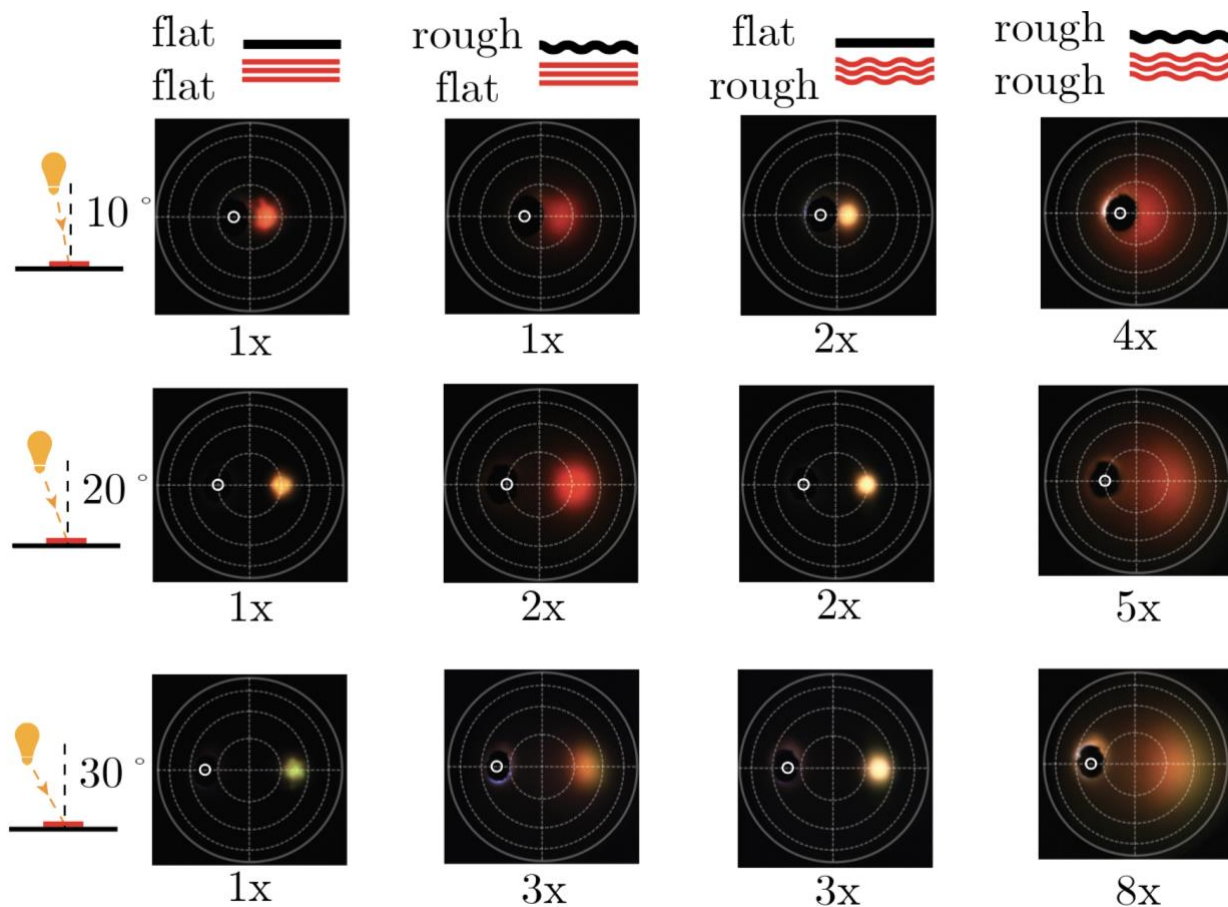
Figure 4-11 – Angular distribution and visual comparison of four samples: Camera images from ping-pong ball setup described in section 4.2.2. Images were taken at three illumination conditions (θ_{inc} = 10°, 20°, and 30°). The incident light direction/position is marked by a white circle in the left half of each image. The images have been normalized based on exposure condition, then scaled in MatLab for greater

visibility. The scaling factors are indicated under each image (e.g. "8x" means the data has been scaled by a factor of 8).

Figure 4-12 shows a comparison of all four samples based on their peak reflectivity per unit solid angle (Ω), measured as the maximum reflectivity percentage in both experimental ("Exp.") and model ("Model") results divided by the Ω of the detector/model resolution. The experimental Ω was determined by diameter of the detector iris aperture and the length of arm from detector to sample. The model Ω was determined by the resolutions $d\theta_{obs}$ and $d\varphi_{obs}$.

These data are represented on a logarithmic scale for reasonable comparisons of experimental and model data which, from sample to sample, have maximum reflectivities that differ by orders of magnitude. It is expected that as Ω of the model approaches that of the experiments (50 sq. degrees in the model vs. 0.5 sq. degrees experimentally), the data would be in better agreement, as discussed in section 4.5. While the maximum reflectivities per unit solid angle have orders of magnitude discrepancies between the model and the experiments, the relative trend between samples is similar: *flat-flat* has the highest value and *rough-rough* has the lowest, and *flat-rough* and *rough-flat* are in between.
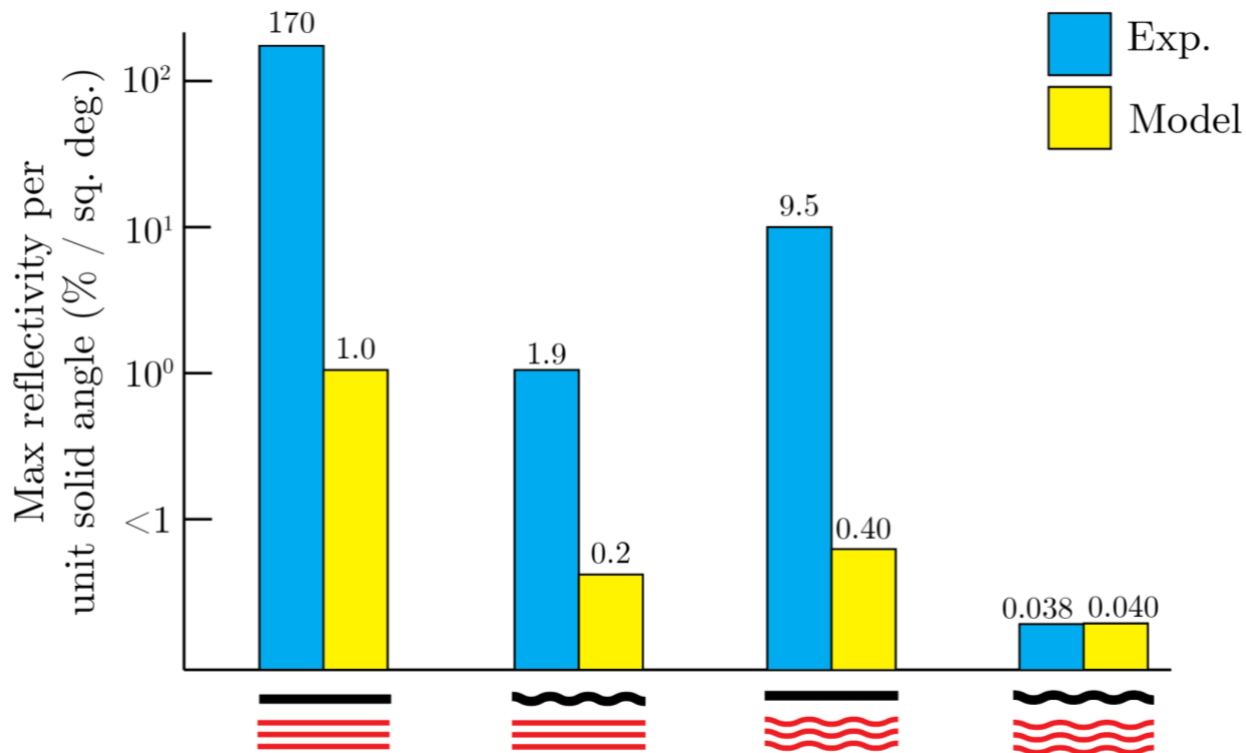
Figure 4-12 – Quantitative comparison of reflectance per unit solid angle: Bar graph comparing maximum reflectivity percentage per unit solid angle (Ω) of each sample. Note the y-axis logarithmic scale. As expected with energy conservation, the maximum

intensity per Ω decreases as light is reflected more diffusely, from *flat-flat* to *rough-rough*.

Figures 4-13, 4-14, 4-16, and 4-18 compare for each sample the observed color from polar diagram model results & ping pong ball images, as well as the reflectance spectra measured at the specular condition for each angle of illumination. The reflectance spectra for θ_{inc} = θ_{obs} can be compared across samples to visualize the difference in angular dependency of hue and spectral width. Figures 4-15, 4-17, and 4-19 compare measurements of angular dependency of hue via experimental reflectance spectra for *rough-flat, flat-rough,* and *rough-rough* samples. The *flat-flat* sample is omitted for additional hue travel comparison because the reflectance spectra in Figure 4-13 captures all necessary hue travel information.
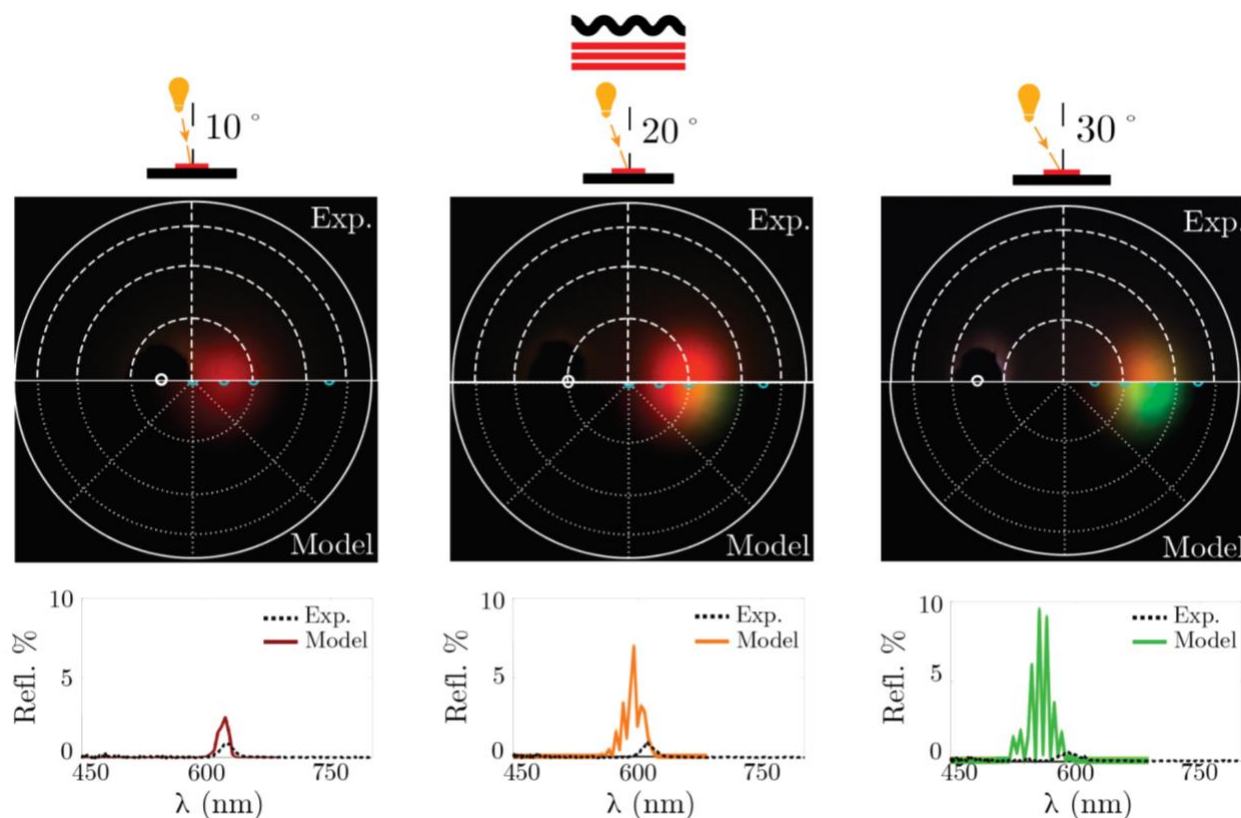
Flat topcoat - flat photonic texture:
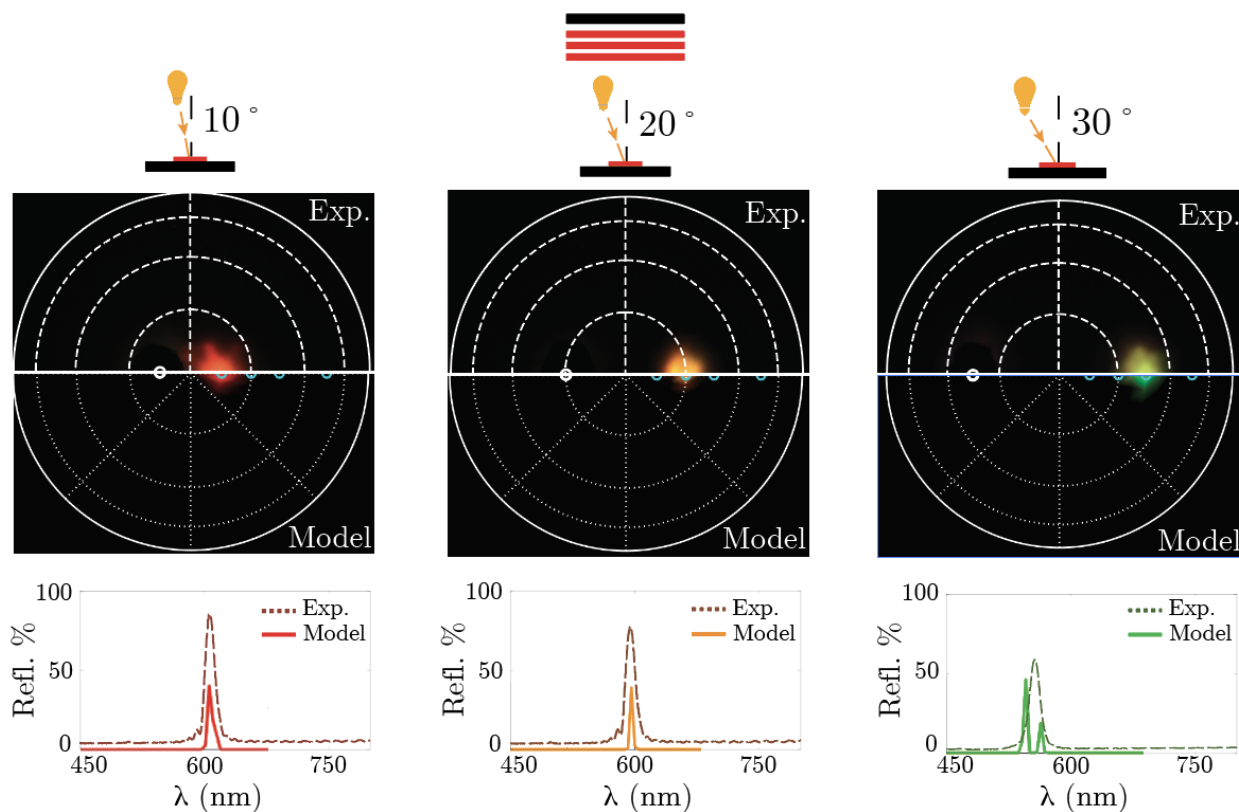
Figure 4-13 – Flat-flat experimental and model comparison: Comparison of experimental and model data for *flat-flat* sample, at three illumination conditions (θ_{inc} = 10°, 20°, and 30°). The upper set of images compares the experimental ping-pong ball images to the polar diagram model outputs. The experimental images are normalized according to scaling factors in Figure 4-11 above. The lower set of images compares the experimental spectra to the model spectra outputs. Spectra are reported at specular conditions, where θ_{inc} = θ_{obs} (e.g. θ_{inc} = θ_{obs} = 10° for the left column).

Figure 4-13 shows good agreement between the observed experimental color and model color, good agreement on center wavelength location, and reasonable agreement on spectral width. Similarly, the green color split into two peaks in $\theta_{inc} = 30°$ spectra can be explained by resolution of the modeling. The unit solid angle Ω of the experimental spectrometry setup was 0.19 square degrees, and Ω of the model was close to 50 square degrees. The wavelength resolution was 5 nm, leading to under-resolved spectrum. Modeling was conducted at low-resolution based on the computation limits and time constraints, but these data can easily be reproduced with smaller Ω/higher wavelength resolution, which is addressed in section 4.5.

The discrepancy in diffuseness is based on the difference between the flat topcoat scattering angle in the model and the experimental beam size. The incident light on the experimental sample was a collimated beam with diameter of ~2mm. The width of the "beam" of incident light on the model sample is determined by the flat topcoat scattering angle (1°), which is equivalent to a collimated beam of diameter $\ll$1mm).

In agreement with the hypothesis and model results, the flat-flat sample has a narrow diffuseness, bright and pure color, and high angular dependency of hue when $\theta_{inc} = \theta_{obs}$. Thus, we get a surface-protected sample that is highly reflective of a narrow wavelength range and can only be observed at a narrow range of angles.

Rough topcoat - flat photonic texture:

Figure 4-14 – Rough-flat experimental and model comparison: Comparison of experimental and model data for *rough-flat* sample, at three illumination conditions (θ_{inc} = 10°, 20°, and 30°). Images compare the experimental ping-pong ball images to the polar diagram model outputs. The DSLR images are normalized according to scaling factors in Figure 4-11 above. Spectra are reported for θ_{inc} = θ_{obs}. Note the spectral y-axis range is from 0-10% reflectivity.
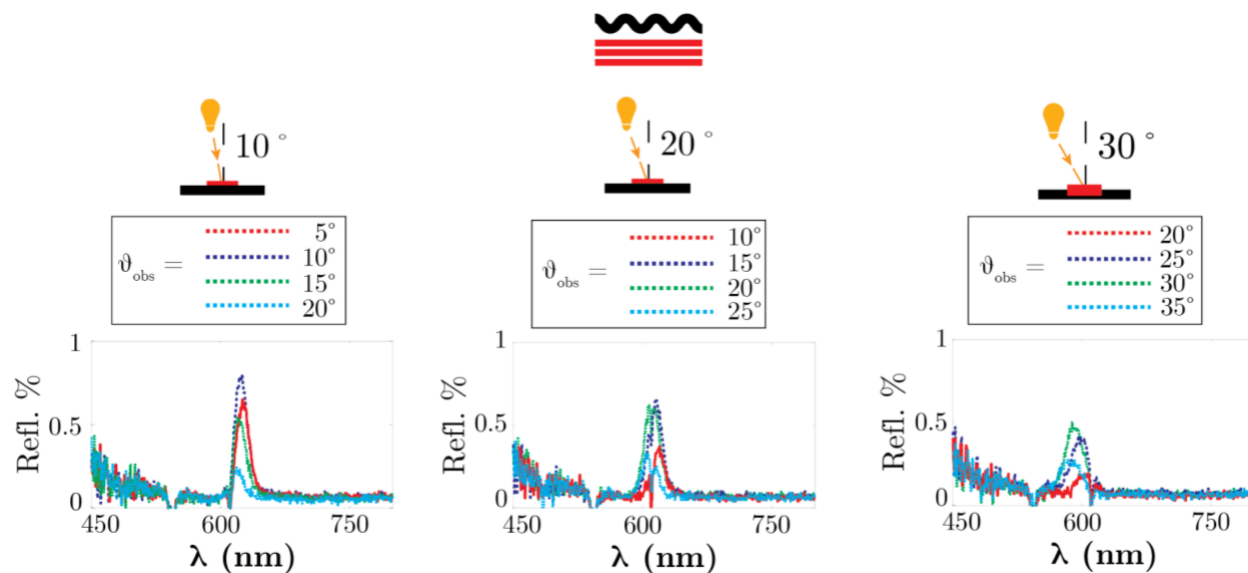
Figure 4-15 - Rough-flat angular dependency of hue: Experimental spectra, demonstrating spectral width as well as angular dependency of hue for the *rough-flat* sample. Spectra were collected at three illumination conditions (θ_{inc} = 10°, 20°, and 30°) and many observation conditions. Reported for each θ_{inc} are four θ_{obs} in increments of 5°. The *rough-flat* sample has low reflectance (close to 1%) and narrow spectral width. Angular dependency of hue as a function of observation angle is low at low θ_{inc} and increases as θ_{inc} increases. Angular dependency of hue as a function of illumination angle is also low.

Figures 4-14 and 4-15 show good agreement on diffuseness. There is better agreement between observed experimental color & model color and better agreement on center wavelength location at lower θ_{inc}. There is agreement in angular dependency of hue as a function of observation angle that decreases as θ_{inc} increases. There is very poor agreement in reflectance of spectra: in the model intensity increases as θ_{inc} increases, and in the experimental data intensity decreases as θ_{inc} increases. Increasing θ_{inc} may accentuate the effects of topcoat surface roughness, i.e. incident light scattering, as light is scattered to sharper angles of incidence within the sample and then scattered to wider ranges as it exits the sample from the rough topcoat.

The sparse spectral peaks for θ_{inc} = 10°, 20° are due to low resolution modeling, as discussed in the *Flat-flat* section above. Future work would look to repeat the modeling and experiments to address these discrepancies.

Also, there is a lower spectral width in the experimental setup. Results from model testing at higher photonic structure period (675 nm) suggest that this can be explained by the exposure step occurring at a slight tilt between 10 - 20°, which could be a combination of the projector's diverging light path and a skewed mounting angle (see Appendix A.3).

In partial agreement with the hypothesis and model results, the rough-flat sample has a broadened diffuseness and broadened spectral width. We get a sample with some color constancy at low θ_{inc} and a widened viewing angle.

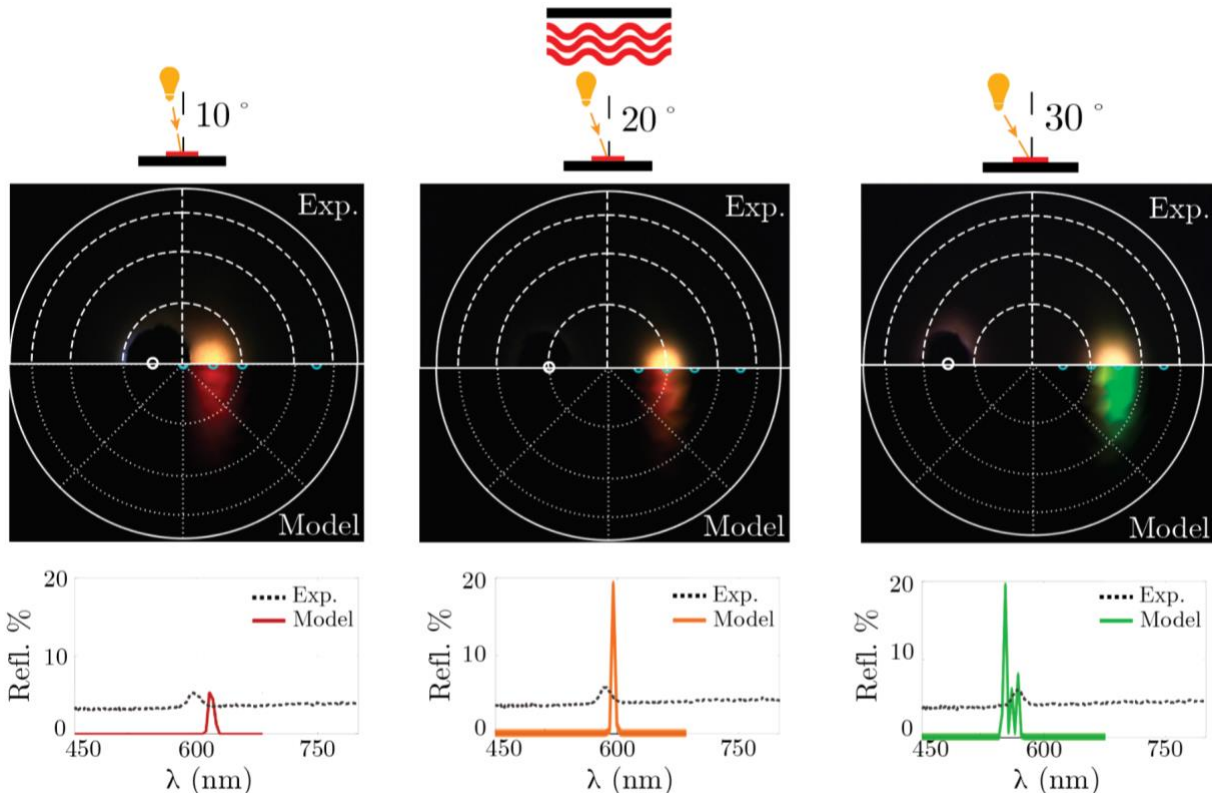*Flat topcoat - rough photonic texture:*

Figure 4-16 – Flat-rough experimental and model comparison: Comparison of experimental and model data for *flat-rough* sample, at three illumination conditions (θ_{inc} = 10°, 20°, and 30°). Images compare the experimental ping-pong ball images to the polar diagram model outputs. DSLR images are normalized according to scaling factors in Figure 4-11 above. Spectra are reported at $\theta_{inc} = \theta_{obs}$. note the spectral y-axis range is from 0-20% reflectivity.
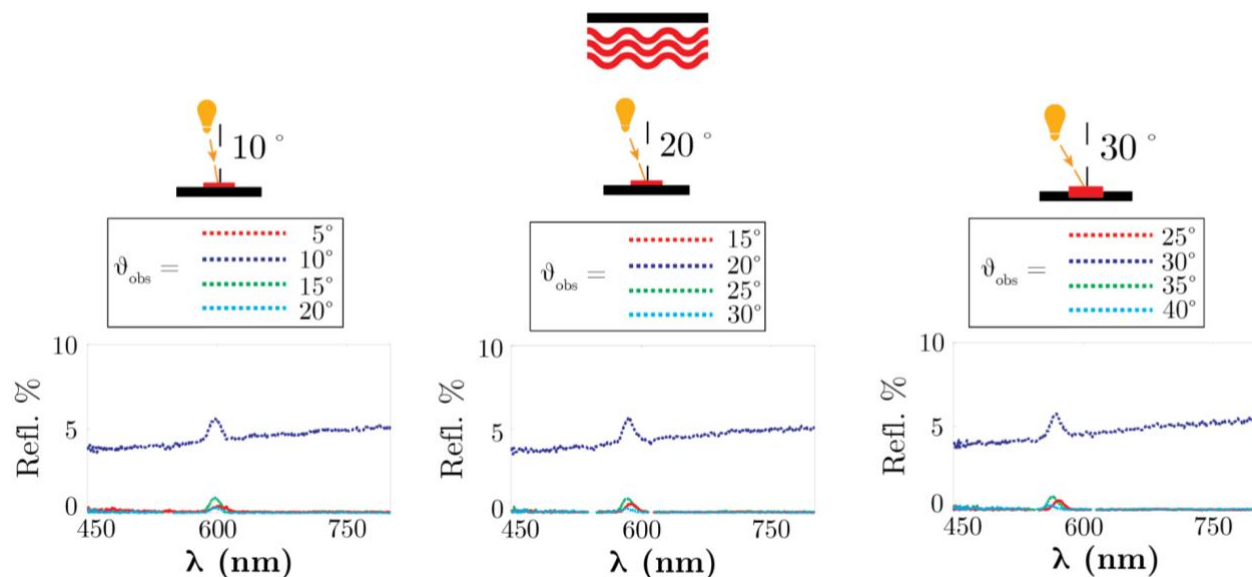
Figure 4-17 – Flat-rough angular dependency of hue: Experimental spectra, demonstrating spectral width and angular dependency of hue for the *flat-rough* sample. Spectra were collected at three illumination conditions (θ_{inc} = 10°, 20°, and 30°) and many θ_{obs}. Reported for each θ_{inc} are four θ_{obs} in increments of 5°. θ_{inc} = 10° has three θ_{obs} due to physical limitations of the experimental setup. The *flat-rough* sample has low reflectance (<5%) especially at off-specular observation angles $\theta_{inc} \neq \theta_{obs}$. Angular dependency of hue as a function of observation angle can be observed as the peak center wavelength shifts slightly for each θ_{inc} condition. Hue as a function of illumination angle and specular condition angles both can be observed as the peak center wavelength shifts, but spectra at θ_{inc} = θ_{obs} are mostly dominated by the broadband spectral information (background ~4% reflectivity across the spectrum).

Figures 4-16 and 4-17 show general poor agreement between model results and experimental results for *flat-rough*, which is mostly connected to the strong specular reflections on the experimental flat topcoat surface. There is close agreement on angular distribution in the x-direction and poor agreement in the y-direction. DSLR images mostly detected the bright specular reflection, so the expected scattered color (with narrow spectral distribution) is washed out in the camera detector. Also, note the consistent 4% background in the experimental spectra, seen in both Figures 4-16 and 4-17 at θ_{inc} = θ_{obs}. Low reflectance peaks in experimental spectra potentially suggest a diverging or poorly aligned spectrometric beam and would be addressed in future work with cleaner measurements.

While most agreement is poor, there is good agreement in spectral position λ_p. The sparse spectral peaks for θ_{inc} = 10°, 20°, 30° are due to model outputs at low resolution, as discussed above in the *Flat-flat* results.

In agreement with the hypothesis and model results, the *rough-flat* sample has a broadened angular distribution, where the viewing angle is anisotropic in x and y based on the anisotropic brushed surface profile. The broadened spectral distribution also agrees with our hypothesis and model results. Thus, we get a sample with some color constancy at low θ_{inc} and a widened viewing angle that greatly suffers from strong background specular highlights.

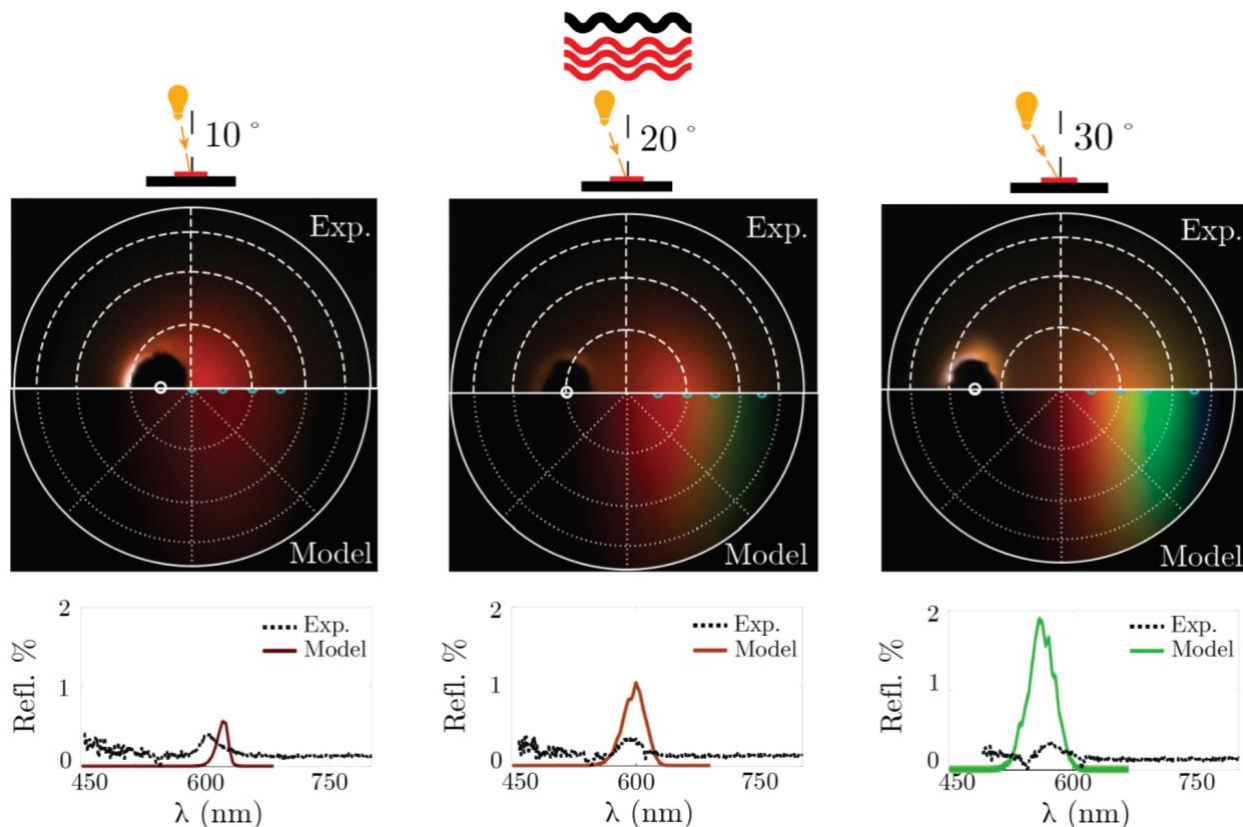*Rough topcoat - rough photonic texture:*

Figure 4-18 – Rough-rough experimental and model comparison: Comparison of experimental and model data for *rough-rough* sample, at three illumination conditions (θ_{inc} = 10°, 20°, and 30°). Images compare the experimental ping-pong ball images to the polar diagram model outputs. DSLR images are normalized according to scaling factors in Figure 4-11 above. Spectra are reported at $\theta_{inc} = \theta_{obs}$. Note the spectral y-axis ranges from 0-2% reflectivity.
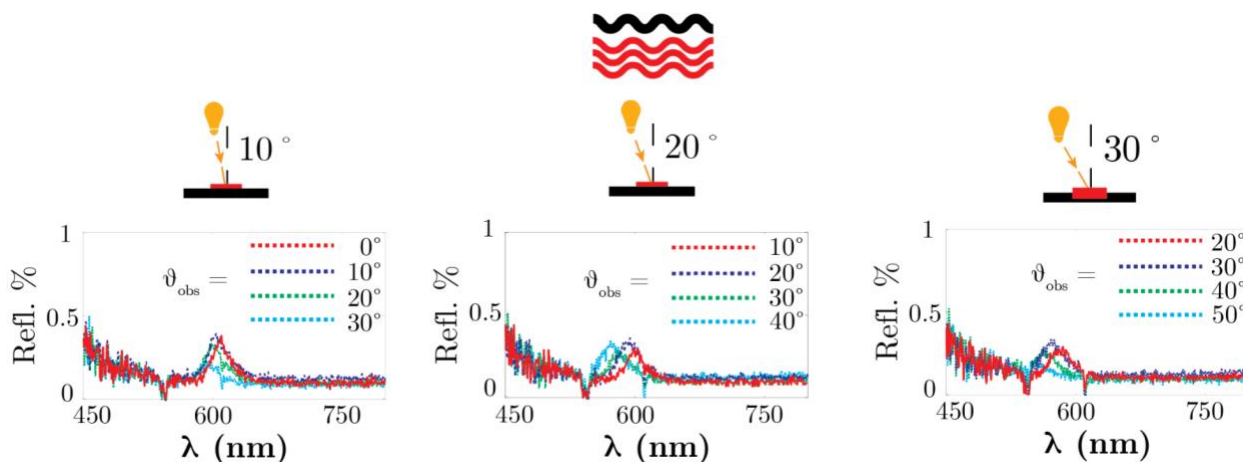
Figure 4-19 – Rough-rough angular dependency of hue: Experimental spectra, demonstrating spectral width and angular dependency of hue for the *rough-rough*

sample. Spectra were collected at three illumination conditions (θ_{inc} = 10°, 20°, and 30°) and many θ_{obs}. Reported for each θ_{inc} are four θ_{obs} in increments of 10°. The *rough-rough* sample has low reflectance (~1%) and wide spectral peaks. Angular dependency of hue as a function of observation angle is low, as λ_p remains mostly constant for each θ_{inc} condition. Angular dependencies of hue as functions of illumination angle and specular angles are also low.

Figures 4-18 and 4-19 show close agreement on angular distribution in both x-direction and y-directions. DSLR images were captured at long exposure and scaled significantly, so some information on the scattering width is lost at the far edges due to the translucence of the ping-pong ball material. There is good agreement between observed experimental color and model color, especially at lower θ_{inc}; the experimental color appears more blended than the model color. This can be explained by the integration resolutions used in the model, where the unit solid angle of the experimental system is two orders of magnitude higher than that of the model outputs presented here, as discussed in the *Flat-flat* section on unit solid angle Ω and in section 4.5 on limitations of high-resolution modeling.

Experimental spectra are hampered by the noise of the spectrometer device, which hovers around 0.25% for wavelengths between 400 - 500 nm. It was not possible for most spectral data of the *rough-rough* sample to detect the difference from noise at standard reference. The standard reference for the three previous samples was taken with a 1 mm aperture diameter. For *rough-rough* spectral measurements, the aperture was opened completely to 5 mm, increasing Ω to 13 square degrees. While intensity information from these measurements is inaccurate and unreliable, spectral width and angular dependency of hue can be estimated more accurately. For clarity, noise has been truncated around 450 nm for some spectra. From these data, we see good agreement on λ_p position and reasonable agreement on spectral width. Spectral widths in the model increase as θ_{obs} increases away from the θ_{inc} = θ_{obs} condition.

In agreement with the hypothesis and model results, the *rough-rough* sample has the widest angular distribution where the viewing angle is anisotropic in x and y based on the anisotropic brushed surface profile. It also has the widest spectral distribution, as predicted from our hypotheses and model results.

All four samples demonstrate some model and experimental agreement, especially in angular distribution. The model was further used to define outer extents of the design space, as well as limitations of this material system.

4.4 Discussion of accessible design space

Table 4-3 shows the scattering parameters used to expand the design space. Scattering parameters were selected based on the empirically measured scattering angles and adjusted for theoretically isotropic brushed surfaces.

Table 4-3 – Modeling with scattering angles to expand the design space

Flat flat	Rough flat
$\alpha = 1.0°$ $\beta x = 0.01°$ $\beta y = 0.01°$	$\alpha = 6°$ $\beta x = 0.01°$ $\beta y = 0.01°$
Flat rough	Rough rough
$\alpha = 1.0°$ $\beta x = 12°$ $\beta y = 12°$	$\alpha = 6°$ $\beta x = 25°$ $\beta y = 25°$

Results of the expanded design space modeling are presented in Figure 4-20. A full metric evaluation is presented in Figure 4-21, which compares all four samples – initial model results, experimental results, and expanded design space results.
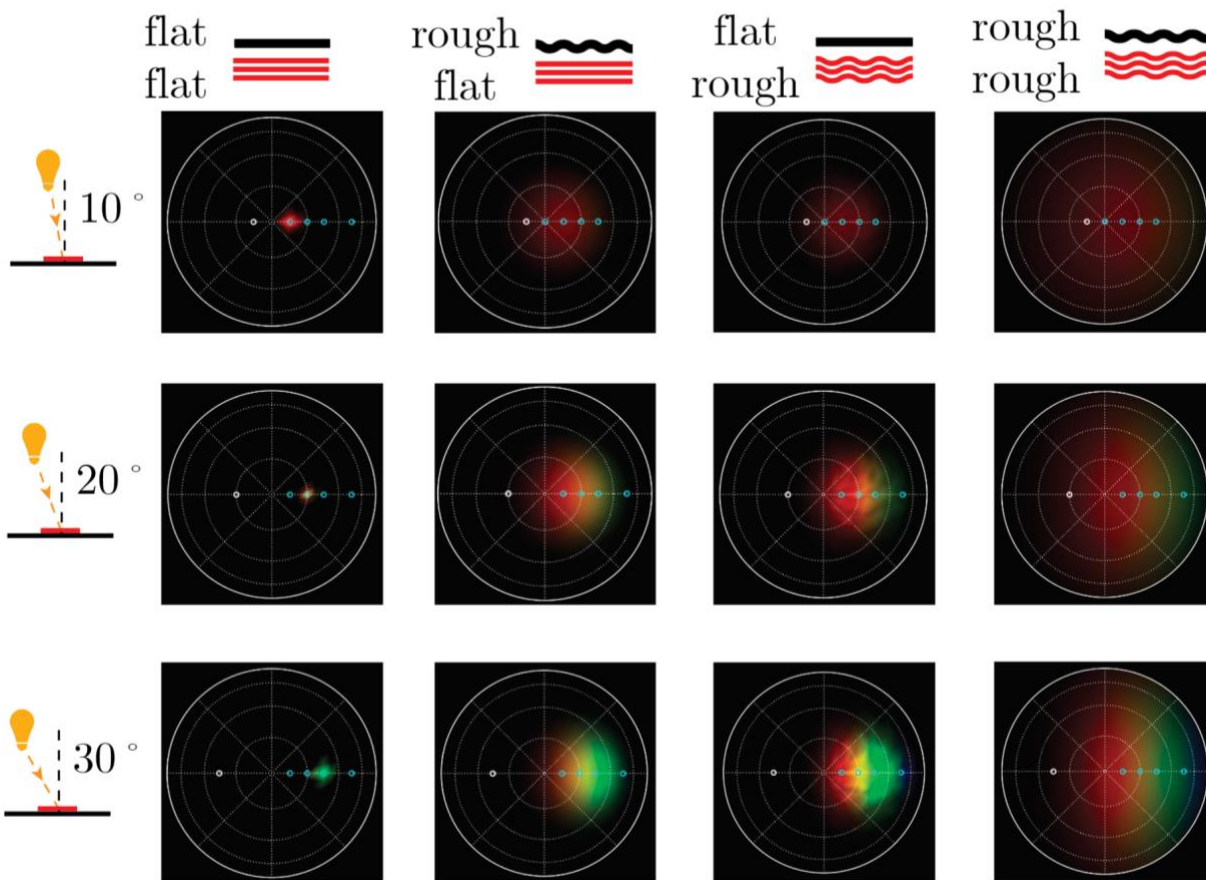
Figure 4-20 – Expanded design space model outputs for four samples: Polar diagram outputs from model, demonstrating an expanded design space. Simulations were performed at three illumination conditions (θ_{inc} = 10°, 20°, and 30°). The incident light direction/position is marked by a small white circle on the left side of each image. The images are uniformly scaled by a "brightness factor" in MatLab for greater visibility. Sample parameters are as follows: *flat-flat* $\alpha = 1.0°$, $\beta_x = \beta_y = 12°$; *rough-flat* $\alpha = 6°$, $\beta_x = \beta_y = 0.01°$; *flat-rough* $\alpha = 1°$, $\beta_x = \beta_y = 12°$; *rough-rough* $\alpha = 6°$, $\beta_x = \beta_y = 25°$.

flat ▬
flat ≡

	Model	Exp.	D.S.
Obs. Hue (Δnm/Δ°)	–	–	–
Ill. Hue (Δnm/Δ°)	–	–	–
Spec. Hue (Δnm/Δ°)	3.50	2.51	3.50
Spectral width (nm)	10.0	14.4	10.0
Diffuseness (% of 2π)	1.12%	2.07%	1.12%

rough 〰
flat ≡

	Model	Exp.	D.S.
Obs. Hue (Δnm/Δ°)	1.50	0.98	1.75
Ill. Hue (Δnm/Δ°)	3.25	0.67	2.25
Spec. Hue (Δnm/Δ°)	3.00	1.74	3.75
Spectral width (nm)	22.1	20.2	35.6
Diffuseness (% of 2π)	8.34%	7.21%	15.8%

flat ▬
rough 〰

	Model	Exp.	D.S.
Obs. Hue (Δnm/Δ°)	0.00	0.48	1.83
Ill. Hue (Δnm/Δ°)	–	1.30	3.00
Spec. Hue (Δnm/Δ°)	3.50	1.46	3.75
Spectral width (nm)	14.0	17.2	11.9
Diffuseness (% of 2π)	6.85%	3.90%	19.3%

rough 〰
rough 〰

	Model	Exp.	D.S.
Obs. Hue (Δnm/Δ°)	1.78	0.77	1.75
Ill. Hue (Δnm/Δ°)	2.00	0.78	3.50
Spec. Hue (Δnm/Δ°)	3.75	1.64	1.50
Spectral width (nm)	33.0	40.8	47.1
Diffuseness (% of 2π)	42.7%	24.7%	76.7%

Figure 4-21 – Full metric evaluation comparing model, experimental, and expanded design space: A comparison of four samples, from model results ("model"), experimental results ("exp.), and expanded design space model results ("D.S."). The metric details are outlined below. Optical properties are angular dependency of hue for changing observation direction ("Obs. Hue"), angular dependency of hue for changing illumination direction ("Ill. Hue"), angular dependency of hue for changing observation and illumination direction ("Spec. Hue"), spectral width, and diffuseness.

Angular dependency of hue as a function of observation direction was measured at fixed angle of incidence θ_{inc} = 20° as the average of the change in spectral position λ_p while changing θ_{obs} between 10° and 30°. Angular dependency of hue as a function of illumination direction was measured at fixed angle of observation θ_{obs} = 20° as the average of the change in λ_p while changing θ_{inc} between 10° and 30°. Angular dependency of hue as a function of observation and illumination directions (at specular constraint θ_{inc} = θ_{obs}) was measured as the average of the change in λ_p while changing θ_{inc} and θ_{obs} between 10° and 30°. Spectral width was measured in Matlab as the average of all spectra at θ_{inc} = 10°, 20°, and 30°, and θ_{obs} = 10°, 20°, 30°, and 50°. Diffuseness was measured using Adobe Illustrator, where the threshold of observable light was determined by eye as the boundary when colored pixels were indistinguishable from black pixels. Reflectance was measured as the maximum reflectivity % of all collected spectra, normalized by the unit solid angle (Ω) of the model, ($\Omega \approx$ 50 sq. degrees) and the experimental setup (0.2 < Ω < 13 sq. degrees).

From the above results, the model is a good predictor for diffuseness and spectral width. It is not accurate on angular dependency of hue. Presumably, this could be

improved by accounting for scattering as a function of wavelength. The model is also highly flexible and could be improved or modified to consider many other photonic structures or functions.

The manufacturing techniques employed for all four samples were straightforward and trouble-free, which suggests that these techniques may be replicable for others and scalable in the future.
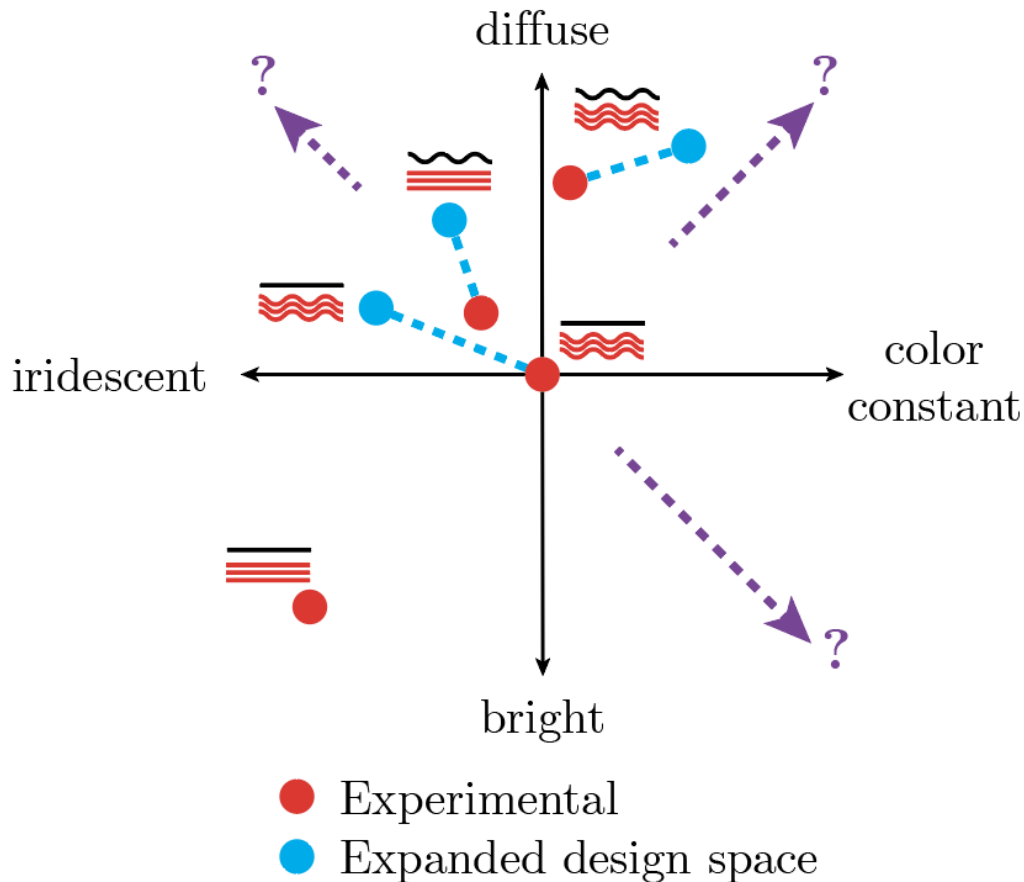
Figure 4-22 – Design space schematic: Representation of the experimentally-achieved design space compared with the expanded design space model results. The purple question marks indicate the far edges of the possible design space, which could be explored as future work.

Figure 4-22 schematically represents the extent of the full achievable design space versus what we were able to achieve, based on the metrics measured in Figure 4-21. Most results live above an imaginary y = x line, i.e. most results are more iridescent and diffuse than they are bright and color constant. Future work could look to expand the design space even further, as well as addressing some core limitations of this approach.

4.5 Limitations and considerations

Computing power is a critical limitation to the modeling technique. While the model calculations can be quite rapidly iterated, for a user with a reasonably-powered computing station the model must be run at low resolution. Modeling was mostly conducted with a wavelength resolution of 5 nm, an icosphere mesh value of 4, and integration variable resolution $d\theta_{obs} = 5°$ and $d\varphi_{obs} = 10°$ on a MacBook Pro 2020 with 16 Gb of RAM, to balance speed and accuracy of the spectral outputs. Each individual sample model run took between 30 and 40 minutes at that resolution (half a day run time for 21 total samples). To match the wavelength resolution of the spectrometer, modeling should be conducted at ~0.5 nm. To match the unit solid angle Ω of the experimental system with a 0.6mm aperture and 140mm detector arm length, modeling should be conducted with $d\theta_{obs} = 0.5°$ and $d\varphi_{obs} = 0.5°$: experimental Ω of 0.19 square degrees vs. model Ω of 0.25 square degrees. Modeling at this unit solid angle, i.e. high resolution, would take roughly two and a half months to process all 21 samples while running continuously on a standard desktop computer. Due to the computational limits of the available desktop computers, MIT's SuperCloud computing cluster was explored to speed up the modeling process [38] but was unable to be implemented by the completion date of the thesis. The model code could also be optimized in discrete calculation of the quadruple BRDF integral to improve efficiency.

As the model suggests, the experimental *flat-rough* and *rough-flat* samples are similar in appearance. The *flat-rough* sample has specular white highlights that the *rough-flat* sample lacks. The *rough-flat* sample has narrower spectral widths at the same observation angles, and the difference in spectral width between these two samples gets more apparent as the angle of incidence increases. The broader spectral widths are associated with visual appearances of muted colors. However, *flat-rough* samples have general poor agreement with the model, mostly stemming from strong specular reflections on the flat topcoat surface. Imaging with the DSLR camera detected these specular reflections, so the expected pure colors with narrow spectral widths are washed out in the camera detector. For this reason, I suggest against using a flat topcoat with the diffuse photonic film, as it diminishes the benefits of the diffuse photonic structure.

With the *flat-flat* sample, the lack of specular highlights was surprising. Bright specular highlights were seen more strongly in the *flat-rough* sample, especially in the ping-pong ball images. It appears that the flat topcoat does little to enhance aesthetic appearance but can serve as a surface protective layer if not operating at specular conditions.

With the *rough-rough* sample, the high diffuseness can be an asset if dealing with an application where unit-solid angle increases. With the other three samples, increasing unit solid angle does not change intensity collection.

Additional metrics of iridescent materials – such as brightness (average of reflectance over wavelength range), angular dependency of brightness, and angular dependency of spectral width – could be added to improve the accuracy of mapping the extents of the design space [20].

Color constancy and brightness seem to be tradeoffs. This is relevant for sensing platforms a la GelSight [39] where a camera with fixed exposure time is being used and detection would mostly be improved by lowering sensing thresholds or increasing illumination intensity.

The execution of this research was not always direct and focused. I learned how to theorize, model, experiment, characterize, and write, all while conducting the research. So, rather than following a clear storyline as laid out in many theses and research articles, my process looked like experiment, characterize, theorize, model, experiment, characterize, theorize, model, experiment, characterize, write, write, write. The non-linearity of scientific research is a beautiful and joyful experience at times, and at other times it can be bewildering. I encourage anyone reading this work that, wherever you are in your process, you *can* keep going.

Finally, the agreement between the modeling and experimental results demonstrates that controlling texture of the photonic film and roughness of its topcoat allows for tailoring the visual appearance of structurally colored materials. Our approach is promising, in terms of opening a rich design space of different appearances, including strong iridescence, color constancy with collimated light sources at small angles of incidence, pure or muted colors, and specular or highly diffuse reflections.

Chapter 5: Conclusions and Suggestions for Future Work

5.1 Summary

A wide design space of appearances and optical properties has been achieved experimentally in structurally colored, color dynamic films. Rough topcoats were applied to holographically manufactured photonic films to modify the incoming and outgoing light fields. Photonic films were manufactured on flat mirror surfaces and diffuse reflective surfaces to modify the texture of the photonic structure, which affects the angular and spectral distributions of the reflected light.

A robust and versatile model was constructed based on Fourier optics to simulate the optical appearance and properties of textured photonic materials with rough topcoats. While the computational implementation of the model suffers from large run times, the model can be tailored to fit many photonic material systems and could be improved by optimizing the quadruple integral implementation.

Procedures were established for fabrication and characterization of photonic films with rough topcoats, allowing for ease in manufacturing and analysis of the materials' optical characteristics. Pure colors were achieved in the *flat topcoat-flat photonic texture*, *flat topcoat-rough photonic texture*, and *rough topcoat-flat photonic texture* samples; muted colors were achieved in the *rough topcoat-rough photonic texture* sample. Specular reflection was achieved in the *flat topcoat-flat photonic* sample; highly diffuse reflections were achieved in the *rough topcoat-flat photonic texture* and *rough topcoat-rough photonic texture* samples. Strong iridescence was achieved in the *flat topcoat-flat photonic* sample; angular color constancy was achieved in the *rough topcoat-flat photonic texture* and *rough topcoat-rough photonic texture* samples, with collimated light sources at small θ_{inc}, i.e. $\leq 10°$.

Spatially controlled optical manufacturing of photonic structures is promising for applications in on-chip optical devices, sensing & imaging (with pixel specific focusing, scattering, or filtering), or microscopy/optically-based characterization techniques, where a small amount of real estate is needed for optical devices. The simple manufacturing process of this material system enables customer specific optical devices. The material system could be supplied to a customer as a blank slate and then optically patterned as needed, specific to the customer's use case. If needed, scattering topcoats could be cast by the customer using a variety of engineered surface profiles, also specific to the customer's use case.

Commercial applications where color constancy and/or isotropy are necessary could benefit from this approach, as in color-dynamic sensing, where the color change must be coupled to a single physical parameter, e.g. strain. Thus, the results demonstrated here could be applied to devices such as bandages, shoes, or robotic grippers, to improve their ability to act as sensors of pressure, force, or shape.

5.2 Suggestions for future work

This work opens various opportunities for further exploration. Surprisingly, the *rough-flat* sample looked both beautiful aesthetically and showed significant diffuseness and color constancy for collimated light sources at small θ_{inc}. The *rough-rough* sample, while having low brightness, could be optimized by tweaking the scattering angle parameters experimentally and in the model. It is suggested to explore the visual appearance design space of the *rough-flat* and *rough-rough* samples further, especially by comparing DSLR images with collimated and highly diffuse illumination sources.

Deeper understanding of wavelength-dependent scattering as a function of surface roughness – via the generalized Harvey Shack (GHS) scatter theory – can make this work relevant across broader wavelength scales. GHS Python scripts are available from Dr. Villads Egede Johansen [40]. The reference link is connected to Dr. Johansen's GitHub page. This Python script can easily be integrated into MatLab, which has previously been demonstrated by Kevin Nattinger at Ohio State [41], who wrote their thesis on converting GHS into Matlab.

Transmissive optical devices could be explored by flipping the materials platform around, where incident light passes through the photopolymer first and exits the scattering layer last.

Our materials platform can easily be expanded on – with shape-decoupled holographic chemistry and/or with advanced manufacturing or lithographic techniques to produce complex surface profiles – for greater control over optical phenomena across the nano- and micro- scales. Use of engineered reflective surfaces, multiple beam optical exposure, or casting of engineered scattering surfaces can add complexity to the materials platform, potentially expanding the design space further.

In conclusion, these future opportunities will further the extent of appearances and optical properties realizable in structurally colored, color dynamic materials, by improving the accuracy of the models used to predict those properties and by expanding the nano-, micro-, and macro- scale morphologies of those materials.

References

1. Polyanskiy, M. N. Refractiveindex.info database of optical constants. Sci. Data 11, 94 (2024).
2. MIT Technology Review. The chemistry behind how you make a record-breaking giant soap bubble. Available at: https://www.technologyreview.com/2019/08/24/102697/the-chemistry-behind-how-you-make-a-record-breaking-giant-soap-bubble (2024).
3. Adobe Stock. Oil slick image. Available at: https://stock.adobe.com/search/images?k=oil+slick+background (2024).
4. Mrázek, J., Tlustý, T., Lázaro, J., & Vojtěch, M. Nanocrystalline Zn2TiO4 films for distributed Bragg's reflectors operating in near infrared region. Optical Materials 112, (2021).
5. McDougal, A., Miller, B., Singh, M. & Kolle, M. Biological growth and synthetic fabrication of structurally colored materials. J. Opt. 21, 073001 (2019).
6. CYPRIS Materials. Available at: https://www.cyprismaterials.com (2024).
7. Sandt, J. D. *et al.* Stretchable optomechanical fiber sensors for pressure determination in compressive medical textiles. Adv. Healthcare Mater. 7, 1800293 (2018).
8. Hong, W., Yuan, Z., & Xudong, C. Structural color materials for optical anticounterfeiting. Nano-Micro Small (2020).
9. Miller, B. H. Scalable optical manufacture of dynamic structural colour in stretchable materials. Nature Mater. 10 (2022).
10. Lippmann, G. La photographie des couleurs. Comptes Rendus Hebdomadaires des Séances de l'Académie des Sciences 112, 274-275 (1891).
11. Miller, B. Design, fabrication, and application of bioinspired soft photonic materials. (2023).
12. Hecht, E. Optics. 3rd edn (Addison-Wesley Publishing Company, 1998).
13. Dominé, D., Haug, F.-J., Battaglia, C. & Ballif, C. Modeling of light scattering from micro- and nanotextured surfaces. J. Appl. Phys. 107, 044504 (2010).
14. Born, M. & Wolf, E. Principles of Optics: Electromagnetic Theory of Propagation, Interference and Diffraction of Light (Cambridge University Press, Cambridge; New York, 1999).
15. Beckmann, P. & Spizzichino, A. The Scattering of Electromagnetic Waves from Rough Surfaces (Artech House, Norwood, 1987).
16. THz Communications: Paving the Way Towards Wireless Tbps. Vol. 234 (Springer International Publishing, Cham, 2022).
17. Lundstrom, M. Scattering and Transmission, ECE-656 (Purdue University, 2011).
18. Maiwald, L. *et al.* Ewald sphere construction for structural colors. Opt. Express 26, 11352 (2018).
19. Nicodemus, F. E., Richmond, J. C., Hsia, J. J., Ginsberg, I. W. & Limperis, T. Geometrical considerations and nomenclature for reflectance. NBS MONO 160 (1977).
20. Gruson, H. *et al.* Quantitative characterization of iridescent colours in biological studies: a novel method using optical theory. Interface Focus 9, 20180049 (2019).

21. Ellingson, S. W. Electromagnetics, Vol. 1 (VT Publishing, Blacksburg, Virginia, 2018).
22. Covestro. Optical properties of Technology. Available at: https://solutions.covestro.com/en/highlights/articles/theme/product-technology/optical-properties (2024).
23. Wikipedia. Normal distribution. Available at: https://en.wikipedia.org/wiki/Normal_distribution (2024).
24. Tavernier, S. Experimental Techniques in Nuclear and Particle Physics (2010).
25. Johansen, V. E. Preparing the generalized Harvey–Shack rough surface scattering method for use with the discrete ordinates method. J. Opt. Soc. Am. A 32, 186 (2015).
26. Krywonos, A., Harvey, J. E. & Choi, N. Linear systems formulation of scattering theory for rough surfaces with arbitrary incident and scattering angles. J. Opt. Soc. Am. A 28, 1121 (2011).
27. Beckmann, P. Scattering of Light by Rough Surfaces, Progress in Optics pp. 53-69, (Elsevier, Volume 6, 1967).
28. Ward, W. O. C. Icosphere script. Available at: https://www.mathworks.com/matlabcentral/fileexchange/50105-icosphere (2015).
29. Yamahata, C. Human vision and the CIE chromaticity diagram (2024).
30. Wikipedia. CIE 1931 color space. Available at: https://en.wikipedia.org/wiki/CIE_1931_color_space (2024).
31. Schanda, J. Colorimetry: Understanding the CIE System (2007).
32. MATLAB. Convert CIE 1931 XYZ to RGB. Available at: https://www.mathworks.com/help/images/ref/xyz2rgb.html#d126e339779 (2024).
33. MATLAB. rgb2xyz help page. Available at: https://www.mathworks.com/help/images/ref/rgb2xyz.html (2024).
34. Judd, D. B. The computation of colorimetric purity. J. Opt. Soc. Am. 13, 133-154 (1926).
35. Xia, L. et al. Light diffuseness metric Part 1: Theory. Lighting Research & Technology 49, 411-427 (2017).
36. Covestro. Bayfol HX sales sheet. Available at: https://solutions.covestro.com/en/products/bayfol/bayfol-hx200_86194384-20033146?SelectedCountry=US (2024).
37. Kirkman, T. The Softbox: An Introduction. Available at: https://www.bhphotovideo.com/explora/photography/tips-and-solutions/the-softbox-an-introduction#:~:text=Softboxes%2C%20on%20the%20other%20hand,wider%20wash%20of%20the%20umbrella (2024).
38. Reuther, A. et al. Interactive supercomputing on 40,000 cores for machine learning and data analysis. IEEE High Performance Extreme Computing Conference (2018).
39. GelSight. Company page. Available at: https://www.gelsight.com/ (2024).
40. Egede, V. Python implementation of generalized Harvey-Shack rough surface scattering method using discrete ordinates. Available at: https://github.com/villadsegede/cosineGHS (2017).

41. Nattinger, K. Experimental validation of the generalized Harvey-Shack surface scatter theory. Available at: https://etd.ohiolink.edu/acprod/odb_etd/etd/r/1501/10?clear=10&p10_accession_num=wright15362469220747447 (2018).
42. Park, H. *et al.* Mechanochromic palettes of cholesteric liquid crystal elastomers for visual signaling. Adv. Optical Mater. 2400266 (2024).
43. Kiebala, D. J. *et al.* Sub-micrometer mechanochromic inclusions enable strain sensing in polymers. Adv. Funct. Mater. 33, 2304938 (2023).
44. Clough, J. M., Kilchoer, C., Wilts, B. D. & Weder, C. Hierarchically structured deformation-sensing mechanochromic pigments. Adv. Sci. 10, 2206416 (2023).
45. Ma, J. *et al.* Mechanochromic, shape-programmable and self-healable cholesteric liquid crystal elastomers enabled by dynamic covalent boronic ester bonds. Angew. Chem. Int. Ed. 61, e202116219 (2022).

Work Credits:

Mathias Kolle for writing the core Matlab scripts used in this thesis, including calculation of the angularly and spectrally resolved reflectivity based on incoherent superposition and Fourier optics, normalizing images, implementation of routines to minimize computation time, converting spectra to RGB, and plotting polar diagrams.

Ben Miller for lending me his Matlab Ewald's sphere model as reference.

OpenAI's ChatGPT for editing with clarity and concision in "mind."

Appendix

A.1 Color-dynamic sensing

Nanostructures that reflect and filter light can be harnessed in dynamic systems that use color as a sensing mechanism. The structure can be actuated chemically (e.g. reaction, pH, or moisture), electrically or thermodynamically (e.g. liquid crystalline electrochromic windows or "mood rings"), and/or mechanically (e.g. structural color in elastomers).

Specifically, mechanochromic devices have been demonstrated in several material systems, where a material is mechanically actuated – deformed, stretched, compressed, or pressed – in a way that produces a colorful change which indicates the actuation [42, 43, 44, 45]. Miller et al. [10] demonstrated application of structurally colored films as color-dynamic force sensors in bandages, where the color change is an indicator of pressure within the bandage. We demonstrated, prior to this thesis, the application of color-dynamic films on modified research bandages, medical compression devices, and athletic shoes.
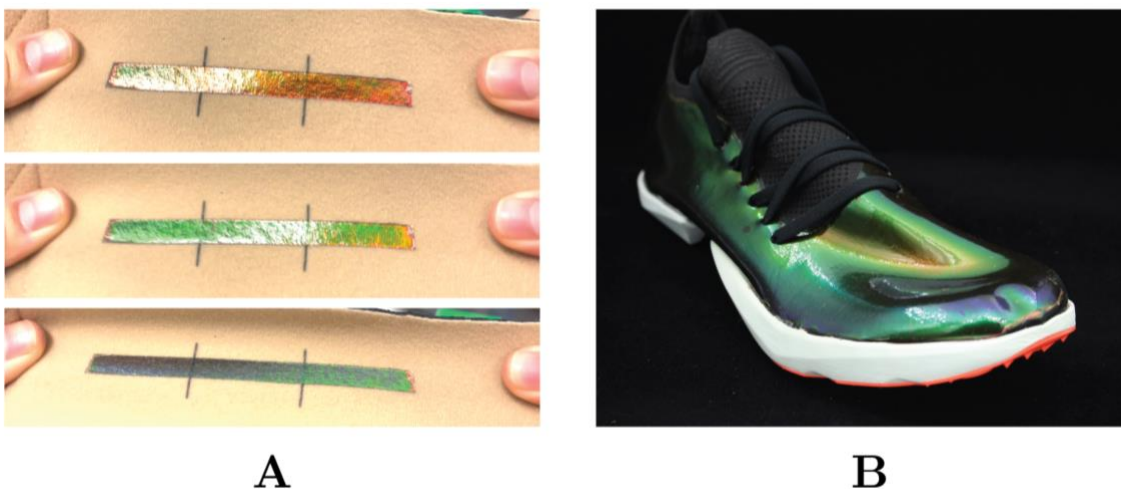

A　　　　　　　　　**B**

Figure A-1 – Applications of color-dynamic materials: (A) Color-dynamic materials applied to Juxtalite bandages, a standard medical compression device used for venous ulcers and other cardiovascular diseases of the extremity. Images from top to bottom show the material being stretched laterally. **(B)** Color-dynamic materials applied to track shoes.

A.2 Discussion on empirical measurements for materials selection

It should be noted that several assumptions and exclusions were made during the empirical characterization process.

Images for transmission and reflection scattering were taken at an angle (~15°). The images were not deskewed for angular correction, because it was assumed that the angular adjustment of the images was small. Future improvements on these measurements should conduct these calculations using images that have been deskewed.

Images were also taken using a beam with a non-zero spot size. The measurements listed in A.6 do account for the scattering angle originating from a non-zero beam spot, but the images were not explicitly deconvolved with a reference/control/mirror spot size. Lastly, scattering is assumed to be independent of wavelength in the model, so it is expected that experimental and model data may diverge as a result. Integration of the generalized Harvey-Shack (GHS) scatter theory, especially for rough surfaces [23], could improve the accuracy of these scatter angle measurements.
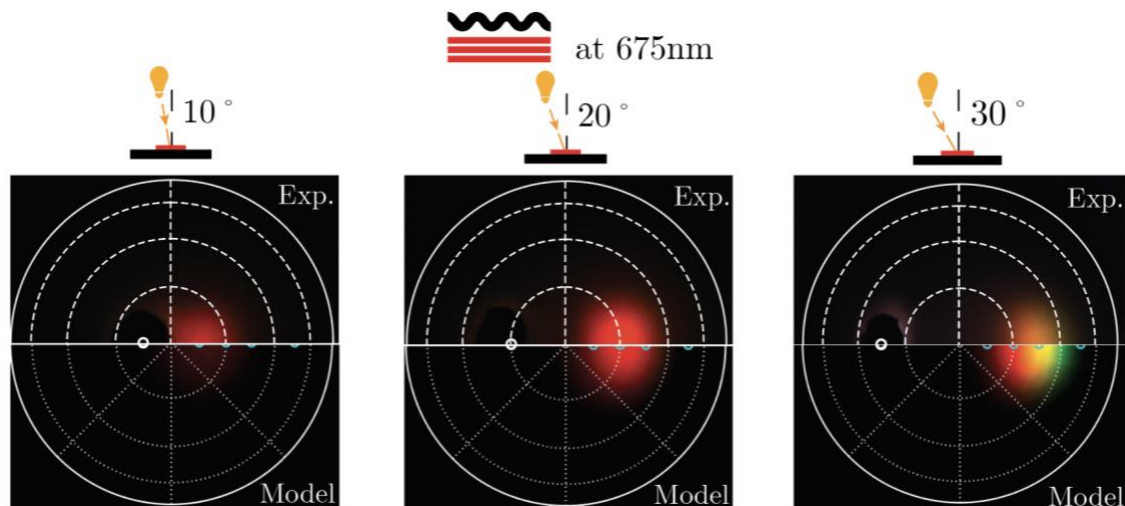
A.3 Model testing at 675 nm

Figure A-2 – Model testing at 675 nm: Comparison of experimental and model data for rough-flat sample with photopolymer/photonic structure made at 675 nm instead of 633 nm. at three illumination conditions (θ_{inc} = 10°, 20°, and 30°). Images compare the experimental ping-pong ball set up images to the polar diagram model outputs. The DSLR images are normalized according to scaling factors in Chapter 4 Figure 4-11.

A.4 Potential sources of error

1. As previously suggested in Appendix A.2, images were not deskewed for angular correction nor deconvolved from the control beam spot. This could contribute to small errors in empirical scattering angle measurements.
2. The function R (*Equation 3.2)* could be defined more precisely, e.g. a Gaussian distribution that is a function of arc length as opposed to projecting a Gaussian in the xy-plane onto a sphere in xyz.
3. The model does not account for white specular highlights.
4. All samples made with 3M Magic™ tape have striations down the center. Photopolymer samples of 1" x 1" were prepared and the Magic™ tape used had a width of ½ ". This could easily be avoided in the future by using 1" wide Magic™ tape.
5. Experimental sample surfaces became warped during curing due to the constriction of the black backing layer. In spectrometric measurements, some samples may have been characterized while positioned at unknown angles.
6. Alignment of the spectrometer was conducted by eye. All collimation was done by eye. One person did all alignments (me) so if there were misalignments, they were at least consistent.
7. During spectrometric measurement, the reference was taken from a mirror placed in a fixture, the mirror was removed, and a sample was placed into the fixture. This process could result in the sample being aligned differently, or even worse could misalign the entire system while removing the mirror/adding sample.
8. The spectral width measurements in Figure 4-17 for the flat-rough samples likely have some error, as the specular highlight is picked up and increases the FWHM measurement. The FWHM was measured from the base of the peak, rather than adjusting the baseline to the 4% specular background.
9. The ping-pong ball images were potentially collected while using a converging beam (again due to collimation error). This would result in additional divergence from model and experimental results.
10. No precise angular markings were used for the qualitative picture setup (Figure 4-3). The camera set up could be more precise to get a more accurate angular comparison.

A.5 Spectrometer alignment components

Rails and pin-hole aperture were used to align the goniometric components of the spectrometer first to the table, and then to each other. Alignment of this device is crucial for accurate measurements. Misalignment in any of the six degrees of freedom can result in high error.
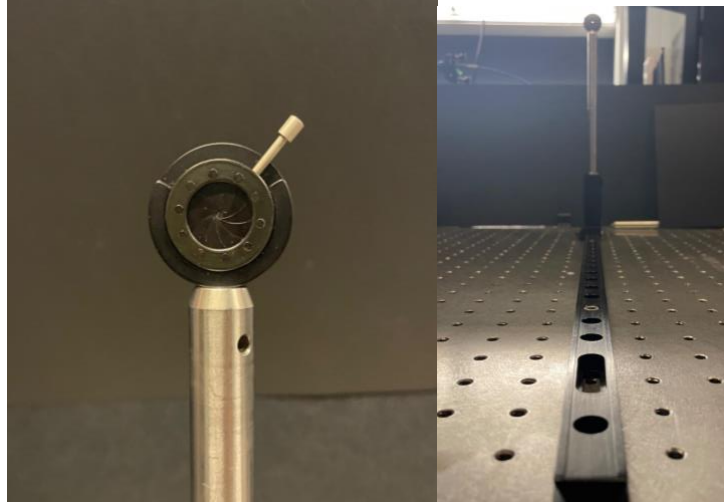
Figure A-3 – Spectrometer rail alignment system: (Left) Iris diaphragm aperture mounted on a post. The aperture is slid to near and far distances to align the source to the table. (Right) The rail mounted to the optics table, with a post and iris aperture on top.

A.6 Materials and equipment

- Solaris from SmoothOn
- Bayfol HX from Covestro
- Mirror: 1" x 1" square UV-enhanced aluminum mirror (ThorLabs)
- Blue vinyl: vinyl sleeve for 4-Piece Finish Selector Pack 304 Multipurpose Stainless Steel (McMaster-Carr)
- Frosted acrylic: Clear frosted P95 acrylic sheet Lucite plexiglass (Amazon)
- Magic™ tape: 3M 810 Scotch® Magic™ tape
- Brushed stainless: Stainless steel 304 with a no. 4 brush finish (McMaster-Carr).
- 18-8 stainless: 18-8 stainless steel shim stock (McMaster-Carr)
- 304 stainless: Multipurpose 304 Stainless Steel Sheet (McMaster-Carr)
- Ocean Optics halogen HL2000 lamp
- Canon EOS Rebel T3i DSLR camera with EFS 18-55mm lens
- Godox SL60W lamp and diffuser
- Lenses from ThorLabs
- ThorLabs SLS201L (spectrometer source)
- Maya 2000 Pro from Ocean (spectrometer)
- Software:
    - MatLab
    - Ocean Software (spectrometer)